



UNIVERSITÀ DI PISA

Dipartimento di Fisica *E. Fermi*

Tesi di Laurea Magistrale in Fisica

Models for axion like particles ALP and sensitivity studies
at Belle II experiment

Relatore:
Francesco Forti

Candidata:
Laura Salutari

Relatore:
Paolo Panci

ANNO ACCADEMICO 2021/2022

Contents

| | |
|--|-----------|
| Introduction | 1 |
| 1 Theoretical overview | 5 |
| 1.1 SM description | 5 |
| 1.1.1 Standard Model as Gauge theory | 6 |
| 1.1.2 Electroweak sector | 7 |
| 1.1.3 Yukawa interaction and mass term | 9 |
| 1.1.4 CP violation in the electroweak interactions | 10 |
| 1.1.5 Open problems | 12 |
| 1.2 CP parity problem in the strong interactions | 13 |
| 1.2.1 Strong interactions | 13 |
| 1.2.2 CP violating term | 14 |
| 1.2.3 Peccei-Quinn mechanism | 15 |
| 1.2.4 Search for axions | 16 |
| 1.3 Introduction to Dark Matter | 17 |
| 1.3.1 Dark matter formation and candidates | 18 |
| 2 ALP model and experimental search | 23 |
| 2.1 Effective ALP model | 23 |
| 2.2 Search and constraints for ALPs | 24 |
| 2.2.1 Laboratory experiments | 25 |
| 2.2.2 Astrophysics and cosmology | 26 |
| 3 QCD axion in the MeV range | 31 |
| 3.1 Phenomenological aspects | 32 |
| 3.1.1 Axion-Electron coupling | 34 |
| 3.1.2 Channels to explore | 37 |
| 4 Axion Like Particle as Dark matter | 39 |
| 4.1 Model description | 39 |
| 4.1.1 Production mechanism | 41 |
| 4.2 Channels to explore | 43 |
| 5 Belle II | 45 |
| 5.1 B-factories | 45 |
| 5.2 Belle II | 47 |
| 5.2.1 Accelerator | 48 |
| 5.2.2 Detector | 49 |

| | | |
|----------|--|-----------|
| 5.2.3 | Software | 54 |
| 6 | Simulation for QCD axion model | 55 |
| 6.1 | Signal | 57 |
| 6.1.1 | Generation | 57 |
| 6.1.2 | Simulation | 58 |
| 6.1.3 | Reconstruction | 58 |
| 6.2 | Background | 59 |
| 6.3 | Event preselections | 60 |
| 6.4 | Region for sensitivity optimization | 62 |
| 6.4.1 | Mass peak | 63 |
| 6.4.2 | Resolution | 67 |
| 6.5 | Radial vertex distribution | 69 |
| 6.6 | Sensitivity estimation | 75 |
| 6.7 | Recast on coupling parameters | 76 |
| 6.7.1 | Dark photon search and recast | 79 |
| 7 | Study on $\tau \rightarrow l \alpha$ | 83 |
| 7.1 | Belle II study | 83 |
| 7.2 | Recast of the limit | 85 |
| | Conclusions | 88 |

Introduction

The thesis work focuses on the theoretical aspects of two types of axion-like particles model with flavor non-universal couplings to Standard Model fermions and their specific phenomenological signatures at the Belle II experiment.

The Standard Model (SM), developed in the half of the '900 century, is able to describe the fundamental forces regulating the interactions between particles and to foresee a great deal of physical processes. Nonetheless, there are many observations that do not find explanation in the standard model picture, of which two are addressed and discussed in this thesis.

One is the “strong CP problem”. The strong interactions are described by the quantum chromodynamics (QCD). It is possible to add in the QCD lagrangian a field term which breaks the invariance of the strong interactions under CP-parity. The violating term is proportional to an angular parameter θ which can take any value in the $[0, 2\pi]$ interval: the bigger the value, the more CP is violated. In this theory CP-violating quantities are allowed, such as the neutron electric dipole moment. From the measurement of this quantity it is possible to infer the value of θ , and the latest measurements give $\theta < 10^{-10}$. At the moment, the Standard Model does not provide an explanation for the small value of theta, hence why the CP violation in QCD should be so “soft”.

The second problem here highlighted is the explanation of the dark matter nature. It is a new type of matter, dark because it emits and absorbs light too little to be seen through electromagnetic interaction. It is known to exist because of experimental evidence concerning astrophysical observations, and it makes up 24% of matter in the Universe. Thanks to cosmology it is possible to estimate with precision the present dark matter abundance, which has been measured by the Planck collaboration.

The search for the particle nature of dark matter started in the '80. The main characteristics of a dark matter particle candidate are: absence of strong and electromagnetic interactions, long life time and a production mechanism for which the particle is non-relativistic in the early Universe. With these requests it is possible to explain how dark matter evaded for so long a direct search and the role it played in the structure formation. Proposal of particles as DM candidates continued in time, arriving at the formulation of new particles as candidates.

Both the problems briefly discussed can not be explained with the fields composing the SM picture, so they require beyond standard model (BSM) theories. Interestingly, a new class of particles could represent a solution for both the open questions.

This class goes by the name of axion-like particles (ALPs). In general they are pseudoscalar particles associated with the Nambu Goldstone boson arising from a new global symmetry $U(1)$ spontaneously broken at an energy scale Λ . The first and most famous type of ALP is the axion derived by the theory of Peccei and Quinn, with

the help of Weinberg and Wilczek. This new particle was proposed as a dynamical solution of the strong CP problem, and it is indicated as QCD axion.

The generalization of axion to ALP can find reason for a lot of different problems still unresolved. In this thesis, there are two realization of a general ALP model with non-universal couplings to the SM fermions. One realization is relative to the description of a QCD axion with mass in the MeV/c^2 range, which implies, for the QCD axion case, new physics at energies $\Lambda \sim O(\text{GeV})$. This model, thanks to the non-universal couplings to fermions, can describe a *pion-phobic* axion, thus evading a number of stringent limits on the QCD axion in such a mass range. This type of axion has relatively strong couplings with the SM fields, and in particular it mainly decays into electron and positron with a short lifetime.

A second realization is unrelated with the QCD problem, and keeps the parameters of mass and Λ value not correlated. This generic ALP can be used as a dark matter candidate by setting a small mass value for the particle, a long lifetime and suppressed coupling to SM sector. In this case, the non-universal couplings allow the ALP to have flavor-violating couplings at tree level. This feature is used in the particle production mechanism, explained via the *freeze-in* of lepton-flavor violating decays of SM leptons. This explanation can match the abundance of the ALP with the abundance of dark matter measured by the Planck collaboration.

The introduction in the SM of new fields imply a great deal of phenomenological signatures which could prove or disprove the theory proposed. The new physics can be searched for by different means, spacing from terrestrial searches (colliders, target experiments, ecc) to astrophysical observations. The thesis focus on the possible research on both models at the Belle II experiment. Belle II is an experiment installed on the SuperKEKB accelerator, in which asymmetric beams of electrons and positrons collide with a center of mass energy matching the $\Upsilon(4S)$ mass. Belle II belongs to the *B-factory* class of experiments, and has features such as clean environment which allows it to be important in the search of new physics .

The work of the thesis is organized as follows: in chapter 1 there is a brief overview of the standard model theory, the description of the three types of interactions and the explanation of CP violation in the weak interactions, followed by the addressed open problems. In chapter 2 the lagrangian for axion-like particles is introduced, and also a list of experimental possibilities to probe for generic ALP particles and the existing limits on different couplings to standard model particles. In chapter 3 the realization as QCD axion model in the MeV/c^2 mass range is explained and existing limits are reviewed; in chapter 4 there is the description for the ALP as dark matter candidate, proposed with freeze-in mechanism as production mechanism. In chapter 5 the *B-factory* and Belle II experiment are presented, with a description of the most important elements of the detector. In chapter 6 there is explanation of the simulation made for the channel $e^+e^- \rightarrow \gamma a$ which can be important to probe sensitivity of Belle II for the QCD axion model. Finally in chapter 7 there is the review of a Belle II study on the

channel $\tau \rightarrow l \alpha$ which is interesting for the ALP model as dark matter candidate, and the results are compared with the prediction of the model.

1. Theoretical overview

In this chapter there is a summary of the Standard Model, of the particles it describes and the interactions between them. The model can explain a great deal of physical phenomena, but it is not complete because of some remaining issues it cannot describe. In this chapter there is an overview mainly on two problems still not explained by the SM. One is relative to the behaviour of the strong interactions under *charge conjugation* C and *parity* P symmetry, also referred to as the *strong CP problem*. In the model, the strong force theory contains a term violating CP symmetry proportional to an angular parameter θ . The experimental searches for such violation put a stringent upper limit on θ , forcing its value to be almost zero. The Standard Model does not provide a mechanism explaining why the parameter has such a little value. Another problem is the description and explanation of dark matter (DM). This type of matter gives evidence of itself through gravitational effects, and is considered to be a fair portion of existing matter ($\sim 24\%$). In this chapter there is a reminder of dark matter characteristics, on the possible production mechanisms and the possible particle candidates of which it could be composed of.

1.1 SM description

The Standard Model (SM) is the set of theories which describe the constituent of matter and the fundamental forces acting between them. It identifies leptons and quarks as building blocks of matter, and it is able to describe three of the four forces of which they are affected: electromagnetic, weak and strong force. Leptons can interact electromagnetically and weakly, while quarks are affected by all three forces. The Standard Model is a gauge theory. In such theories the way particles interact is by mutual exchange of other particles called mediators. A mediator is therefore the quantum permitting the specific interaction, and they appear naturally in the theory by requiring a gauge invariant model. The first theory developed in this sense was quantum electrodynamics (QED)

Types of particles

Particles are divided into two subgroups based on the spin value: bosons are particles with an integer spin ($S=0,1,2,\dots$); fermions are particles with fractional spin ($S=\frac{1}{2}, \frac{3}{2}, \dots$). In the SM, the fundamental particles are fermions, which are leptons and quarks. Leptons undergo electromagnetic and weak force, and they come in three generations: (e, ν_e) , (μ, ν_μ) and (τ, ν_τ) . For each lepton generation there is a quantum number L called leptonic number. Also quarks come in three generations: (u, d) , (c, s) and (t, b) .

Quarks undergo all three types of forces, and are characterized by a fractional electromagnetic charge. Quarks have an ulterior quantum number called *color* arising in the strong interactions. Though color has been proven to exist, only colorless particles or combinations of particles can be seen. This is explained through a phenomenon called *color-confinement*, which is responsible for the grouping of quarks into neutral color combinations: mesons (two quark state) and baryons (three quark state) are the simplest colorless particles we observe in nature.

For each lepton and quark there exists an *anti-particle*, which has the same properties but all quantum numbers of opposite sign. Furthermore, both leptons and quarks have two *chiral* components: the *left-handed* component and the *right-handed* one. Weak interaction is the only interaction sensible to such decomposition, and acts only on left-handed particles (right-handed antiparticles).

Three fundamental forces

The electromagnetic, weak and strong interactions are mediated respectively from: photons, massive vector bosons and gluons. The mediators arise from the gauge invariance of the theory, but while the photon and gluon are massless, the weak mediators are massive: $W^\pm = 80.4 \text{ GeV}/c^2$ and $Z = 91.2 \text{ GeV}/c^2$. Furthermore also gluons and photons are very different: the latter gives rise to a force with infinite range thanks to its zero mass; while, even if massless, gluons give rise to a short range interaction. This again can be explained through color-confinement: gluons are colored and can be exchanged only between other colored particles - like quarks - but such particles are confined, hence the short range of the interaction.

Although the difference between the mediators, two of the three forces have been successfully described in a unified theory: electromagnetic and weak interactions can be described both by the electroweak model.

1.1.1 Standard Model as Gauge theory

The Standard Model is a gauge theory with a local group symmetry given by $U(1)_Y \otimes SU(2)_L \otimes SU(3)_C$. The first two groups describe the electroweak sector, which is the unified theory of weak and electromagnetic interactions; the last one gives rise to the strong interactions. The group $U(1)_Y$ represents a phase redefinition of the fields, while $SU(2)_L$ acts on the left components of particles (from this the prefix L). Because of this symmetry, leptons and quarks are organized in doublets and singlets under $SU(2)_L$:

$$\psi_L^i : l_L^i = \begin{pmatrix} \nu^i \\ e^i \end{pmatrix}_L \quad q_L^i = \begin{pmatrix} u^i \\ d^i \end{pmatrix}_L \quad \psi_R^i : e_R^i \quad u_R^i \quad d_R^i \quad (1.1)$$

where the index i runs on all three generations both for leptons and quarks. The $U(1)_Y \otimes SU(2)_L$ group symmetry introduces four vector gauge fields : B_μ for $U(1)_Y$ and W_μ^a with $a=1,2,3$ for $SU(2)_L$.

The strong interaction is described by a non-Abelian gauge group given by $SU(3)_C$, where the subscript C stands for color. This gauge group introduces eight vector gauge fields G_μ^α where $\alpha = 1 \dots 8$, which are the eight different gluons, mediators of the strong force.

The Standard Model lagrangian does not introduce an explicit mass term for the particles, because such term would break the group symmetry. The way the mass is introduced is thanks to the *Higgs mechanism*, explained in the next paragraph. This mechanism exploits the presence of a scalar doublet ϕ with a vacuum expectation value given from a quartic potential $V(\phi^\dagger \phi)$ which breaks the $U(1)_Y \otimes SU(2)_L$ symmetry group into the $U(1)_{EM}$ sub-group. The interaction with ϕ determine the mass term for the all the fields, except for the photon field which must remain massless.

Thus, along with the leptons and quarks previously listed, there are 12 mediators plus one scalar field which form the base in the Standard Model. They are listed in table 1.1.

| | | | |
|----------|-----|-------------------------|-----------------------------|
| γ | S=1 | 0 GeV/c ² | electromagnetic interaction |
| W^\pm | S=1 | 80.4 GeV/c ² | weak interaction |
| Z | S=1 | 91.2 GeV/c ² | weak interaction |
| g | S=1 | 0 GeV/c ² | strong interaction |
| h | S=0 | 125 GeV/c ² | Higg field |

Table 1.1: Bosons mediators of the three fundamental forces plus the Higgs field. For each particle the spin S and mass value is listed. Mass values taken from PDG [1]

The lagrangian including all three forces plus the Higgs field is given by [2]:

$$\mathcal{L} = \mathcal{L}_{kin} + \mathcal{L}_H + \mathcal{L}_{EW} + \mathcal{L}_Y + \mathcal{L}_{QCD} \quad (1.2)$$

The remaining part of this section will concentrate on the electroweak sector \mathcal{L}_{EW} and the Yukawa interaction in \mathcal{L}_Y , from which the violation of CP-parity arise; the strong interaction in \mathcal{L}_{QCD} is described in the next section.

1.1.2 Electroweak sector

The \mathcal{L}_{kin} indicates the kinetic and self-interaction terms for the gauge fields:

$$\mathcal{L}_{kin} = -\frac{1}{4}B_{\mu\nu}B^{\mu\nu} - \frac{1}{4}W_{\mu\nu}^a W_a^{\mu\nu} \quad (1.3)$$

The derivative coupling D_μ in terms of B_μ and W_μ^a is written as:

$$D_\mu = \partial_\mu + ig \frac{\tau_a}{2} W_\mu^a + ig' \frac{Y}{2} B_\mu \quad (1.4)$$

where τ_a are the three generators of $SU(2)_L$, Y is the $U(1)_Y$ generator, and g, g' the couplings associated to the fields.

The electromagnetic field A_μ and the weak ones Z_μ and W_μ^\pm can be expressed through the B_μ and W_μ^a fields in the following way:

$$W^\pm = \frac{1}{\sqrt{2}}(W_\mu^1 \mp iW_\mu^2), \quad Z_\mu = \cos \theta_w W_\mu^3 - \sin \theta_w B_\mu, \quad A_\mu = \cos \theta_w B_\mu + \sin \theta_w W_\mu^3 \quad (1.5)$$

The angle θ_w is the Weinberg angle describing the rotation between the (B_μ, W_μ^a) and $(W_\mu^\pm, Z_\mu, A_\mu)$ basis. It represents a fundamental parameter of the theory and it can be expressed through the coupling parameters as: $\tan(\theta_w) = g'/g$.

\mathcal{L}_H is the lagrangian term for the scalar doublet ϕ :

$$\mathcal{L}_H = |D_\mu \phi|^2 - V(\phi^\dagger \phi) \quad (1.6)$$

$$V(\phi^\dagger \phi) = \mu^2 \phi^\dagger \phi + \frac{\lambda}{2} (\phi^\dagger \phi)^2 \quad (1.7)$$

where the parameters in $V(\phi^\dagger \phi)$ are $\mu < 0$, $\lambda > 0$.

The scalar doublet is composed by two complex fields $\phi = (\phi^\dagger, \phi^0)$ so it has four degrees of freedom. The potential $V(\phi^\dagger \phi)$ has a non-invariant ground state under the symmetry group $U(1) \otimes SU(2)_L$, because ϕ acquires a vacuum expectation value (VEV) v . The value $v = 246 \text{ GeV}$ is indicated as the electroweak (EW) scale. On the ground state, the doublet can be written as :

$$\phi = \frac{e^{i\lambda_a \tau_a / 2v}}{\sqrt{2}} \begin{pmatrix} 0 \\ v+h \end{pmatrix} \quad (1.8)$$

where λ_a and h are four fields, where h is properly the Higgs field. The exponential part can be gauged away, so in the end ϕ in the ground state is :

$$\phi = \frac{1}{\sqrt{2}} \begin{pmatrix} 0 \\ v+h \end{pmatrix} \quad (1.9)$$

In \mathcal{L}_H the term $\mu^2 h^2$ represents the mass term for the Higgs field $m_h = 125 \text{ GeV}/c^2$.

Through the derivative coupling D_μ the boson fields W^\pm, Z interact with ϕ and gain mass :

$$M_{W^\pm} = v \frac{g}{\sqrt{2}} \quad M_Z = v \frac{\sqrt{g^2 + g'^2}}{\sqrt{2}} \quad (1.10)$$

The field A_μ does not have such a coupling, thus it remains massless. It is associated to the photon field, the boson field of the residual symmetry $U(1)_{EM}$. The

fermion fields gain mass through an interaction like $\bar{\psi}_L^i \tilde{\phi} \psi_R$ written explicitly in \mathcal{L}_Y .

The \mathcal{L}_{EW} describes the interaction between the electroweak fields and the fermion fields ψ :

$$\mathcal{L}_{EW} = \mathcal{L}_{kin} + e(W_\mu^+ J_+^\mu + W_\mu^- J_-^\mu + Z_\mu^0 J_0^\mu + A_\mu J_{EM}^\mu) \quad (1.11)$$

Where \mathcal{L}_{kin} represents the kinetic term for the fermions; J_\pm^μ are the weakly charged currents, J_0 is the neutral one and J_{EM}^μ the electromagnetic current. Their expressions are:

$$J_+^\mu = \frac{1}{\sqrt{2}}(\bar{\nu}_L^i \gamma^\mu e_L^i + \bar{u}_L^i \gamma^\mu d_L^i) \quad J_-^\mu = \frac{1}{\sqrt{2}}(\bar{e}_L^i \gamma^\mu \nu_L^i + \bar{d}_L^i \gamma^\mu u_L^i) \quad (1.12)$$

$$J_0^\mu = \frac{1}{2 \cos \theta_w \sin \theta_w}(\bar{l}_L^i \sigma^3 \gamma^\mu l_L^i + \bar{q}_L^i \sigma^3 \gamma^\mu q_L^i) - \tan \theta_w J_{EM}^\mu \quad (1.13)$$

$$J_{EM}^\mu = (-\bar{e}^i \gamma^\mu e^i + \frac{2}{3} \bar{u}^i \gamma^\mu u^i - \frac{1}{3} \bar{d}^i \gamma^\mu d^i) \quad (1.14)$$

with σ^3 the third Pauli matrix and the apex i runs on all three generations both for leptons and quarks.

1.1.3 Yukawa interaction and mass term

The Yukawa term \mathcal{L}_Y represents the interaction between the fermions ψ and the pseudoscalar doublet ϕ through which fermions gain mass.

$$\mathcal{L}_Y^q = \bar{q}_L^i Y_{ij}^u u_R^j \tilde{\phi} + \bar{q}_L^i Y_{ij}^d d_R^j \phi + h.c. \quad (1.15)$$

$$\mathcal{L}_Y^l = \bar{l}_L^i Y_{ij}^e e_R^j \phi + h.c. \quad (1.16)$$

The mass matrices Y_{ij} are allowed to have non-diagonal elements, in their most generic form. This implies possible mixing between particles in the mass term. In order to have a diagonalized mass term, it is possible to write Y_{ij} in a diagonal form using two unitary matrices U and W :

$$Y_{u,d,l} = U_{u,d,l} y_{u,d,l} W_{u,d,l}^\dagger \quad (1.17)$$

where $y_{u,d,l}$ is a diagonal matrix with real positive eigenvalues.

The U, W matrices can be re-absorbed in \mathcal{L}_Y by a redefinition of the right-handed fields as:

$$u_R^i \rightarrow W_u^{ij} u_R^j, \quad d_R^i \rightarrow W_d^{ij} d_R^j, \quad e_R^i \rightarrow W_R^{ij} e_R^j \quad (1.18)$$

and the left-handed fields:

$$u_L^i \rightarrow U_u^{ij} u_L^j, \quad d_L^i \rightarrow U_d^{ij} d_L^j, \quad e_L^i \rightarrow U_l^{ij} e_L^j, \quad \nu_L^i \rightarrow U_\nu^{ij} \nu_L^j \quad (1.19)$$

in the expressions for J_{EM}^μ and J_0^μ the W and U matrix cancel out. The leptonic sector in the charged weak currents is invariant under the rotation U_l , whereas for the quark sector :

$$J_+^\mu = \frac{1}{\sqrt{2}} \bar{u}_L^i \gamma^\mu (U_u^\dagger U_d)_{ij} d_L^j \quad J_-^\mu = \frac{1}{\sqrt{2}} \bar{d}_L^i \gamma^\mu (U_d^\dagger U_u)_{ij} u_L^j \quad (1.20)$$

The rotation performed on the fields in order to diagonalize the mass matrix gives raise to a new matrix: the *Cabibbo-Kobayashi-Maskawa* matrix $V_{CKM} = U_u^\dagger U_d$. It represents the misalignment between the mass basis and the interaction basis for the quark fields.

The V_{CKM} is a 3x3 unitary matrix usually parameterized as in [1]:

$$V_{CKM} = \begin{pmatrix} c_{12}c_{13} & s_{12}c_{13} & s_{13}e^{i\delta} \\ -s_{12}c_{13} - c_{12}s_{13}s_{23}e^{i\delta} & c_{12}c_{23} - s_{12}s_{13}s_{23}e^{i\delta} & c_{13}s_{23} \\ s_{12}s_{23} - c_{12}s_{13}c_{23}e^{i\delta} & -c_{12}s_{23} - s_{12}s_{13}c_{23}e^{i\delta} & c_{13}c_{23} \end{pmatrix} \quad (1.21)$$

The abbreviation s_{ij} and c_{ij} stand for $\sin \theta_{ij}$ and $\cos \theta_{ij}$. The free parameters are made explicit: three real angles θ_{ij} which represent the rotation angles between the interaction basis and mass basis for the quarks; and one complex phase $i\delta$. As explained in the next subsection, the complex phase $i\delta$ is responsible for the CP violation of flavor-changing processes in weak interactions.

1.1.4 CP violation in the electroweak interactions

Charge conjugation C and parity P are two discrete symmetries under which fields and their combinations can have eigenvalue +1 (in case of symmetry) or -1 (not symmetric). The effect of P and C on the chiral components of the fermion fields are listed in table 1.2:

| | P | C |
|----------|----------|------------------------|
| ψ_L | ψ_R | $i \sigma^2 \psi_R^*$ |
| ψ_R | ψ_L | $-i \sigma^2 \psi_L^*$ |

Table 1.2: Effect of P and C operators on the chiral components of fermion fields.

The combination of fermion fields ψ and dirac matrices γ_μ are bilinears classified as in the first row of the table 1.3. In the same table are also listed the eigenvalues of each bilinear under the effect of C and P operators.

The effects of C and P operators on the bilinears entering the weak charged cur-

| | scalars $\bar{\psi}\psi$ | pseudoscalars $\bar{\psi}\gamma_5\psi$ | vectors $\bar{\psi}\gamma_\mu\psi$ | pseudovectors $\bar{\psi}\gamma_\mu\gamma_5\psi$ | tensors $\bar{\psi}\sigma_{\mu\nu}\psi$ |
|---|-----------------------------|---|---------------------------------------|---|--|
| C | +1 | +1 | -1 | +1 | -1 |
| P | +1 | -1 | +1 | -1 | +1 |

Table 1.3: Eigenvalues of the different combination of fields.

rents $W_\mu^\pm J_\pm^\mu$ are:

$$\begin{aligned}
\mathcal{L}_{EW}^\pm &= \bar{e}_L^i \gamma^\mu v_L^i W_\mu^- + h.c. + \bar{u}_L^i \gamma^\mu V_{ij} d_L^j W_\mu^- + \bar{d}_L^i \gamma^\mu V_{ij}^\dagger u_L^j W_\mu^+ \\
P\mathcal{L}_{EW}^\pm &= \bar{e}_R^i \gamma^\mu v_R^i W_\mu^- + h.c. + \bar{u}_R^i \gamma^\mu V_{ij} d_R^j W_\mu^- + \bar{d}_R^i \gamma^\mu V_{ij}^\dagger u_R^j W_\mu^+ \\
C\mathcal{L}_{EW}^\pm &= \bar{e}_R^i \gamma^\mu v_R^i W_\mu^- + h.c. + \bar{u}_R^i \gamma^\mu V_{ij}^\dagger d_R^j W_\mu^- + \bar{d}_R^i \gamma^\mu V_{ij} u_R^j W_\mu^+
\end{aligned} \tag{1.22}$$

In the lagrangian the C,P and CP symmetries are violated because of the physical phase in the V_{CKM} matrix. In fact the V_{CKM} matrix is not hermitian $V_{ij} \neq V_{ij}^\dagger$ because of the complex phase. This is the reason why CP parity is violated in the weak charged processes.

An other useful parametrization of V_{CKM} matrix is the Wolfenstein one [1], in the parameter space given by (A, λ, ρ, η) :

$$V = \begin{pmatrix} 1 - \frac{1}{2}\lambda^2 & \lambda & A\lambda^3(\rho - i\eta) \\ -\lambda & 1 - \frac{1}{2}\lambda^2 & A\lambda^2 \\ A\lambda^3(1 - \rho - i\eta) & -A\lambda^2 & 1 \end{pmatrix} + o(\lambda^4) \tag{1.23}$$

The parameter λ is the sine of the mixing angle between u and d quark, so $\lambda = 0.22$. Written in this way, it is easy to see that, in the weak charged currents, the transitions between particles of the same generation have a probability almost one (the diagonal elements); while transitions between different generations (out of diagonal elements) are more and more suppressed because of the small value of λ .

The unitary conditions for the V_{CKM} matrix $V_{ij}V_{ij}^* = 1$ lead to nine equations which regulate the probability of the transitions, for example :

- $V_{ud}V_{ud}^* + V_{us}V_{us}^* + V_{ub}V_{ub}^* = 1$ means the probability of transitioning from a u quark to a d quark type is one.
- $V_{ud}V_{us}^* + V_{cd}V_{cb}^* + V_{td}V_{ts}^* = 0$ means there is no possibility of transitioning between a d quarks and a s quark type at tree level.

These equations $\sum_{ijk} V_{ij}V_{ik}^* = 0$ ($j \neq k$) compose a triangle in the plane (ρ, η) as shown in figure 1.1:

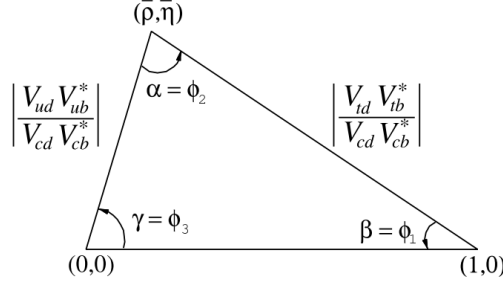


Figure 1.1: Unitary triangle for the equation $V_{ud}V_{ub}^* + V_{cd}V_{cb}^* + V_{td}V_{tb}^* = 0$. The triangles sides are normalized with $V_{cd}V_{cb}^*$ and the angles are : $\alpha = \arg \frac{V_{ud}V_{ub}^*}{V_{td}V_{tb}^*}$, $\beta = \arg \frac{V_{td}V_{tb}^*}{V_{cd}V_{cb}^*}$, $\gamma = \arg \frac{V_{cd}V_{cb}^*}{V_{ud}V_{ub}^*}$

The measure of the three angles represent an important test for the Standard Model and therefore a source of new physics. This type of study is conducted in devoted experiments, mostly collider type experiments as later described.

1.1.5 Open problems

The Standard Model has been studied for the last 50 years, and so far has been able to explain a great deal of phenomena. Nonetheless it is know that it remains an incomplete theory: a modern intuition sees the SM as an effective theory, the low energy expression of a greater and more complete theory. The model should be expanded in order to contain new fields and interactions necessary to explain some open problems remaining. A few examples of open problems are :

- explanation of the number of generations both of leptons and quark families
- explanations of the mass hierarchy between the fermion generations
- explanation of the diagonal hierarchy in the structure of the V_{CKM} matrix.
- explanation for dark matter (DM) nature
- the CP-violation term in the strong interactions

As anticipated, the thesis will concentrate on the last two open questions, and will study model proposal for both problems. The way these problems are usually dealt with is by an enlargement of the standard model through new fields and interactions, which give new models indicated as Beyond Standard Model (BSM) models.

1.2 CP parity problem in the strong interactions

In this section there is an explanation about the strong CP problem, and, along with it, one of the most promising models proposed as a solution of such problem: the Peccei-Quinn (PQ) model. The model predicts the existence of a new particle, the axion, whose main characteristics are here described.

1.2.1 Strong interactions

The strong interaction affect the fermions interacting with the gluon fields, and it is described in the \mathcal{L}_{QCD} term, here written as in [3] where the gluon fields are A_μ :

$$\mathcal{L}_{QCD} = \sum_f^{N_f} \bar{q}_f \left(\gamma^\mu i D_\mu - m_f \right) q_f - \frac{1}{4} G_{\mu\nu}^a G_a^{\mu\nu} \quad (1.24)$$

$$G_{\mu\nu} = \partial_\mu A_\nu - \partial_\nu A_\mu - ig_s [A_\mu, A_\nu], \quad D_\mu = \partial_\mu - g_s A_\mu^a T_a \quad (1.25)$$

where g_s is the strong coupling constant, N_f is the number of quark flavours, a runs from 1 to 8 and T_a are the eight generators of the $SU(3)_C$ symmetry group. The lagrangian is symmetric under a $U(1)$ transformation for each quark field, thus it conserves flavor. It also conserves C,P and T.

In the limit of m_f approaching zero, the lagrangian is symmetric under the *chiral group* $U(N_f)_L \otimes U(N_f)_R$, which can be decomposed as $SU(N_f)_L \otimes SU(N_f)_R \otimes U(1)_L \otimes U(1)_R$. The subscripts L and R indicate the chiral component of the fields. A mass term would break such symmetry group because it would mix the left and right chiral components of the fields.

The \mathcal{L}_{QCD} could also contain a renormalizable term such as:

$$G_{\mu\nu} \tilde{G}^{\mu\nu} \quad , \quad \tilde{G}_{\mu\nu} = \frac{1}{2} \varepsilon_{\mu\nu\rho\sigma} G^{\rho\sigma} \quad (1.26)$$

This term had been discarded because it can be written as the quadri-divergence of a current called *Chew-Simons* current :

$$K_\mu = \varepsilon_{\mu\nu\rho\sigma} tr [A_\nu^a G_{\rho\sigma}^a - \frac{g_s}{3} f^{abc} A_\nu^a A_\rho^b A_\sigma^c] \quad (1.27)$$

$$\partial_\mu K^\mu = G_{\mu\nu}^a \tilde{G}_a^{\mu\nu} \quad (1.28)$$

In such a case, the action would not feel the effect of the operator in equation 1.26, because performing an integration over all space-time of the quadri-divergence $\partial_\mu K^\mu$ results in a vanishing contribute.

However, in the paper [4] the authors describe a class of gauge fields with non-trivial topological properties and with a finite action for which the lagrangian term in

equation 1.26 does not vanish. These gauge configurations are called *instantons*. Because of the complexity of non abelian group vacuum state, such gauge configurations must be inserted in the action regulating the path integral between different states. As a result, the effective lagrangian becomes :

$$\mathcal{L}_{eff} = \mathcal{L}_{QCD} + \frac{\theta g_s^2}{32\pi^2} G_{\mu\nu} \tilde{G}^{\mu\nu} \quad (1.29)$$

where $\theta \in [0, 2\pi)$ is an angular parameter.

1.2.2 CP violating term

In the strong interactions there are two sources of CP-parity violation. One is given by the possible phase in the quark mass matrix due to the Yukawa coupling as seen previously. The other source is in the $G\tilde{G}$ term introduced in equation 1.29, because the tensor $\varepsilon^{\mu\nu\rho\sigma}$ breaks CP-parity. The combination of these two sources with physical meaning is [5]:

$$\theta_{phys} = \theta + \arg(\det(m)) \quad (1.30)$$

because a chiral rotation such as $e^{i\gamma_5\alpha}$ would have an effect on both theta and the mass term as:

$$\theta \rightarrow \theta - \alpha \quad \arg(\det(m)) \rightarrow \arg(\det(m)) + \alpha \quad (1.31)$$

An observable sensible to the physical quantity in equation 1.30 is the neutron electric dipole moment (nEDM), as said in [6]. The neutron spin \mathbf{S} interacts with an external electric field \mathbf{E} as described by the non-relativistic hamiltonian :

$$H = -d_n \mathbf{E} \frac{\mathbf{S}}{S} \quad (1.32)$$

where d_n is the nEDM. The hamiltonian term breaks CP because the electric field is a vector while the spin is a pseudo-vector quantity. The θ_{phys} enters the d_n term through the relation [6]:

$$d_n(\theta) = 2.4 \cdot 10^{-16} \theta_{phys} \cdot e \cdot \text{cm} \quad (1.33)$$

which yields an upper limit for the physical angular parameter:

$$|\theta_{phys}| < 3 \cdot 10^{-10}. \quad (1.34)$$

There is no prediction for the value of θ_{phys} and having it almost zero does assure CP symmetry. Nonetheless such a stringent upper limit, which implies a very small symmetry breaking, puzzle physicists, and is addressed as a *fine-tuning* problem. To sum up, after the discovery of instantons, the strong interactions include a CP violating term given by the combination of a mass-matrix phase and an angular parameter related to the vacuum of the QCD. Despite the necessity of them both, the two sources cancel out almost completely, leaving a θ_{phys} extremely small.

1.2.3 Peccei-Quinn mechanism

There is the necessity to find a convincing mechanism explaining why the θ and $\arg(\det(m))$ should cancel out at a precision of $O(10^{-10})$.

One of the most interesting explanations comes from the model proposed by Peccei and Quinn [5], [7], with also the contributions of Weinberg and Wilczek [8], [9].

In their model, the effective angle θ_{eff} is zero no matter which was the initial value of θ

They introduce a new global symmetry, referred to as $U(1)_{PQ}$, which is broken by instantons effects at an energy scale f_a . From this broken symmetry a new degree of freedom arises in the spectrum: a pseudo-scalar neutral and spin zero boson named *axion*. In the lagrangian, the axion field a couples to an operator of the form $G\tilde{G}$ and the other fields as in equation 1.35 ([10]):

$$\mathcal{L}_a = \frac{1}{2}(\partial_\mu a)^2 + \mathcal{L}(\psi, a) + \frac{1}{4}g_{a\gamma}^0 a F \tilde{F} + \frac{g_s^2}{32\pi^2} \frac{a}{f_a} G_\mu \tilde{G}^\mu \quad (1.35)$$

The first term is the kinetic part for the axion, while $\mathcal{L}(\psi, a)$ contains the derivative interaction with the fermion fields and will be made explicit later. The $aF\tilde{F}$ encodes the axion-photon coupling, through a factor $g_{a\gamma}^0$ which is dimensional. The lagrangian is written after electroweak symmetry breaking.

The effect of $U(1)_{PQ}$ on the axion field is a shift : $a \rightarrow a' = a + k \cdot f_a$ so it is possible to choose k in such a way to eliminate the $G\tilde{G}$ in equation 1.29. In [11] it is shown that the axion potential $V(a)$ is minimized for $\langle a \rangle = 0$. After the shift of the axion field, the two $G\tilde{G}$ terms are canceled out, so to choose the vacuum with $\theta = 0$ does not have physical consequences. With a chiral transformation it is possible to compute the real diagonalized mass matrix for the quark fields, meaning that also the $\arg(\det(m)) = 0$. From this it is immediate that the CP-violating source θ_{phys} is zero.

In the original PQ model the axion is a phase direction in the standard Higgs doublet. In order to have the necessary degrees of freedom, the SM contains two Higgs doublets ϕ_1 and ϕ_2 which couple to SM fields as in the Higgs mechanism. They break the $U(1)_Y \otimes SU(2)_L \otimes U(1)_{PQ}$ symmetry group when they acquire a vacuum expectation value $\langle \phi_1^0 \rangle = v_1$ and $\langle \phi_2^0 \rangle = v_2$ so that $v_{EW} = \sqrt{v_1^2 + v_2^2}$. Thus the energy scale $f_a = 245 \text{ GeV}$. The axion in this original model is *visible* because it couples only to Standard Model fields and produce visible final states in the experiments.

1.2.4 Search for axions

In order to believe the PQWW or a similar mechanism one should proof the existence of the axion. The tools to be used in the search vary depending on the mass of the particle.

For the QCD axion, a mass term arises from the mixing between the a and π field.

At energy scales of $1 \div 2\text{GeV}$ (well below the EW scale) the only degrees of freedom in the quark sector are the lightest quarks u, d and s . For a phenomenology at low energies, one can re-write the effective lagrangian using chiral lagrangian techniques [12], [13]. In this case, in order to describe the axion-gluon bosonized interaction, the $aG\tilde{G}$ term is eliminated through a chiral rotation of the fermion fields :

$$\psi \rightarrow e^{i\gamma_5 Q_a \frac{a}{2f_a}} \psi \quad (1.36)$$

where Q_a is a matrix acting on quark fields. The rotation induces an anomaly term:

$$\frac{-g_s}{32\pi^2} Tr[Q_a] \frac{a}{f_a} G\tilde{G} \quad (1.37)$$

which, by the choice of $Tr[Q_a] = 1$, allows to eliminate the $aG\tilde{G}$ operator in the lagrangian in equation 1.35. The rotation also effects the $g_{a\gamma}^0$ coupling and the mass term M_q of the quark fields as:

$$g_{a\gamma} = g_{a\gamma}^0 - \frac{\alpha}{2\pi f_a} 2N Tr[Q_a Q^2] \quad (1.38)$$

$$M_a = e^{i\frac{a}{2f_a} Q_a} M_q e^{i\frac{a}{2f_a} Q_a} \quad (1.39)$$

The non-derivative coupling between axion and quarks have been shifted in the mass matrix M_a .

The matching onto the chiral lagrangian is possible by considering the M_a mass term in expression above and taking the axion-quark bilinear couplings as :

$$\bar{q}_L^i \gamma_\mu q_L^j \rightarrow \frac{if_\pi^2}{4} [UD_\mu U^\dagger]^{ij} \quad \bar{q}_R^i \gamma_\mu q_R^j \rightarrow \frac{if_\pi^2}{4} [U^\dagger D_\mu U]^{ji} \quad (1.40)$$

The operator $U = e^{i\pi^a \lambda^a / f_\pi}$ contains the effective Goldstone bosons, that is the pion fields; λ^a are the Gell-Mann matrices, $f_\pi = 92.3\text{MeV}$ is the pion decay constant and D_μ is the covariant derivative

At first order of $1/f_a$ the chiral lagrangian is:

$$\mathcal{L}^\chi = \frac{f_\pi^2}{4} [Tr((D^\mu U)^\dagger D^\mu U) + 2B_0 Tr[UM_a^\dagger + M_a U^\dagger]] + \mathcal{L}^\chi(\partial_\mu a, J_a^\mu) \quad (1.41)$$

where is related to the B_0 the quark condensate and the axion-quark copling is in \mathcal{L}^χ .

Using this expression for the lagrangian and taking only the first order, a mass term for the axion arises from the coupling with the lightest quarks ([10], [13]). The mass m_a of the axion can be computed as :

$$m_a \simeq 5.7 \left(\frac{10^{12} \text{GeV}}{f_a} \right) \mu\text{eV} \quad (1.42)$$

where it is clear that the value of m_a depends on the value of the breaking energy scale. This is an important feature of the QCD axion. In the original work of PQWW, the scale is taken $f_a = 245 \text{GeV}$, so it describes an axion with mass in the MeV/c^2 range. The PQWW axion, which should be visible because it couples to SM fields, has been discarded because of experimental results and constraints. Although the original PQWW axion is dead, the idea is still interesting. Other models have been proposed based on the same mechanism but introducing new physics at higher energies ($\sim \text{TeV}$). These axions in these models acquire light mass and have SM couplings way suppressed, thus they usually are *invisible* axions.

In chapter 3 a work made in 2020 shows how a possible model for an axion in the MeV/c^2 still survives thanks to a particular choice of the axion-fermion couplings.

The search for this new particle and so the confirmation of the Peccei-Quinn idea is still an open challenge.

1.3 Introduction to Dark Matter

Dark matter (DM) is the name indicating a new type of matter, which is *dark* meaning that it interacts too little with the light to be discovered through electromagnetic interaction. This new type of matter was firstly considered to explain the observed rotational velocity of galaxies in the Coma cluster in 1933. Galaxies are composed by a central bulk with stars spinning around it in almost circular orbits. From Keplers second law, it is expected that the rotation velocities decrease as the distance from the center increases, but this is in contradiction with the velocities actually observed [14]. As a matter of fact, the observed galaxy rotation curve remains flat as distance from the center increases: this implies the existence of ulterior matter in the galaxy.

Another necessity for new matter comes from the mechanism of structure formation. This refers to the period during which the fluctuations of the homogeneous Universe collapsed to form galaxies and other structures. The Cosmic Background Explorer (COBE) detected the fluctuations in the cosmic microwave background, which result extremely small. In an Universe composed only by barionic/fermionic matter, such small fluctuations would have been "washed away" by the interaction with radiation, the dominant matter in the early Universe. This calls for an other type of matter, unaffected by electromagnetic interaction but still interacts through gravity. With such properties, even small perturbations of such matter could have grown and, thanks to

gravitational interaction, act as a potential well helping in the collapse process of ordinary matter [15].

There are several formulations regarding the DM nature, most of which predict it to have a particle composition.

Other than electrically neutral, a particle candidate as dark matter must also be stable on the time-scale of the Universe. The Universe has a lifetime of $\tau \sim 10^{18}$ s ([16]). The stability on this time-scale is required because if the particle candidate were to decay into SM particles, it would cause fluxes of cosmic positrons, antiprotons and photons larger than the observed ones [17], [18].

In this thesis the main focus will be on particle nature of dark matter.

1.3.1 Dark matter formation and candidates

The Universe is a homogeneous and isotropic space which expands in time, described by the *Friedman-Roberston-Walker* equations [16] The expansion rate of the Universe is encoded in the Hubble parameter $H(t)$.

During the time evolution of the Universe, particles can be at equilibrium or out of equilibrium between them. For a particle specie, the equilibrium is reached when its interaction rate $\Gamma(t)$, which keeps in account for every scattering process the particle can do as well as its decay, is greater than the expansion rate $H(t)$. At equilibrium, every process has the same probability to happen in both directions, and the particles in this condition are referred to as bath particles.

The number density n and the energy density ρ of a particle at equilibrium can be determined using the formulas :

$$n_i = \frac{g_i}{2\pi^3} \int f_i(p) d^3 p \quad \rho_i = \frac{g_i}{2\pi^3} \int E_i(p) f_i(p) d^3 p \quad (1.43)$$

where g_i is the number of spin states of the particle specie and $f_i(p)$ the *probability distribution function* of its momentum p . The value of $f_i(p)$ are determined by the Maxwell-Boltzmann equations, and the integrals in the above expressions are carried out into two opposite limits. One is the *relativistic* limit, when the mass m of the particle and the temperature of the universe T satisfy $T \gg m$; the opposite *non-relativistic* limit is when $T \ll m$.

Eventually the values of n and ρ become fixed when the particle ceases to interact. For every particle specie, one can define the relic abundance as $\Omega_i = \rho_i / \rho_{crit}$ where $\rho_{crit} = \frac{3H^2}{8\pi G}$. The DM abundance has been measured by the Planck collaboration as stated in [19] and is $\Omega_{CDM} h^2 = 0.12$. For any particle proposed as DM candidate, an important check is to see if its relic abundance agrees with the present DM abundance.

Different candidates can be proposed with different production mechanism. Here three main type of production mechanism are explained: two are *thermal* mechanism, meaning that it involves the interaction between the produced particle and the bath

particles, and one is *non-thermal* meaning that it has another type of explanation not involving bath particles.

It is important that the DM is produced as *cold*-dark matter (non-relativistic) instead of *hot*-dark matter (relativistic). This is necessary for the role DM plays in the structure formation. Dark matter produced as *hot* has large velocities, causing it to free-stream out of overdense regions, diminishing primordial perturbations and thus altering the structure formation.

Thermal production

A particle X is thermally produced when its abundance is reached after it interacted with the bath particles. The particle X can be formulated with a great initial abundance and at equilibrium with the bath particles. Once the total interaction rate Γ between X and the bath particles is smaller than $H(t)$, the particle X exits the equilibrium. Its density does not vary anymore, and this production mechanism is said *freeze-out* mechanism.

A similar mechanism is the *freeze-in* one. This one also considers the interactions between the produced particle X and the bath particles, but the initial X density is very small and the particle specie is never at equilibrium. The particle X can be produced for example by the decay of the other particles in the bath, and once this latter exits equilibrium also the production of X stops.

A visual example of *freeze-out* and *freeze-in* mechanism is given in figure 1.2.

Non-thermal production

An example of *non-thermal* production can be the *misalignment* mechanism [21]. This mechanism can be used to describe the production of a scalar field ϕ with a potential $V(\phi)$. It relates on the behaviour of the field at different temperatures T of the Universe.

For a scalar field, the equation of motion in a Robertson-Walker metric is given by: $\ddot{\phi} + 3H(t)\dot{\phi} + V'(\phi) = 0$. For $H(t) > m(\phi)$ the equations are those of an overdamped harmonic oscillator, and the field is constant for every potential value. When the temperature lowers and $H(t) \sim m(\phi)$ the field starts oscillating around the potential $V(\phi)$. In such eventuality the energy density stored in the oscillations can be used to describe the relic energy density of the particle.

WIMPs

The acronym WIMP stands for weakly interactive massive particle, and such particle can be an interesting candidate for cold dark matter. WIMPs are formulated with a *freeze-out* production mechanism. Interestingly, WIMP particles have a self-annihilation cross section which, for a mass of $\sim 100 \text{ GeV}/c^2 - \text{TeV}/c^2$ and calculated

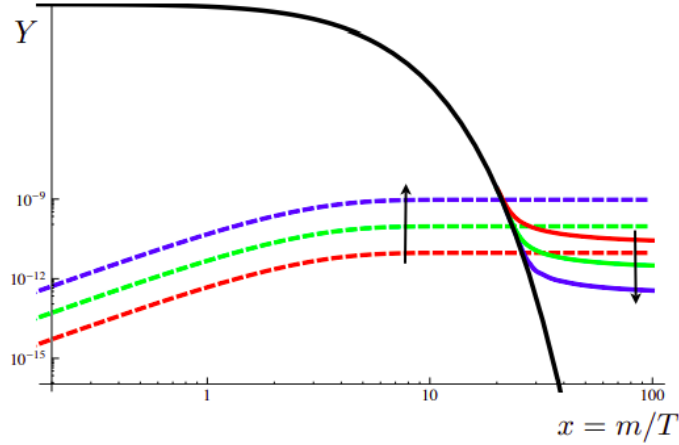


Figure 1.2: Scheme of the *freeze-out* and *freeze-in* mechanism. The x is the ratio between the dark matter candidate mass and the temperature T . Y is the comoving number defined as ρ per entropy density. The black continuous line is the comoving density for DM at thermal equilibrium with the bath. The continuous colored lines represent the progress in case of *freeze-out* scenario. Dashed lines show the comoving number for *freeze-in* case: initially Y is almost zero, while it grows in time. The arrows indicate the effect of increasing the couplings between the DM and the bath particles. Image taken from [20]

at the time of *freeze-out*, assumes value $\langle \sigma v \rangle \sim 10^{-26} \text{cm}^3 \text{s}^{-1}$. With this value, the calculated relic density turns out to be $\Omega_W h^2 \sim 0.1$ [22], very similar to the value $\Omega_{DM} h^2$ measured for DM [19]. For this reason WIMPs are good candidates. The interest towards these particles arises also for the fact that they are predicted in some extensions of the Standard Model, such as Minimal Supersymmetry [14]

QCD axions

QCD axions can be proposed as dark matter candidates. As a matter of fact, after the exclusion of a visible axion, as the one in the original PQWW model, most of the alternative models propose an invisible particle which is also dark matter candidate, making them even more important in the search for new physics. In these models the axion mass can be quite small. In order to be a *cold dark matter* candidate, it must have an adequate production mechanism. The *misalignment* mechanism produces light QCD axions with a relic abundance which can match the DM one, and, because of the mechanism itself, the axions are non-relativistic despite the light mass [23], [24].

I clarify from now that for the models studied in this thesis the two remain separate objects: the QCD axion studied is not a DM candidate, and the DM particles

considered do not solve the CP-parity problem in strong interactions

ALPs

The generalization of a scalar or pseudo-scalar field like the axion is called axion-like particle (ALP). They resemble the axion because of certain properties (electrically neutral and spin zero), and also appear in different theoretical context. They maintain couplings to fermions and photons, though not necessarily to gluons. They remain good for DM proposal. In chapter 4 a model viewing ALP as dark matter particles produced by *freeze-in* mechanism will be discussed.

2. ALP model and experimental search

The two problems above stated and explained can be solved by the formulation of at least one new field in the Standard Model picture. In particular, both the CP-problem and the dark matter explanation are related to the class of particles called axion-like particles. It is then interesting to study the phenomenological implications of a new scalar field introduced as an ALP.

2.1 Effective ALP model

Similarly to what was done by Peccei and Quinn, one can introduce in the SM lagrangian a new global symmetry broken at a given energy scale, and obtain a new degree of freedom as a pseudo-scalar field of which to study the couplings with the Standard Model fields.

This type of approach is used in this thesis, where I have studied the theoretical and phenomenological implications coming from the introduction of an effective lagrangian term capable of describing two classes of axion like particle (ALP) models.

From [25], the most general effective lagrangian up to five-dimension operators for a pseudoscalar field a can be written as:

$$\begin{aligned} \mathcal{L}_{eff} = & \frac{1}{2}(\partial_\mu a)^2 - \frac{m_{a,0}^2 a^2}{2} + \frac{\partial_\mu a}{2\Lambda} \sum_f \bar{\psi}_f \gamma^\mu c_f \psi_f + \\ & c_{GG} \frac{a}{\Lambda} G^{\mu\nu} \tilde{G}_{\mu\nu} + c_{BB} \frac{a}{\Lambda} B^{\mu\nu} \tilde{B}_{\mu\nu} + c_{WW} \frac{a}{\Lambda} W^{\mu\nu} \tilde{W}_{\mu\nu} \end{aligned} \quad (2.1)$$

with Λ energy scale suppressing the higher order operators and $m_{a,0}$ a possible mass term explicitly breaking the residual shift symmetry given by a $U(1)$ transformation. It is convenient to take \mathcal{L}_{eff} invariant under CP parity, thus the a field must be odd under CP.

The lagrangian in equation 2.1 is an effective lagrangian because it contains only operators up to dimension 5.

Again, it is convenient to work in a basis in which the fermion fields have been rotated by an axial transformation:

$$\psi \rightarrow e^{i\gamma_5 \frac{a}{2f_a} Q_a} \psi \quad (2.2)$$

where Q_a in a generic matrix acting on the fermions. Because of the rotation, in a complete lagrangian including also the fermion equations the kinetic term of fermions $\bar{\psi} i \partial_\mu \gamma^\mu \psi$ give rise to an other derivative coupling with the a field :

$$\mathcal{L}_{eff} = \frac{1}{2}(\partial_\mu a)^2 + \frac{\partial_\mu a}{2f_a} \sum_{i,j} \bar{\psi}_i (C_{ij}^V \gamma^\mu + C_{ij}^A \gamma^\mu \gamma^5) \psi_j + .. \quad (2.3)$$

where the index i, j run on all three family generations both for leptons and quarks. The coupling matrix C_{ij}^V enters the vector current, while C_{ij}^A for the axial one. Both the matrices can have on and off diagonal elements.

This effective lagrangian is interesting because it can be used to describe a:

- **QCD axion with non-universal flavor coupling:** the field a can be recognized as the Goldstone boson of the $U(1)_{PQ}$ and plays the role of the QCD axion. The axion model must necessarily include the $aG\tilde{G}$ as explained in the previous chapter. The energy scale Λ is then the f_a previously cited, and again the relation 1.42 connects the mass of the axion a and the f_a scale. The coupling matrix structure can be used to describe a peculiar model in which the QCD axion has a mass in the MeV/c^2 . This QCD axion model will be explained in chapter 3
- **Axion-like particle as dark matter candidate:** in this formulation, the field a is a generic ALP. It is not related to the solution of strong CP problem, so in this case the Λ is not correlated to the mass term. The ALP particle proposed with this lagrangian can be a dark matter candidate with tree-level flavor-violating couplings to leptons, which opens the possibility to link its production with lepton flavor violating processes. This model is described in chapter 4.

rivedi

The expression in equation 2.3 remains a generic expression for a new particle which interacts with the Standard Model fields. For every possible model formulation it is necessary to search for the signatures of such interactions. The way this can be done is through a variety of experiments, briefly explained in the next section.

2.2 Search and constraints for ALPs

The search for generic ALP can be implemented with different techniques, coming from various physics sectors. The following means are used to probe different possible ALP models which share the lagrangian in equation 2.1. They study ALPs coming from processes either generated in laboratory conditions or present in nature. For this the following experimental searches are divided as laboratory experiments and astrophysical observations. In particular the following options will concentrate on the coupling of ALPs with photons and electrons, which are the most interesting for many models.

At the end of the summary of the experimental techniques there are two plots, in figure 2.1 and 2.2, showing the main limits both for the ALP-photon coupling and ALP-electron coupling.

2.2.1 Laboratory experiments

These type of experiments search for ALPs generated by colliding particles. They suffer of less uncertainties because the laboratory conditions are well controlled and the physical processes are better understood. The experiments look at the decay products of the ALP. The ALP is invisible if its decay length ($l = \tau c \beta \gamma$) is larger than the detectable region, meaning it decays outside the experiment. In models with high suppression scale the couplings with SM particles are extremely suppressed, hence the particle has a long lifetime τ and is more likely to escape the detector before decaying (as the invisible axion previously mentioned).

Beam dump experiments

Beam dump experiments are a class of experiment in which an energetic beam collides against a target. From the interaction between the beam particles and the material nuclei, a final state including an ALP could arise, for example from a sort of bremsstrahlung. The produced particles flow towards an electromagnetic calorimeter, which is behind an earth shielding. The SM particles - except neutrinos - are stopped by the shielding, while new possible particles could pass the shielding and be detected through their decay products. This type of experiment can test the axion-photon coupling thanks to the Primakoff production and the axion-electron coupling thanks to Bremsstrahlung effect [26], [27].

Light shining through wall

This type of experiment (LSW) exploits the coupling between axion field and the electromagnetic tensor, coupling which allows the photon to convert into an axion and vice versa. The idea of the experiment is to direct a photon beam against an absorbing wall, after which no photons should be detected. Thanks to the presence of the magnetic field, a photon could convert into an axion. This particle, thanks to its suppressed interactions, could go through the wall and give signal once it converts again into a photon. This type of experiment is well illustrated in [28].

Colliders

This type of experiment class uses energetic beams colliding on each other surrounded by detecting material to detect the final state particles. From the interacting beam particles, an ALP can be generated and its decay products detected. Interesting channels such as $e^+e^- \rightarrow a\gamma$ or decays of resonances such as $\Upsilon \rightarrow a\gamma$ are studied at LHC, LEP, CLEO and BaBar [29]. The experiment ARGUS, at the e^+e^- collider ring at DESY, has carried on a study on the lepton-flavor violating processes which could be mediated by an ALP. The collaboration has set limits on the branching ratio of $\tau \rightarrow ea$

and $\mu \rightarrow ea$, which can be recast in a specific ALP model as limits on the coupling parameter between the ALP and the interested leptons.

Target experiments

Similarly to the beam dump experiments, these experiments direct an energetic beam against a target. In particular, the experiments here cited use beams of muons, and the collision on the target is used to stop the muon and study its decay at rest. The muon in fact has a long lifetime ($\tau_\mu = 2.2 \mu\text{s}$), which in other experiments results in a long decay length, meaning that it can decay outside the detective material.

For high precision muon decay measurements specific experiments have been designed. It is the case of TRIUMF, Mu3e, MEGII. They study processes which contain lepton flavor violation, which again can be explained in different ALPs models depending on the characteristics of the new particle involved. The limits on the $\mu \rightarrow e\alpha$ branching ratio given by the work of Jodidio at the TRIUMF collaboration is still one of the most stringent [30]. The experiment Mu3e [31] studies channels like $\mu \rightarrow eee$, $\mu \rightarrow e + X$ with X short or long lived particle. The collaboration aims at lowering the existing limit on the $\mu \rightarrow eee$ from 10^{-12} given from SINDRUM [32] collaboration to 10^{-16} .

The same final state of $\mu \rightarrow \text{invisible} + e$ could be implemented at the MEGII collaboration [33] where there are ongoing researches for $\mu \rightarrow \gamma + e$. For both experiments the expected bounds on the lepton-flavor violating coupling of μ and e should be stronger than the present ones.

2.2.2 Astrophysics and cosmology

A great deal of constraints on ALP models come from cosmology and astrophysical observations. This physic sector represents a good environment in which to seek presence of ALPs, because stars are powerful sources of weakly interacting particles (such as neutrinos, or new particles as ALPs or others).

Star cooling

One of the main ways to prove the production of ALPs in stars is to measure how this new energy loss mechanism could alter the stellar evolution. An example is given by the observation of the neutrino burst from Supernova SN1987a [34], which should be shorter if ALP emission were possible. Also, the processes of energy loss of red giants [35] and the cooling rate of the Sun and white dwarfs put limits in the ALP-photon parameter space.

Direct detection

Direct detection seeks the interaction between an ALP and the material of a detector through the recoil of electrons in the material. For example, an incoming ALP could undergo axion-electric effect in which the ALP is absorbed as in $ae^-Z \rightarrow e^-Z$. This would lead to a recoiling electron with same energy as the incoming ALP. This type of search is carried on by the Edelweiss collaboration [36], which concentrates on the study of Solar axions.

Bragg diffraction

An other technique to study solar axions is the one used by DAMA experiment [37]. The experiment is based on the conversion of an ALP into a photon due to the electric field of a crystal configuration. The photon then scatters through the crystal, and if it satisfies the Bragg condition the signal is enhanced. This mechanism depends on the direction of the incoming axion respect the crystal plane, so the dependence of the signal on the sun position is used to suppress the background. Also the Edelweiss experiment is suitable for this type of search.

Helioscope technique

Helioscopes are superconducting magnets kept at extreme low temperatures. They are used to detect photons coming from the inverse Primakoff effect of solar axions, which is possible thanks to the magnetic field of the apparatus. An example is given by the Cern Axion Solar Telescope (CAST) [38].

Telescope search

A particular class of axions, with mass in the eV/c^2 range, should be abundant in galaxy clusters and have a signature decay into two photons with wavelength $\lambda = 310 \div 830 \text{ nm}$. Different telescopes have searched for this type of signature [39], and the lack of signal puts a limit on the $3 - 8 eV/c^2$ axions.

The discussed experiments and searches limit the viability for an ALP model both in the case of a QCD axion and of a candidate for dark matter. The next two chapters will describe phenomenological models which could exist in the present limitations.

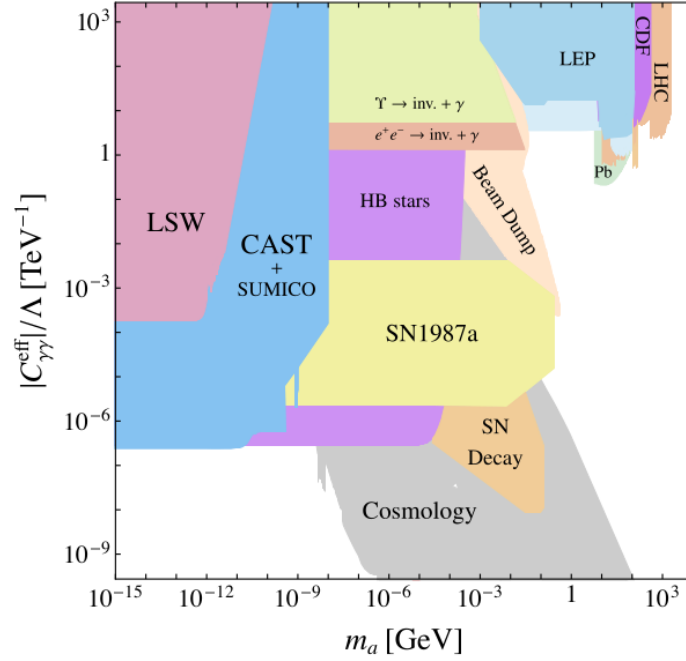


Figure 2.1: The figure reports the limits on the ALP- γ coupling $C_{\gamma\gamma}^{eff}$ obtained by different techniques for a model where the ALP decays mainly into two photons. The plot is an exclusion plot, for which the colored regions are the ones excluded. The exclusion areas show the name either of the experiment (CAST, LEP, LHC), of the source of constraint (Cosmology, HB stars, SN decay), of the class of experiments (LSW) or of the specific channel observed in a collider experiment ($\Upsilon \rightarrow inv. + \gamma$, $e^+e^- \rightarrow inv. + \gamma$). From the plot it is evident that the $C_{\gamma\gamma}^{eff}$ coupling is fairly constrained, making it a crucial parameter to formulate in any ALP model not excluded. Image taken from [40]

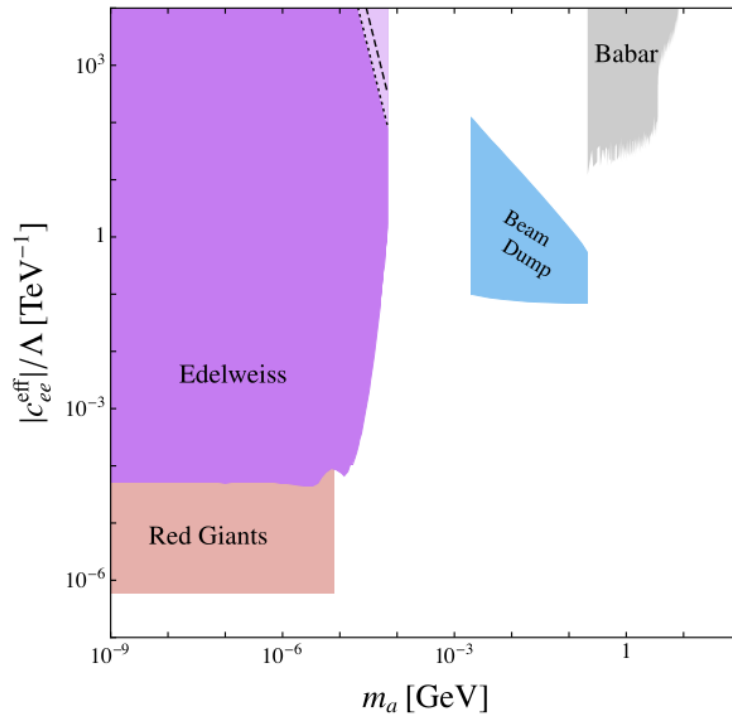


Figure 2.2: Exclusion plot for the ALP- e coupling c_{ee}^{eff} in a model where the ALP decays predominantly into an electron-positron pair. The limits come from different experiments (Edelweiss, Babar, Beam Dump experiments) and in general from the observations of red giants. This parameter space results less constrained. Image taken from [40].

3. QCD axion in the MeV range

This chapter presents one of the possible formulations for the generic ALP lagrangian written in equation 2.3.

In the case here considered, the lagrangian can be used in a model for a QCD axion with a mass in the MeV/c² range. A viable axion model is surely interesting to confirm the PQWW general mechanism proposed as solution of strong CP problem stated in chapter 1. Here the lagrangian is reported, and also the main characteristics of the QCD axion:

$$\mathcal{L}_{eff} = \frac{1}{2}(\partial_\mu a)^2 + \frac{\partial_\mu a}{2f_a} \sum_{i,j} \bar{\psi}_i (C_{ij}^V \gamma^\mu + C_{ij}^A \gamma^\mu \gamma^5) \psi_j + \frac{1}{4} g_{a\gamma\gamma} F \tilde{F} \quad (3.1)$$

For consistency, because it shall now describe an axion, the scale Λ will again be referred to as f_a . The lagrangian is written after the field rotation in equation 2.2 to eliminate the θ term. The rotation modifies the axion-photon coupling $g_{a\gamma\gamma}$ and it shifts the dependence of the axion in the mass matrix for fermions. By mapping the lagrangian with a chiral one the mass term for the QCD axion arise as:

$$m_a \sim 5.7 \frac{10^{12} \text{GeV}}{f_a} \mu\text{eV} \quad (3.2)$$

An axion with mass in the MeV/c² range thus implies a breaking energy scale $f_a \sim \text{GeV}$. New physics at the GeV scale has important features. From a theoretical point of view, the model of such axion is not affected by the *PQ quality problem*, which is explained in [10] and here briefly reported.

Global symmetries, as the $U(1)_{PQ}$, are considered no to be fundamental in quantum field theory. When a set of renormalizable operators allowed by Lorentz invariance has a remaining symmetry over a global redefinition of the fields, the symmetry is said to be *accidental*. Such symmetry is expected to manifest below a certain energy scale, over which higher non renormalizable operators would break it. The minimum dimension d suitable for the non-renormalizable operators has to be kept in account, because the higher it is, the better the *accidental* symmetry shall be.

In the Peccei-Quinn model, there are two scenarios :

- **high f_a value:** if the breaking energy scale assumes values $f_a \geq 10^8 \text{GeV}$, the lowest dimension required for a non-renormalizable and PQ violating operator is very large : $d \geq 8$. This because the operators modify the axion potential, making it move from the minimum and thus spoiling the whole PQ mechanism. The dimension value d is then found by imposing $\theta_{eff} = 0$ so to save the mechanism, and it depends on the value chosen for f_a . For high breaking energy scales ($f_a = 10^8, 10^{10}, 10^{15} \text{GeV}$) the dimension of the operators grows ($d = 8, 10, 21$)

meaning that the $U(1)_{PQ}$ is a very good symmetry. But it is a global symmetry, expected to be broken. It is clear that this feature will come at cost of some fine tuning of parameters.

- **low f_a value:** if the scale is low like $f_a \leq 10^3 \text{ GeV}$ the minimal dimension for operators breaking the PQ symmetry but not spoiling the mechanism is $d > 5$. For example, in the original PQWW model the lowest-dimensional symmetry breaking operator can be written with the Higgs singlets and has a dimension of 6, so the quality of the Peccei-Quinn symmetry should not be so high.

From an experimental point of view, new physics at this energy scale is surely more easy to be tested in the available experiments, but of course encounters much more limits. In fact, the PQWW at the EW scale has been ruled out.

The model uses an axion with non universal couplings with fermion fields, which means that the C_{ij} matrices can have off-diagonal elements. This structure allows to evade some stringent limits, as explained in the next section. The possibility of a non universal structure arises from a UV completion theory of the class of the *DFSZ* models. This class usually adds two or more Higgs doublets carrying PQ charges to the Standard Model and at least one SM-singlet complex scalar field ϕ . This allows to decouple the EW symmetry breaking scale and the PQ scale [41]. Also, the SM fermion fields, through the interaction with the two Higgs doublets, become charged under the symmetry $U(1)_{PQ}$. By non requiring such charges to be universal, it is possible to achieve the desired coupling matrix C_{ij} . An example of a general axion-fermion coupling in the *DFSZ* picture is given in the paper [10].

The paper [42] follows a phenomenological type of study: it investigates the necessary couplings considering a scale $f_a \sim \text{GeV}$ on the basis of precedent studies.

For this model, a region in the space parameter given by the axions mass and its coupling to electrons is still not completely excluded. The model is thus still viable, even though it will have some parameters explicitly tuned so to avoid the up mentioned limits.

3.1 Phenomenological aspects

Some existing bounds are used to select the right form of the coupling between the axion and SM particles, as in the case of quarkonia decays and the mixing between axion and pions, both of them briefly explained. Thanks to an accurate choice of couplings, the model remains viable. Other precedent bounds are instead deemed as uncertain and not able to eliminate all possible space parameter. This is the case of Kaons decay.

Quarkonia decay

Decays of quarkonia such as :

$$J/\Psi \rightarrow \gamma a \quad \text{or} \quad \Upsilon \rightarrow \gamma a \quad (3.3)$$

are to be evaded, otherwise they would be dominant respect to the decay in leptons states. The couplings λ_c and λ_b respectively between axion and quark c and b are of order $O(m_q/f_a)$. Taking in account $f_a \sim \text{GeV}$ and the quarks masses as in [1] the couplings would be of order one, thus dominant. But radiative decays of quarkonia did not lead to axion discovery [43]. In the paper, the constraint is evaded by allowing couplings only between axions and the first quark generation.

Pion-phobia

The effective lagrangian 2.3 written in the convenient basis of rotated fields has a mass term M_a for fermions which depend on the axion field and on the charges Q_i of the quarks under the global symmetry $U(1)_{PQ}$. Considering only the quarks u, d the mass is:

$$M_q(a) = \begin{pmatrix} m_u e^{iQ_u a/f_a} & \\ & m_d e^{iQ_d a/f_a} \end{pmatrix} \quad (3.4)$$

Diagonalizing the matrix, a mixing angle $\theta_{a\pi}$ between the axion and the pion arises, and it is proportional to :

$$\theta_{a\pi} \propto \left(\frac{Q_u m_u - Q_d m_d}{m_u + m_d} \right) \frac{f_\pi}{f_a} \quad (3.5)$$

In the MeV/c^2 range, the $a - \pi$ mixing would bring rare decays such as $\pi^+ \rightarrow e^+ \nu_e a \rightarrow e^+ \nu_e e^+ e^-$, with decay rate:

$$\Gamma(\pi^+ \rightarrow e^+ \nu_e a) = \frac{\cos^2 \theta_c}{384\pi^3} G_F^2 m_\pi^5 \theta_{a\pi}^2 \quad (3.6)$$

The SINDRUM collaboration [44] has put an upper limit on the branching fraction of this specific π decay, for an axion with mass $m_a \sim 1 - 20 \text{ MeV}/c^2$. The upper bound is then translated to the mixing angle value: $|\theta_{a\pi}| < (0.5 - 0.7) \cdot 10^{-4}$.

As seen in equation 3.5, the value of $\theta_{a\pi}$ depends on the masses of the up and down quarks and their charge Q_u and Q_d . The latter can be conveniently chosen so to set to zero the $\theta_{a\pi}$ while remaining of order $O(1)$. This is achieved by setting :

$$\frac{Q_u}{Q_d} = \frac{m_d}{m_u} \quad (3.7)$$

Such a choice allows the model to be *pion-phobic* but still viable. The choice in equation 3.7 is possible in this model in which C_{ij} allows non-universal couplings.

Since the axion does not mix with neutral pions, it is also possible to avoid an axion decay into two photons. This would contribute to the effective coupling between $a - \gamma$ which is highly constrained as seen in the previous chapter and in the related plot 2.2.

K decays

K decays have been used as experimental proof to rule out axions in the MeV/c^2 range. In the article [42] the authors review the papers and find the constraints to be quite feeble. The critiques concern mainly three types of arguments of the charged kaons decay. Firstly the experimental analyses and interpretation of some papers on $K^+ \rightarrow \pi^+ a$ are deemed as not clear, so the limits for $m_a < 50 \text{MeV}/c^2$ are ignored. Secondly there are problems with relating $K^+ \rightarrow \pi^+ a$ to SM decays of kaons because of the way the *octet-enhancement* is realized in the chiral perturbation theory. Lastly, it is impossible to calculate a reliable estimation of the $\theta_{a\eta}$ mixing. Therefore, the value of such angle can not be used to test bounds from $K^+ \rightarrow \pi^+ a$. The decays by themselves can not be used to definitively exclude the QCD axion of this model.

Axion-photon coupling

The coupling between the axion and the electromagnetic tensor is model dependent:

$$g_{a\gamma\gamma}^0 = \frac{\alpha}{2\pi f_a} \frac{E}{N} \quad (3.8)$$

where α is the electromagnetic constant, and E and N respectively the electromagnetic and color anomaly of the $U(1)_{PQ}$ symmetry. After the rotation of the fields (equation 2.2) the anomaly of the lagrangian modifies the coupling as :

$$g_{a\gamma\gamma} = \frac{\alpha}{2\pi f_a} \left(\frac{E}{N} - 6\text{Tr}[Q_a Q^2] \right) \quad (3.9)$$

where Q is the diagonal matrix containing the electric charges of the quarks.

In the paper [42] the calculations of this effective operator are computed in the chiral lagrangian. The effective coupling depends on the mixing angles between the axion and mesons, and it is of order $g_{a\gamma\gamma} \sim 0.1/(10 \text{TeV})$. This value can be confronted in with the limits in figure 2.2. The shown limits are for models in which $Br(a \rightarrow \gamma\gamma) \sim 1$ and the scale is of order TeV. The axion is, for many limits cited, an invisible, meaning that its decay length is greater than the detectable region. In the model here discussed, the axion is not invisible in that sense, because its scale is $f_a \sim \text{GeV}$ and it promptly decays into e^+e^- . This means that in the figure some of the excluded regions do not exist for this model. In particular the limits of $Y \rightarrow \gamma + inv.$ and $e^+e^- \rightarrow \gamma + inv.$ put by LEP. The model is therefore not excluded.

3.1.1 Axion-Electron coupling

The axion couples with the fermions in a derivative way. Because of this, it does not play any role in the solution of the strong CP problem. Furthermore it is model independent, so the possible constraints on the coupling could be enough to rule out the axion proposed by themselves.

In the paper [42] the axion-electron coupling is studied in the non-derivative form, which can be obtained by an integration by parts of the lagrangian term. The interaction term is then:

$$\mathcal{L} \supset \frac{Q_e}{f_a} m_e a \bar{e} i \gamma_5 e \quad (3.10)$$

The ratio between the electron charge Q_e under $U(1)_{PQ}$ and the scale f_a is the coupling constant, and will be object of study in chapter 6. In order for the model to be experimentally viable, the axion should couple predominantly to electrons, so to avoid constraints from the axions invisible decay mode as in $K^+ \rightarrow \pi^+ (a \rightarrow \text{invisible})$.

Other limitations on the coupling are given by beam dump experiments and recast from the search of *dark photons*. The axion enters also in the electrons and muons anomalous magnetic moment, and this also will have consequences on the coupling strengths

Beam dump experiments

Beam dumps experiments have been introduced in chapter 2 as an important class of experiments limiting the space parameter for generic ALP particles. For the axion here proposed, the branching fraction of axion into electro-positron pair is considered almost one. With such assumption, the lifetime of the axion can be inferred by the $a \rightarrow e^+ e^-$ decay width [42]. The formula for the decay width is:

$$\Gamma_{a \rightarrow e^+ e^-} = \frac{m_a}{8\pi} \left(\frac{Q_e m_e}{f_a} \right)^2 \sqrt{1 - \frac{4m_e^2}{m_a^2}} \quad (3.11)$$

and the lifetime is $\tau = h/(2\pi\Gamma)$. In figure 3.1 are shown the constraints from beam dumps experiments are shown as a gray exclusion area. The plot shows that the lifetime for a viable axion in the MeV/c² range must be less than $\tau \leq \text{ps}$ [27]

Search from dark photon

One possible extension of the Standard Model comes from the formulation of a $U(1)_{DM}$ abelian gauge group, from which a new massive vector boson could arise as mediator between DM particles charged under the $U(1)_{DM}$ group and SM particles. The boson is called dark photon, and shares a lot of theoretical and experimental aspects with the massive axion.

The most important aspect is that both particles interact with electrons : the dark-photon with a coupling ε , the axion with coupling Q_e/f_a . The two particles can also share the same final state. It is then possible to recast the limits on ε coming from other experiments to limits on the parameter of our interest. In figure 3.1 such recast is shown both for KLOE and BaBar. The two experiments and their study on the dark photon are briefly explained at the end of chapter 6.

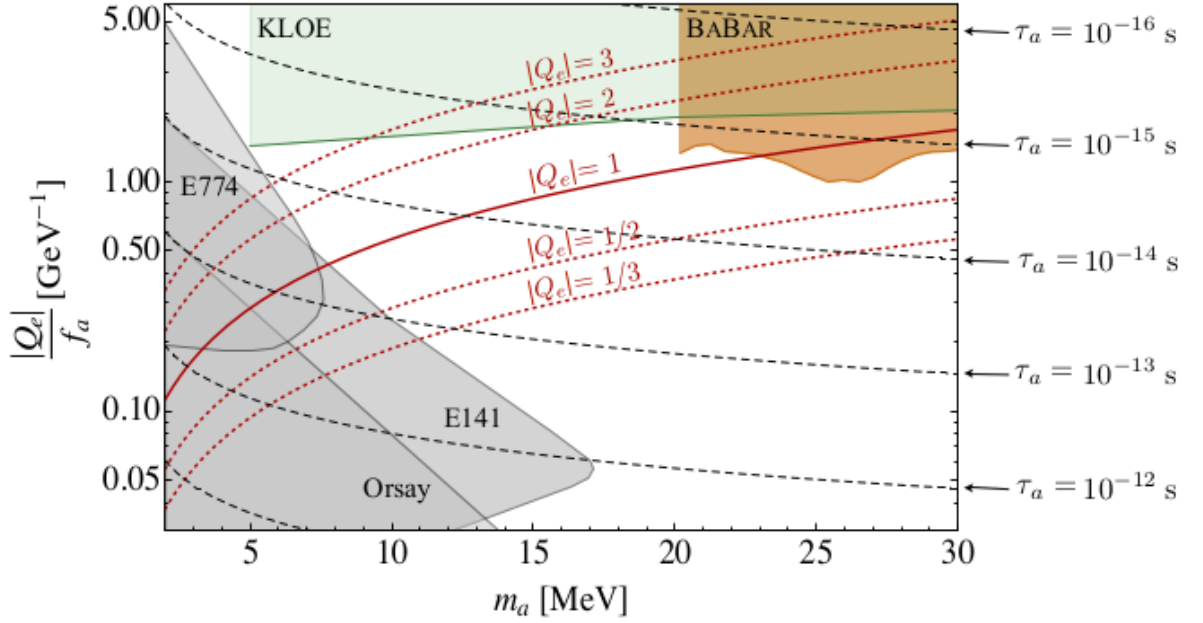


Figure 3.1: The plot shows the parameter space given from the axion mass m_a and electron-axion coupling Q_e/f_a . The red and black lines are parameters of the model: the red lines represent various options for the electron charge Q_e under the new symmetry $U(1)$, while the black dotted lines show the lifetime τ_a . They are plotted to locate the possible values entering the still allowed region. The gray regions are the ones excluded by beam dump experiments. The KLOE and BaBar exclusion regions are a forecast from their search of a dark photon. Image taken from [42]

Leptons anomalous magnetic moment

The electrons anomalous magnetic moment (AMM) can be calculated in the SM and compared with its measure. Up to date, the two differ as:

$$a_e^{SM} - a_e^{exp} = -0.9 \cdot 10^{-12} \quad (3.12)$$

where $a = (g - 2)_e/2$ and the sup scripts SM and exp indicate respectively the calculated and measured value ([45] and [46]).

The MeV axion, through its coupling with electrons, contributes to the AMM, and the one loop level is the largest contribution. If the electron charge under the new symmetry is $|Q_e| \geq 0.5$, the axions contribution exceeds the difference in equation 3.12 by more than two sigma. The problem can be avoided if the coupling between axion and heavier leptons are included, as explained in [47] and considering second order contributions. These are greater because proportional to m_l^2 (l is either a muon or tau). Taking in account the second loop contribution given from $a - \tau$, a fine tuning of the coupling parameter can regulate the total contribution as to be suitable for

the difference in 3.12. This is then a possible way to cancel the troublesome axions contribution. By adding also the coupling between axion and muons, one can keep in account the difference as in equation 3.12 both for electrons and muons. This is possible in a model contemplating non-universal couplings between the axion and leptons: as discussed in [47] the axion-electron and axion-muon matrix elements should follow the hierarchy $c_{ae} \sim c_{a\tau}$ and $c_{ae} \gg c_{a\mu}$.

3.1.2 Channels to explore

The coupling between the electron and axion is the main one to study, because in the model discussed it rules the axion lifetime and thus the viability of the whole axion model. Collider experiments represent a good tool to probe the model, especially for the energies scales involved. A useful channel can be represented by $e^+e^- \rightarrow \gamma a$, for example in a collider such as Belle II. The simulation for this channel will be object of chapter 6.

4. Axion Like Particle as Dark matter

The other possible formulation for a generic ALP with lagrangian as in equation 2.3 can be used in a model for which the ALP is a dark matter particle candidate. In a particular formulation described in the paper [48], the structure of the coupling matrix between the ALP and SM fermions is used to link the ALP production with lepton-flavor violating (LFV) decays of SM fermions.

New physics is often related to lepton flavor violating processes, because these are not expected in the Standard Model. The ALP, being a new particle enlarging the SM picture, is often related to LFV processes thanks to its coupling with leptons. This also has an experimental advantage because of the uniqueness of the process signature.

In this model, the main production mechanism of this dark matter particle is the *freeze-in* mechanism of LFV decays of standard model leptons.

4.1 Model description

The effective lagrangian is reported again:

$$\mathcal{L}_{eff}^{ALP} = \frac{1}{2}(\partial_\mu a)^2 + \frac{\partial_\mu a}{2\Lambda} \sum_{i,j} \bar{\psi}_i \gamma^\mu (C_{ij}^V + C_{ij}^A \gamma_5) \psi_j \quad (4.1)$$

In this scenario, the ALP mass and Λ are not inversely proportional as in the axion case. The lagrangian is effective and written under the EW scale, after the rotation of the fields with 2.2. It is also anomaly free meaning it does not include the tree level coupling with the electromagnetic field tensor $g_{a\gamma\gamma} F \tilde{F}$. The coupling between the ALP and photons generates from fermion loops, as later shown.

The study concentrates on the interaction with leptons, which are charged under the global $U(1)$, and it limits to the couplings of only right handed leptons. The charge matrix is indicated with P . The coupling matrices C_{ij} are responsible of lepton flavour violating interactions if they include off-diagonal elements. These can originate from the charge matrix P once the lepton fields are rotated by the W, U matrix which diagonalize the fermions mass matrix:

$$U^\dagger M W = M^{diag} \quad (4.2)$$

Rotating from the chiral basis to the mass basis, the coupling matrices become:

$$C_{ij}^{V,A} = U^\dagger P_{ij} U \quad (4.3)$$

and in general can have off-diagonal elements.

To give a simple example for how the model works, one can work out the equations in a basis in which only two out of three leptons are charged. The choice of which ones are charged do not alter the conclusions, although it obviously changes the phenomenological aspect.

For this, one possibility is to choose the charge matrix P as:

$$P = \begin{pmatrix} 1 & 0 & 0 \\ 0 & -1 & 0 \\ 0 & 0 & 0 \end{pmatrix} \quad (4.4)$$

in which the electron and muon are charged under the $U(1)_{PQ}$. Again the charge matrix is flavor dependent.

The rotation matrix can be structured to implement the rotation only in the two charged lepton space, with the form:

$$U = \begin{pmatrix} \cos \alpha & \sin \alpha & 0 \\ -\sin \alpha & \cos \alpha & 0 \\ 0 & 0 & 1 \end{pmatrix} \quad (4.5)$$

The resulting coupling matrices are given by:

$$C^V = C^A = \begin{pmatrix} \cos(2\alpha) & \sin(2\alpha) & 0 \\ \sin(2\alpha) & -\cos(2\alpha) & 0 \\ 0 & 0 & 0 \end{pmatrix} \quad (4.6)$$

which have on and off-diagonal elements. The angular parameter α can be chosen so to give a predominant off-diagonal coupling. In fact if $\alpha = \pi/4 - \varepsilon/4$ the $C^{V/A}$ structure becomes:

$$C^V = C^A = \begin{pmatrix} \sin(\varepsilon) & \cos(\varepsilon) & 0 \\ \cos(\varepsilon) & -\sin(\varepsilon) & 0 \\ 0 & 0 & 0 \end{pmatrix} \quad (4.7)$$

and with the choice of a small enough ε the off-diagonal elements are predominant, so the texture in 4.7 enhances the lepton flavor violating processes, while reducing the flavor conserving ones. The interesting values are for $\varepsilon \ll 1$.

Rates

The model works with only two leptons charged under $U(1)$. For notation they will be named f_1 and f_2 , where for the rest of the discussion f_1 will be lighter than f_2 .

To link the production of the ALPs to the lepton flavor violating decays, a trivial limit on the ALP mass is that $m_a < m_{f_2}$. The rate for the kinematically allowed decay process is:

$$\Gamma_{f_2 \rightarrow a f_1} = \cos^2 \varepsilon \cdot \frac{1}{32\pi} \frac{m_{f_2}^3}{\Lambda^2} \left(1 - \frac{m_a^2}{m_{f_2}^2}\right)^2 \quad (4.8)$$

If the ALP were heavier than f_1 , the other allowed process would be $a \rightarrow f_1 f_1$, with a rate given by:

$$\Gamma_{a \rightarrow f_1 f_1} = \sin^2 \varepsilon \cdot \frac{m_a m_{f_1}^2}{8\pi \Lambda^2} \sqrt{1 - \frac{4m_{f_1}^2}{m_a^2}} \quad (4.9)$$

Thanks to the structure of 4.7, this decay rate is suppressed by the presence of $\sin^2 \varepsilon$.

The suppression present in the diagonal elements is important also for the decay of the ALP into two photons. In an anomaly free model as this one, the $g_{a\gamma\gamma}$ coupling has contributions coming from lepton loops, so the decay rate is:

$$\Gamma(a \rightarrow \gamma\gamma) \sim \frac{\alpha^2}{64\pi^3} \frac{m_a^3}{\Lambda^2} \sum_i |C_{ii}^A \frac{m_a^2}{12m_i^2}|^2 \quad (4.10)$$

where the index i runs over the three fermion families. In the model, the decay is suppressed because it relies on the on-diagonal elements of the coupling matrix. This feature is desirable: if the main decay of the ALP is in the two photon channel, the particles mean life time is inversely proportional to the decay width $\tau_a \propto 1/\Gamma(a \rightarrow \gamma\gamma)$ meaning that the more suppressed the decay width the more stable the ALP can be.

The limits on the lifetime τ_a come from precise measurements of the cosmic microwave background anisotropies [18]. The decay or annihilation of DM particles during the last scattering epoch would lead to early energy injection; the particles injected would have then heated and ionize the neutral hydrogen, modifying the CMB anisotropy spectrum. The lower limit on the ALP lifetime is $\tau_a > 10^{24}$ s for an ALP mass in the keV/c² – MeV/c² range, interesting for this model.

4.1.1 Production mechanism

Three main production mechanism for dark matter particles were illustrated in chapter 1. The one used in this model is the *freeze-in* mechanism : it assumes an almost zero initial abundance for the ALP, which couple to bath particles, without ever reaching equilibrium with them. These couplings allow the bath particles to create the wanted ALP, whose number density increase until the generating particles exit the thermal equilibrium. The number density is then froze in [20], [49].

The equations regulating the progress of the particle density and energy density n and ρ are the Boltzmann equations. They can be formulated for the PSD in and FRW universe as in [49]:

$$\frac{df(p)}{dt} = \frac{C[f(p)]}{E} \quad (4.11)$$

with $E^2 = m^2 + p^2$ and $C[f(p)]$ named collision operator which keeps account of all the processes involving the specific particle.

With the assumptions made for the *freeze-in* mechanism, in the expression 4.11 the only process to keep in account are the decay of particles giving the final wanted particle. Given an initial state of $B_i(k_i)$ bath particles with $i = 1..l$ and a final state with $B_{l+1}(k_{l+1}) + .. + B_{l+m}(k_{l+m})$ bath particles and $\chi(p) + .. + \chi(p_n)$ DM particles, the $C(T, p)$ function for only DM production results in [49]:

$$C(T, p) = \frac{n}{2} \int \prod_{i=1}^{l+m} d^3 k_i \prod_{i=2}^n d^3 p_i (2\pi)^4 \delta^4(P_f - P_i) |\mathcal{M}|^2 \prod_{i=1}^l f_i(k_i) \quad (4.12)$$

For the model, the ALP can be produced by:

- lepton flavor violating decay $f_2 \rightarrow f_1 a$.
- scattering on-diagonal $f_i \gamma \rightarrow a f_i$ and $f_i f_i \rightarrow \gamma a$.
- off-diagonal $f_2 \gamma \rightarrow a f_1$ and $f_2 f_1 \rightarrow \gamma a$.

The significant contribution to the Ω is given by the decay rate $f_2 \rightarrow a f_1$. In fact the scattering processes including photons always include a α_{EM} factor which suppress the contribution.

The result for the relic density in the freeze in mechanism is given by:

$$\Omega h^2 \approx \frac{3.46 \cdot 10^{26} g_{f_2} m_a \Gamma(f_2 \rightarrow f_1 a)}{g_{*s} \sqrt{g_*} m_{f_2}^2} \quad (4.13)$$

with g_{f_2}, g_*, g_{*s} are the relativistic degrees of freedom for the f_2 lepton and the energy and entropy density at the freeze in time, which occurs at $T \sim m_{f_2}$. The dependence of g_* and g_{*s} from the temperature can be found in [50].

The relic abundance for dark matter measured from the Planck collaboration is $\Omega_{DM} h^2 = 0.12$. By matching the abundance in 4.13 with the measured one, requiring thus that the model describes an ALP which covers all the abundance, the expected energy scale for the model is given by:

$$\Lambda \approx \sqrt{\frac{g_{f_2}}{g_{*s} \sqrt{g_*}}} \sqrt{\frac{3.46 \cdot 10^{26}}{0.12}} \sqrt{\frac{m_a m_{f_2}}{32\pi}} \cos \epsilon \quad (4.14)$$

having ignored orders of $m_a^2/m_{f_2}^2$. The mass value has the upper limit given from the heaviest lepton mass, but it also has a lower limit. The ALP produced from the *freeze-in* mechanism is a warm dark matter candidate if its initial kinetic energy is too high. A higher initial velocity for the particle means a grater free-streaming length, the parameter measuring the distance the particle travels before interacting with other particles. Dark matter is used to justify the structure formation, as said in chapter 1. Having a particle candidate with a high free-streaming length is problematic, because it would erase the cosmological perturbations, thus spoiling the explanation for structure formation. A limit on the lower value of m_a is given by [49] and for the *freeze-in* mechanism is of order $m_a \geq 10 \text{ keV}$.

Considering an ALP with mass in the range $10^{-2} - 10^{-1} \text{MeV}/c^2$ the ϵ parameter which gives an adequate lifetime τ_a and a value of Λ in an open region in the parameter space is $\epsilon \sim 10^{-2}$ as shown in figure 4.1 taken from [48]. The magnitude of the breaking energy scale is $\Lambda \sim 10^9 \text{GeV}$ for the model to be still viable and to describe an ALP which covers all Ω_{DM} .

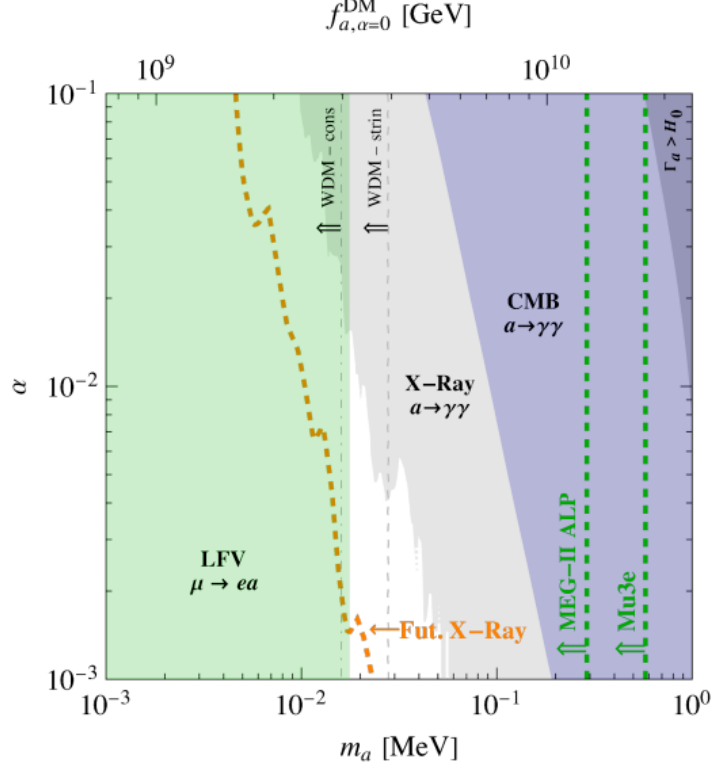


Figure 4.1: Parameter space given from the ALP mass m_a , the value of the ϵ parameter (in figure α) and the energy scale Λ (in the figure f_a). The exclusion plot shows the limits and the free region available for this model in the case of μ and e charged leptons, for an ALP production given by $\mu \rightarrow ea$. The green excluded area is derived from the search of $\mu \rightarrow ea$ conducted by [30]. The area in dark blue is excluded by studies of the CMB in the eventuality of energy injection from ALP decay. The gray excluded area refers to search of dark matter particles into two mono-energetic photons with energies in the $1 \div 100 \text{keV}$ range [51]. The plot shows possible future limits coming from the MEGII and Mu3e experiments with the dashed lines.

4.2 Channels to explore

The model described can be probed in experiments which study LFV decays such as $\tau \rightarrow \mu(e)a$ or $\mu \rightarrow ea$. The final state is a lepton track and missing energy due to the invisible ALP, since the latter does not decay. The possibility to have DM

detection in terrestrial experiments is very important, since other constraints come from cosmological observations (such as the CMB) which can be affected both from theoretical or experimental inaccuracies.

The figure 4 of paper [52] shows the comparison between CMB bounds on DM and detector bounds. For the τ channels, cosmological observations are still stronger, but for the μ channel the detector bounds are more stringent. The new experiments MEGII and Mu3e may be able to probe scales of order $\Lambda \sim 10^9 \text{GeV}$, as suggested in figure 4.1. In chapter 7 there is an overview on the channel $\tau \rightarrow la$ carried on by Belle II.

5. Belle II

Searches for new physics using accelerators has a number of benefits, such as a better understanding of the physical process both of signal and background, and the control over the number of events through the luminosity of the machine. Searches for new physics at colliders can be pursued by two means. One is to use detectors capable of probing SM at higher energies, the approach of experiments at the LHC. In this approach the main goal is to obtain the largest number of final states using highly energetic beams (TeV), with a side effect of a large hadronic background. From this type of experiment, the particles potentially discovered represent new heavier degrees of freedom enlarging the standard model.

Another possibility is to use colliders with lower energy, but high intensity beams, usually fixed at the mass value of a resonance. The final states include only those matching the initial state resonance, but can be studied in a cleaner environment and allow more precise measurements. This second approach is more useful in the precision test of the Standard Model, and aims at finding new physics which could cause discrepancies between a predicted quantity and its measurement. For this type of colliders, the main feature is the luminosity of the machine and the angular coverage of the detector elements.

For the models presented in chapter 3 and chapter 4, given the mass range of the particles and the strength of the interactions, the best choice is to study the phenomenology in precision-high intensity colliders.

In this chapter I introduce a class of colliders known as *B-factories* and concentrate on the Belle II experiment, for which I have studied two interesting channels.

5.1 B-factories

The term *B-factory* indicates an electron-positron collider with a high production rate of B mesons. These type of colliders have been introduced to produce big samples of B mesons for studies of CP violation in weak interactions in the B sector.

CP violation can be measured in weak interactions through the decay of meson systems such as $K\bar{K}$ or $B\bar{B}$ in three ways [53]:

- from mixing violation: when the mixing between two neutral mesons, due to weak interactions, has a different amplitude $M^0 \rightarrow \bar{M}^0 \neq \bar{M}^0 \rightarrow M^0$.
- direct violation in the decay: when the decay of a neutral meson in a final state $|f\rangle$ differs from the antiparticle decay $M \rightarrow |f\rangle \neq \bar{M} \rightarrow |\bar{f}\rangle$.

- violation in the interference between mixing and decay amplitudes: given a final state $|f\rangle$ eigenvalue of CP, accessible both from M and \bar{M} , violation can be found by the interference between $M^0 \rightarrow |f\rangle$ and $M^0 \rightarrow \bar{M}^0 \rightarrow |f\rangle$

In *b-factories*, the production of B mesons is achieved by setting the collision energy at the $\Upsilon(4S)$ resonance, the first $b\bar{b}$ bound state which mass value allows a decay into b-flavored mesons. From the PDG [1], the mass values are $m_{\Upsilon(4S)} = 10.58 \text{ GeV}/c^2$ while $m_B = 5.28 \text{ GeV}/c^2$ and the decay has a branching fraction of $\Upsilon(4S) \rightarrow B\bar{B}$ given by $BF = 96\%$ where the final state can be B^+B^- or a $B^0\bar{B}^0$ with almost equal probability. Due to the small Q-value of the process, the B mesons are almost at rest in the center of mass frame. The accelerators are asymmetric, that is with two beams at different energies. The purpose is to produce B-mesons not at rest, but with a Lorentz boost $\beta\gamma$, so in the laboratory frame the mesons have a decay length allowing the separation between their two decay vertices.

The distance between decay vertices helps in separating the analysis in two sides: one is the *tag* side and the other the *signal* side. In the *tag* side, the final state particles are used to infer the flavor of the decaying B meson, so to understand if at the decay time it was a B^0 or a \bar{B}^0 . Thanks to this information, and knowing the time evolution of an oscillating B meson, it is possible to reconstruct the flavor of the B meson in the *signal* side, which decays in the final state $|f\rangle$ eigenvalue of CP. Once the flavor of the in the *signal* side is known, the measure of the decay amplitude of B and \bar{B} in $|f\rangle$ are compared.

In table 5.1 the principal properties of the $\Upsilon(4S)$ and of B-mesons are summarized. Although the main feature is the B meson production, these colliders can also be used to study other particles, such as τ leptons or charmed particles, for which the production cross section is highlighted in table 5.2.

| | | | | |
|----------------|-------------------------|-------|-------------------|-------------------|
| | M [GeV/c ²] | J^P | Γ [MeV] | quark composition |
| $\Upsilon(4S)$ | 10.579 ± 0.001 | 1^- | 20.5 ± 2.5 | $b\bar{b}$ |
| | M [GeV/c ²] | J^P | τ [ps] | quark composition |
| B^+ | 5.2792 ± 0.0003 | 0^- | 1.638 ± 0.004 | $u\bar{b}$ |
| B^0 | 5.2796 ± 0.0002 | 0^- | 1.519 ± 0.004 | $d\bar{b}$ |

Table 5.1: Table with main characteristics of $\Upsilon(4S)$ and B mesons. Values taken from [1]

| $e^+e^- \rightarrow$ | σ [nb] | $e^+e^- \rightarrow$ | σ [nb] |
|----------------------|-------------------|----------------------|----------------------|
| $u\bar{u}$ | 1.61 | e^+e^- | 300 ± 3 |
| $d\bar{d}$ | 0.40 | $\mu^+\mu^-$ | 1.148 |
| $c\bar{c}$ | 1.30 | $\tau^+\tau^-$ | 0.919 |
| $s\bar{s}$ | 0.38 | $\nu\bar{\nu}$ | $0.25 \cdot 10^{-3}$ |
| $\Upsilon(4S)$ | 1.110 ± 0.008 | | |

Table 5.2: Values of the total cross section of e^+e^- for two final state quarks or two final state leptons. Values taken from [54]

The main advantages of *b-factories* in the search for new physics are briefly listed [55]:

- the events are much cleaner with respect to the ones at hadronic colliders, and the trigger efficiency is higher. This allows a better environment in which to study forbidden or extremely rare processes.
- missing-mass analyses are easier thanks to a precise knowledge of the initial state and a detector with an almost complete solid angle coverage. This type of study is important for all new states with at least one invisible final particle.
- in general the number of tracks per event is limited (~ 10 per event [56]). This makes the reconstruction of charged final states more efficient.

The first generation of *b-factory* were BaBar at PEP-II and Belle at KEKB: the first located at the SLAC laboratory in California, the second at the KEK laboratory in Japan. Both experiments required high luminosity because the B decays interesting for CP violation have small branching fraction. The design luminosity of BaBar and Belle were $L=1.2 \cdot 10^{34} \text{cm}^{-2} \text{s}^{-1}$ and $L=2.1 \cdot 10^{34} \text{cm}^{-2} \text{s}^{-1}$ respectively (values taken from [55]). While BaBar has ceased collecting data, the Belle experiment has been upgraded with the Belle II experiment, which is presented in the following section.

5.2 Belle II

Belle II is an experiment located in Japan, at the SuperKEKB accelerator. It is the upgrade of the previous experiment Belle. The innovations made to the accelerator and the detector are so to obtain higher rate events for more statistics and to gain better precision. The peak luminosity is designed to reach $L=8 \cdot 10^{35} \text{cm}^{-2} \text{s}^{-1}$, and the detector has been designed for a 30kHz event rate.

5.2.1 Accelerator

A scheme of the Super KEKB accelerator is given in figure 5.1. As in the other B-factory accelerators, SuperKEKB has two asymmetric beams. In particular the electron beam has energy $E_{e^-} = 7 \text{ GeV}$ and is named High Energy Ring (HER), the positron beam instead has energy $E_{e^+} = 4 \text{ GeV}$ and is indicated with Low Energy Ring (LER). With such beam energies, the Lorentz boost is $\beta\gamma = 0.28$. The two beams interact in the interaction point (IP) where the Belle II detector is located.

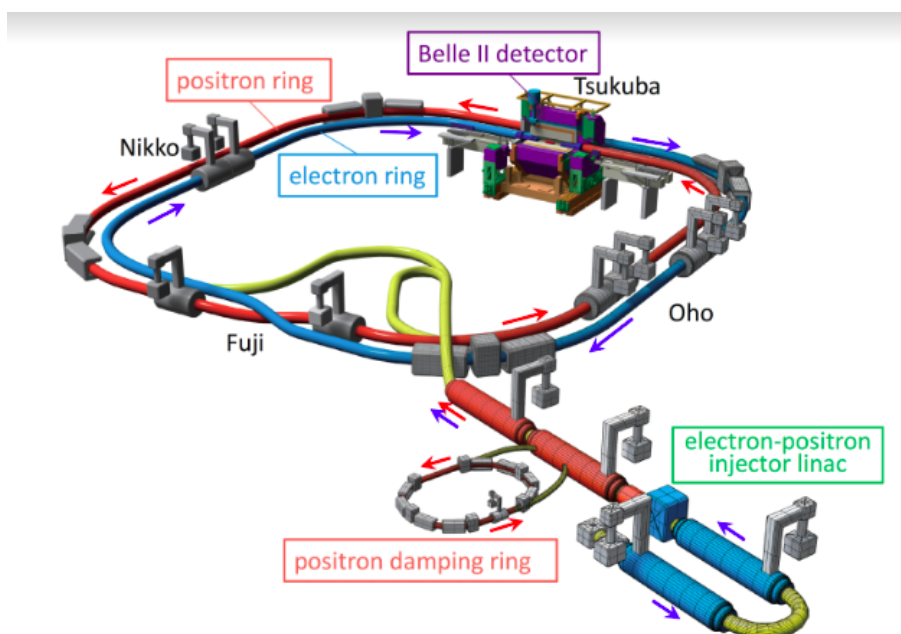


Figure 5.1: Schematic representation of the SuperKEKB accelerator. The Belle II detector is located at the interaction point of the two beams.

The luminosity of the machine can be estimated by the formula :

$$\mathcal{L} = \frac{N_b n_{e^+} n_{e^-} f}{A_{eff}} \quad (5.1)$$

with N_b number of bunches, n_{e^+}/n_{e^-} number of positron/electrons per bunch, f the circulation frequency and A_{eff} the effective overlapping area of the two beams in the IP. SuperKEKB plans to obtain a peak luminosity 40 times higher than KEKB by increasing beam currents and reducing the beam overlap area. Currents are limited by bunch instabilities and power consumption. The area reduction is achieved adopting the *nano-beam* scheme originally developed for SuperB project, and well described in [57].

5.2.2 Detector

In general a detector whose main goal is to study with precision rare events or find new physics must be able to :

- contain all the possible final state particles.
- minimize multiple scattering or energy loss allowing a better reconstruction of the particles trajectories and energies.

The main parts of the detector are outlined, and the most important ones highlighted afterwards:

- **Beam pipe:** the inner part surrounding the vacuum in which the beams collide. It has an inner radius of 1 cm.
- **Tracking system:** it consists of three co-axial cylindrical systems which reconstruct the trajectory of charged particles. The closest to the beam pipe are the two layers of the *Pixel Detector* (PXD) based on DEPFET technology. The second part is the *Silicon Vertex Detector* (SVD) made of double-sided silicon strip sensors. Lastly, the *Central Drift Chamber* (CDC), a large volume gas drift chamber with small drift cells. It is used to reconstruct trajectories of charged particles so to determine their momenta and provide particle identification using the dE/dx information. In addition, it also generates trigger information for charged particles.
- **Particle identification:** For particle identification, two detectors based on Cherenkov radiation are used. In the barrel region the time-of-propagation (TOP) counter is used, while in the forward end-cap there is the ring imaging detector with aerogel as Cherenkov radiator (ARICH).
- an **electromagnetic calorimeter** (ECL) is used to detect and measure photons and to identify electrons. It is based on CsI(Tl) scintillating crystals coupled with a fast electronic read-out system.
- In the outer part of the detector there is the K_L and μ detector (KLM), made by thick iron plates alternate with active elements

A presentation of the detector is given in figure 5.2

Pixel Vertex Detector

The PXD is made of two cylindrical layers co-axial with the beam pipe and at distance 1.4cm and 2.2cm, covering the angles $17^\circ < \theta < 150^\circ$. On the inner layer there are 8 ladders, with pixels of area $50 \times 50 \mu\text{m}^2$. The outer layer has 12 ladders where the pixels have size $50 \mu\text{m}^2$. The total read-out time is $20 \mu\text{s}$. The sensors are based

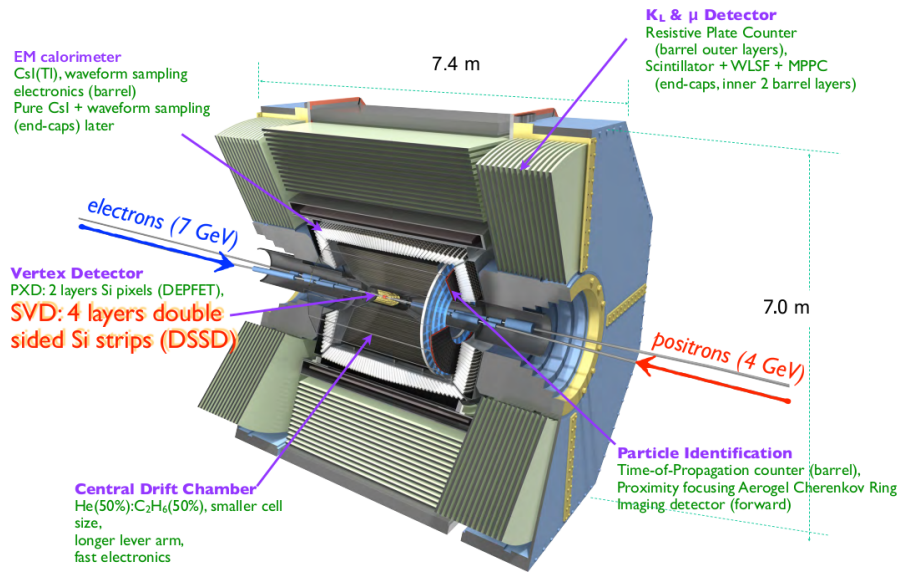


Figure 5.2: A representation of the Belle II apparatus. The main detectors are listed in the figure.

on DEPLETED Field Effect Transistor (DEPFET) technology, a semiconductor where the charge release by the crossing particles is used to modulate the current of a FET, obtaining internal signal amplification.

Silicon Vertex Detector

It is a system which, together with the PXD, is used to reconstruct the position of the charged particles. It has to work with an intense background rate. In order to achieve the best precision possible even for particles with low-momentum, the materials must be thin to keep multiple scattering low. The SVD is divided into four layers surrounding the IP, at a distance of 3.9 cm, 8 cm, 10.4 cm and 13.5 cm. Each layer carries a (different) number of ladders, and each ladder is equipped with a number of Double-Sided Silicon Strips Detectors (DSSD). The ladders in layer 3 consists of two equal rectangular sensors of size $123 \times 38 \text{ mm}^2$, while each ladder of layers 4, 5 and 6 has respectively 2, 3, 4 rectangular sensors of size $123 \times 58 \text{ mm}^2$ and one trapezoidal sensor in the forward region. The technology of DSSD is capable of giving a precise measure of two space coordinates of the particle position while remaining a thin component. This type of detector is based on the $p-n$ junction. In particular, in the DSSD the junction is asymmetrical, with a higher doped p region. This allows a larger depletion region, through which the electrons and holes, created from the passage of a charge particle, drift towards the electrodes. From the electrodes it is possible to measure the induced current, and infer the position and charge of the initial particle. The electrodes are divided in segments called *strips*, which are of two types: one orthogonal to the other in order to give information about the x - y coordinates. In order

to identify which strip is crossed, there is a cut on the signal to noise ratio (SNR).

CDC

The Central Drift Chamber is the central tracking device of the Belle II detector. It is a large gas volume with small drift chambers used to reconstruct the trajectories of charged particles to precisely determine their momenta, as well as provide trigger information for charged particles and particle identification information thanks to the energy loss in the volume. The CDC consists in two cylinders long 2.2m and with radius 1.70m (innermost cylinder) and 1.130m (outermost cylinder). The volume is filled with a gas mixture of 50% He and 50% ethanol. It is made up by 56 layers containing a total of 14.3k wires. The anode wires are $30\mu\text{m}$ thick while the cathode ones are $126\mu\text{m}$ thick. In the Belle CDC the wires were all distant $10 \div 18\text{mm}$. In the Belle II CDC the first 8 layers have wires distant $6 \div 8\text{mm}$, improving the dimensions of the drift cells to better handle the high background rate.

TOP

The TOP detector is located in the barrel region, between the CDC and the ECL. It has radius of 1.24m and it is composed of 16 detectors. The purpose of the TOP detector is to give information on the nature of the detected particle and improve the K/π separation. It exploits the Cherenkov effect using quartz bars (45cm wide and 2cm thick) as radiating elements, and it measures the time of propagation of the photons in the bars. The bars have at one end a focus mirror, and at the other end micro-channel plate photomultipliers (MCP-PMTs). Each photon propagates in the bar via total reflection on the inner walls of the quartz, so to preserve the Cherenkov angle it is emitted at. The focus mirror directs the photons to the MCP-PMTs. The photomultipliers have a gain of $\sim 10^6$, they give the propagation time measurement and also information on the x - y arrival coordinates, all three used to reconstruct the Cherenkov ring image. The time resolution is of $\sim 50\text{ps}$, while the spatial resolution is of order $\sim \text{mm}$. The detected photons associated to each track are tested against two probability distribution functions (PDF): one relative to a π particle hypothesis and one relative to the K particle hypothesis. From the PDFs it is possible to determine the likelihood of the photons coming from a π or K particle, thus allowing a separation between the two cases.

ARICH

The ARICH is in the forward region and has an radius of 410mm and an outer one of 1.140m. The ARICH exploits the Cherenkov effect to further discriminate between K and π with momentum $\sim 4\text{GeV}/c$ and between π , μ and e with momentum $\leq 1\text{GeV}/c$. It uses Aerogel as radiator, divided in two layers, each 2cm thick, with

different refractive indices $n_1 = 1.045$ and $n_2 = 1.055$, a method used to improve the signal yield and keep a good resolution on the Cherenkov angle. The Cherenkov photons are detected by hybrid avalanche photon detector (HAPD), which are vacuum tubes including avalanche-diode type photo-detector. The photons hitting the photocathode produce electrons by photo-electric effect, electrons which are accelerated towards the avalanche detectors. The number N of detected photons effect the angular resolution as $\sigma_{\theta_C}^N = \theta_{\theta_C}/\sqrt{N}$. For each track an average number of 20 photons are detected, which leads to a resolution of $\sigma_{\theta_C}^N \sim 3$ mrad.

Electromagnetic Calorimeter

The ECL has different functions:

- detect photons with high efficiency, and determine precisely their energy and angle.
- detect electrons.
- provide trigger signal.
- measure K_L together with the KLM.

The ECL is composed by segments of CsI(Tl) crystals, reused from the Belle detector. The ECL is made up by a 3.8 m long barrel region with inner radius of 1.25 m, and two endcaps respectively at 1.96 m forward the IP and 1 m backward the IP. The overall angular acceptance is from $\theta \sim 12^\circ$ to $\theta \sim 150^\circ$ (with a gap of $\sim 1^\circ$ where the endcaps meet the barrel) which covers up to 90% of the solid angle in the center of mass frame. The crystals have an average cross section size of 60×60 mm² and a 300 mm length, corresponding to $16.2X_0$. The lateral size of the crystals is comparable with the Moliere Radius, and the thickness is enough to minimize energy leakage for photons with several GeV. The CsI(Tl) crystals have a scintillation light corresponding to ~ 5 k photons per MeV with decay constant of $\sim 1.3 \mu$ s. The light is detected by two photo-diodes with sensitive area of 10×20 mm² attached at the back of the crystals. One of the two output is shaped with a time constant of 0.2μ s and is used for trigger signal, the other is shaped with time constant 0.5μ s and is used to extract amplitude and time information thanks to waveform sampling. The noise level is of 200 keV. The resolution obtained from the ECL is of $\sigma_{E/E} = 4\%$ for particles with energy ~ 100 MeV, while it lowers at $\sigma_{E/E} = 1.8\%$ for energies from 8 GeV.

KLM

The outermost detector is the KLM, composed by a sandwich of iron plates and active detector elements. The iron plates are 4.7 cm thick, providing a 3.9 interaction length which, summed to the 0.8 interaction length of the ECL, allows the K_L to shower

hadronically. The iron plates also serve as the magnetic flux return for the solenoid. The active detectors consist in Resistive-Plate-Chambers (RPC) and scintillators strips with silicon multipliers (SiPM). The RPCs are electrodes made by two 2mm spaced layers of highly resistive glass with a gas mixture in the gap. The charged particle passing through ionize the gas and the signal is read by metal strips located on each side of RCPs. The RCPs have a long dead time, when compared to the background rate. For this, in the endcaps and in the innermost layers, the RCPs have been replaced by scintillators strips. The light produced in the strips is read by the SiPM, which have a time resolution of 7ns. The KLM has an angular acceptance of $20^\circ < \theta < 155^\circ$ and a muon efficiency $\varepsilon_\mu \sim 89\%$ and a K_L^0 efficiency of $\sim 80\%$.

In table 5.3 the main detectors and their characteristics are summarized.

| Measurement | Belle II |
|-------------------------|---|
| B vertex reconstruction | $\sigma_z \sim O(26 \mu\text{m})$ |
| Tracking | $\sigma_{p_t}/p_t = 0.0011 [\text{GeV}/c]$ |
| $K\pi$ ID | $\varepsilon_K \sim 0.90$ with $\varepsilon_\pi = 0.04$ for $p = 2 \text{ GeV}/c$ |
| Calorimetry | $\frac{\sigma_E}{E} = 7.7\%$ at 0.1 GeV, 2.25% at 1 GeV |
| Muon ID | $\varepsilon_\mu = 0.92 - 0.98$ |
| L1 Trigger | 30kHz max |

Table 5.3: Summary table for detective performance, with values taken from [58].

Trigger

The trigger system must be able to distinguish physics from the background. For the Belle II experiment, the trigger requirements include: $\sim 100\%$ efficiency for hadronic events coming from the $\Upsilon(4S)$ decay; average trigger rate below 30kHz, fixed latency around $5 \mu\text{s}$ and a timing precision $\leq 10\text{s}$.

The trigger system is composed by the Level 1 trigger and the High Level trigger:

- *Level 1 trigger* is a hardware-based system which collect information from different detector parts, mainly based on the CDC and ECL trigger information, but also TOP and KLM. Once the low-level reconstruction is complete, a logic system releases a trigger signal whenever selection criteria are satisfied. It is important to highlight the CDC as trigger, because it can give a 3D trigger, which is important for background rejection. In fact, background events have a z -coordinate which does no come from the IP, while the events produced in the e^+e^- have a z -coordinate which is nearly zero. The ECL trigger is useful for identifying Bhabha and $\gamma\gamma$ events

- *High Level trigger*: this type of trigger uses the information coming from all the detectors, and reconstructs fully the events passing the L1 trigger. It uses the same offline reconstruction software used for analysis.

5.2.3 Software

Belle II experiment provides all the members with a specific software in order to manage the large amount of data collected from the detector.

In a database, the raw data is collected along with calibration constants of the detector depending on the status of the accelerator and the sub-detectors. Once the raw data is processed, the high-level information is stored in files named mDST, in which NTuples are used to split and save the information the user needs. The same storage method is used for Monte Carlo (MC) simulations, which sample size is larger than the real data.

Analysis on the stored information is made offline thanks to the internal software called Belle Analysis Framework 2 (*Basf2*). The software make use o *modules* written in C++ language. They implement the desired operations such as generation of MC samples, simulation of the detector and reconstruction of particle tracks. They access *data-objects* saved in a common repository where all the information about the detector and other modules are saved, and any module can access, read and write *data-objects*.

The *modules* are inserted in Python3 scripts called *steering-files* which set the desider parameters and put the *modules* in a *path*, which determine the order in which the *modules* are called.

Basf2 also uses other software packages for different purposes: for handling data it uses ROOT, EvtGen for generating $B\bar{B}$ events and GEANT4 for the detailed description of the detector material and the simulation of its interaction with particles.

The Belle II apparatus is a good candidate in which to test the QCD axion model presented in chapter 3 and the dark matter candidate of chapter 4. In the following paragraphs I will present a study on two channels involving the two models.

6. Simulation for QCD axion model

In the previous chapters a new pseudoscalar field is introduced and two possible interpretations are described, with a particular attention on the possible phenomenological signatures. In this chapter I will focus on the QCD axion model and study the coupling between the axion and electrons through the simulation of a specific channel.

The axion particle represents a new type of particle, giving rise to new processes. The experimental search for new physics signature has to deal with the already known and described processes of the Standard Model giving the same signature, which go under the name of background events. Background events could mask the events coming from the new processes, so in the analysis it is important to discriminate at best the signal events and background events.

The channel used to study the axion-electron coupling is:

$$e^+ e^- \rightarrow \gamma a \rightarrow \gamma e^+ e^- \quad (6.1)$$

where the axion a has mass in a range from $15\text{MeV}/c^2$ to $30\text{MeV}/c^2$. Such channel can probe the parameter space in figure 3.1 still not excluded.

The final state particles can be given by different background processes, the main one being $e^+e^- \rightarrow \gamma\gamma \rightarrow \gamma e^+e^-$ where one of the final state photons undergo pair conversion in the detector material. It is the main background because the invariant mass of the final fermions is zero ($m_\gamma = 0\text{GeV}/c^2$), almost as in the signal events coming from the signal process 6.1, where the axion mass can be considered almost zero when compared to the mass value at which the detector is set ($O(\text{GeV}/c^2)$).

The study aims at putting a preliminary upper limit on the sensitivity obtainable with the Belle II experiment on the coupling parameter Q_e/f_a . The sensitivity on a parameter represent the smallest value of the parameter that the analysis can appreciate at a given confidence level (CL). The sensitivity can be given for the cross section of the interesting process. From the dependence of the cross section on the parameters of the model, it is possible to infer the sensitivity on the parameters.

In the case of a QCD axion with mass in the MeV/c^2 range, the differential cross section for axion production is:

$$\frac{d\sigma_{e^+e^- \rightarrow \gamma a}}{d\cos\theta_\gamma} = \left(\frac{Q_e}{f_a} m_e\right)^2 \cdot \frac{\alpha}{2\sqrt{1 - \frac{4m_e^2}{s}}} \cdot \frac{1}{s \cdot \sin^2\theta + 4m_e^2 \cos^2\theta} \quad (6.2)$$

where θ_γ is the polar angle of the final-state photon respect the beam axis, while s is the invariant mass $\sqrt{s} = 10.58\text{GeV}$. The electron charge under the symmetry $U(1)_{PQ}$ is Q_e and f_a is the energy scale at which the symmetry is broken.

The differential cross-section is integrated in the Belle II acceptance angles $16^\circ <$

$\theta < 150^\circ$. A cut and count operation is made on the angular acceptance.

$$\sigma_{e^+e^- \rightarrow \gamma a} = \frac{4\alpha}{\sqrt{s}} \left(\frac{Q_e}{f_a} m_e \right)^2 \frac{1}{1 - \cos^2 \theta_\gamma + \left(\frac{4m_e^2}{s} \right) \cos^2 \theta_\gamma} \Big|_{\theta_\gamma^\downarrow}^{\theta_\gamma^\uparrow} \quad (6.3)$$

Once the sensitivity on the integrated cross section is known, it can be rephrased as sensitivity on the Q_e/f_a .

In the search for new physics against background events, the sensitivity is given by $S = \frac{s}{\sqrt{B}}$ where s is the number of signal events and B the number of background events. Both quantities are proportional at the luminosity of the machine, so the sensitivity scales as $\propto \sqrt{L}$. The sensitivity is estimated through a *cut and count* method: count the number of signal events vs the count of background events after a selection is applied.

The Feynman diagram for the process is in figure 6.1. The signature will be one final state photon and two tracks of equal and opposite charge with a vertex coming from the IP, because of the prompt axion decay. The photon is reconstructed in the ECL, while the charged particles are mainly reconstructed by the CDC. The SVD plays an important role in the right reconstruction of the decay vertex of the axion, especially when background is introduced (see after)

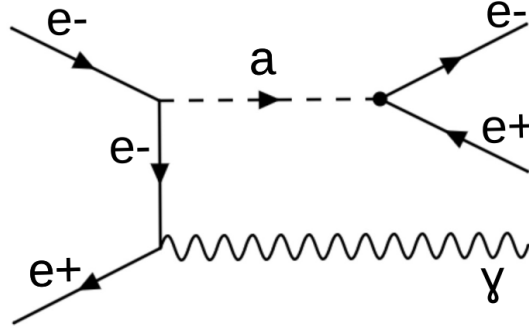


Figure 6.1: Feynman diagram of the studied channel. The interesting coupling are the ones between axion particle and the electrons.

The initial electron and positron collide at an energy in the center of mass equal to the $m_{\Upsilon(4s)} = 10.58 \text{ GeV}/c^2$, so the invariant mass of the event is expected to have a peak in the range $9 \div 12 \text{ GeV}/c^2$. The final state is composed by three particles, but the decay involving the axion is a two body decay, so axion and photon have fixed energy in the center of mass frame.

The outline of the sensitivity study discussed in the next sections is as follows:

- generation, simulation and reconstruction of signal events.

- study of the background processes.
- choice of variables and cuts for event preselection.
- study of the mass of the axion, obtained from the invariant mass of final state e^+e^- .
- choice of a variable for of background rejection
- estimation of the 90% CL sensitivity on the cross section.
- recast of the estimate on the coupling parameter.

6.1 Signal

In general the simulation of events is subdivided in three parts: generation of physical process, simulation of the detector response and reconstruction of the event tracks in the detector. In this section I shortly explain the generation and simulation steps, while in the next section there is the explanation of the reconstruction part, which is done both for signal and background.

6.1.1 Generation

The first step consists in generating the physical process of interest in the detector. This means generating the quadri-momenta of the particles in the process in the expression 6.1 crossing the detector as expected by the model describing the process. To generate the signal event I have used the program MadGraph5 [59]. The program takes as input the lagrangian describing the interaction, and the theoretical values of the coupling parameters; as output it gives the matrix elements and the cross section value for the process.

The axion mass of the generated events is labeled by m_a ; I have generated events for thirteen different mass values: from $m_a = 20\text{MeV}/c^2$ to $m_a = 30\text{MeV}/c^2$ with a step corresponding to $1\text{MeV}/c^2$, plus two values at $m_a = 15\text{MeV}/c^2$ and $m_a = 17\text{MeV}/c^2$. For each mass value I have generated 20000 events, in order to have sufficiently high statistics, since not all of the generated events are correctly simulated or reconstructed. For 20000 events generated, the final simulated and reconstructed events are in the order of ~ 7200 events.

The choice of the mass range from $20 - 30\text{MeV}/c^2$ is motivated by the parameter space shown in figure 3.1. The two lower mass are included to probe the sensitivity of the Belle II detector in the lower mass range. The $\sim 17\text{MeV}/c^2$ has recently received a lot of attention because of an anomaly in the berillium nuclear transitions reported by the Atomki collaboration that could be explained by a neutral spin 1 light boson of mass $\sim 17\text{MeV}/c^2$ [60].

6.1.2 Simulation

This part consists in simulating the passage of the generated particles in the detector components. For the Belle II experiment, this is done thanks to the toolkit *Generation and Tracking 4 (GEANT4)* [61]. It uses the generated impulses to simulate the physical interactions between the particles and the detector material (ionisation, pair production, bremsstrahlung ecc). In the end, it gives the energy deposit in all the sub detector and the electronic readout of the sensors, raw data which is as close as possible to the data produced by the passage of real particles. For example, in the *SVD* the energy deposited by the simulated particles is used to compute the signal on the strips of the detector, calculated taking into account also the noise, the response of the near strips and the readout electronics. The process of converting the information given by *GEANT4* into hits in all the sub detectors is called *digitization*.

6.1.3 Reconstruction

The reconstruction provides the trajectory of the particles and the particle identification from the raw data coming from the detector response. The data can be either from simulated events or real events, in both cases the reconstruction process is the same.

The first step is to group the hits in the sub detectors caused by the passage of a particle into *clusters* and to analyze their shape, size and center. From patterns in the clusters, it is possible to either reconstruct the track left by the particle inside the material, or perform a fit on the kinematic variables of the particle in order for its trajectory to match the pattern in clusters. From the response of the sub detectors involved in the passage of a particle, it is also possible to perform the particles identification.

When a particle decays too quickly and does not reach the detector components, the track is reconstructed through the decay products. Working backwards, it is possible to reconstruct a whole decay chain and infer the information regarding the mother particle, or any particle in between.

At the end of the reconstruction, the information coming from the detector is organized in tracks associated with identified particles. This is the last step in order to have variables useful for an analysis, such as the energy of the incoming particle, or its position.

The reconstruction is made through the *steering-files* which control the workflow of the Belle II software. The *steering-file* used in this study has the following structure.

Firstly the reconstructed tracks have to be associated to a certain type of particle, and they are stored into a list of particles. This is done with the module **fillParticleList**: all the simulated particles are filtered with some request, the ones fulfilling such request are stored into a list and associated with the specific particle type imposed by the user. For the channel in 6.1 this module is used to create lists of photons and electrons. The main request for a particle to enter the photon list is to have an emission angle in the acceptance of the ECL, so $16^\circ < \theta_\gamma < 150^\circ$. For the electrons

particle list the important requirement is on the probability of electron identification using info from all the detectors, and it was set at $\text{electronID} > 0.5$.

After the lists are created, the module **reconstructDecay** is used to create a new particle from the reconstruction of a decay chain involving the particles of the lists. The axion is reconstructed through its decay into electron and positron $a \rightarrow e^+e^-$: the module matches the tracks compatible with electrons and positrons, according to the charge and momentum, and combines their momentum to compute the axions one. It is important to reconstruct electrons and positrons coming from the same particle. To this end vertex fit is performed, so to constrain the two charged tracks into coming from the same vertex. The function **vertex.treeFit** performs a fit for the axion decay chain, finding the best decay vertex position and momenta for the decaying particle.

Once the vertex fit is made, the whole decay chain $\Upsilon(4S) \rightarrow \gamma a \rightarrow \gamma e^+e^-$ is reconstructed from the particle list, and the request is that of two charge tracks in the final state. Then a check on the output of the reconstruction is made through the module **matchMCTruth**. The module compares the generated events with the reconstructed one, and it allows to understand if a certain candidate was actually generated or was given by an erroneous reconstruction procedure.

At the end of the reconstruction, for each particle different variables useful for analysis can be saved, such as the particle energy, its momentum and so on. Such information's stored in root files called Ntuple

6.2 Background

Background include processes with same final state as the signal, or can be confused with the signal. The main background for the process $e^+e^- \rightarrow \gamma a \rightarrow \gamma e^+e^-$ are:

- $e^+e^- \rightarrow e^+e^- \gamma$ indicated as Bhabha scattering with radiation of one photon. The cross section for this background is $\sigma = 300\text{nb}$ [54]. These background events will be indicated with e^+e^- .
- $e^+e^- \rightarrow \gamma\gamma \rightarrow \gamma e^+e^-$ this two-photon process is predominant in the low mass region ($O(\text{MeV}/c^2)$) [62]. The cross section is $\sigma = 4.9\text{nb}$ [54]. This type of background will be labelled by $\gamma\gamma$

For this analysis, the background is taken from the official Monte Carlo campaign (MC14) run independent with size 200fb^{-1} . The ones listed represent the SM background, but some other background can come from other processes, with particles getting lost in the beam pipe. The *steering-file* for the reconstruction is the same used for signal events and background events.

6.3 Event preselections

A set of preselections in the reconstruction phase are made to reduce the number of candidates from background events while keeping a high efficiency on the event signal. The preselections are:

- total invariant mass M around the $\Upsilon(4S)$: $9 < M < 12 \text{ GeV}/c^2$ (see figure 6.2)
- one reconstructed photon in the final state
- two charged tracks with $\text{electronID} > 0.5$
- opposite charge for the two tracks
- energy of the final state photon E_γ greater than 3 GeV . (see figure 6.3)

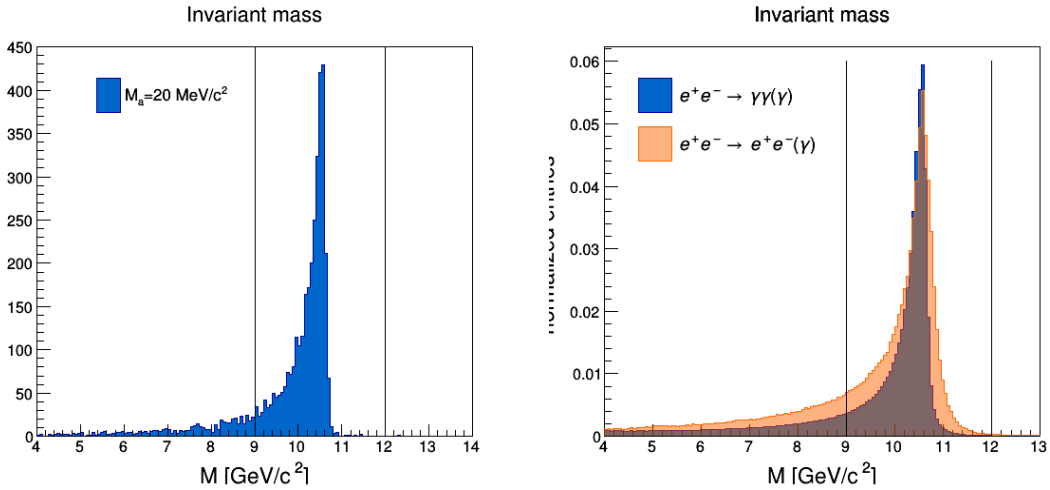


Figure 6.2: The invariant mass M of the whole event is peaked around $m_{\Upsilon(4S)} = 10.58 \text{ GeV}/c^2$. On the left, the distribution for signal events at the example mass generated at $m_a = 20 \text{ MeV}/c^2$. On the right, the same distribution for the two main background processes. The right distributions are normalized. The two vertical lines represent the preselection on the invariant mass of the event $9 < M < 12 \text{ GeV}/c^2$

The figure 6.3 shows the final state photon energy distribution both for signal events and background events. The axion and photon in equation 6.1 come from a two-body decay, so their energy is fixed at $\sim 5.3 \text{ GeV}$ in the center of mass frame. In the laboratory frame, because of the Lorentz boost, the energy is no longer monochromatic and shows peaks at the sides in correspondence of the boost at angles $\theta = 0^\circ, \theta = 180^\circ$. Both for the signal events and the $\gamma\gamma$ background the final state photon comes from a two-body decay, so the two E_γ distribution have similar shape. The

other background has a final state photon only in the case of initial or final state radiation, so the energy of such photon is not fixed. The energy distribution in the lab frame is different respect to the signal photon and the background photon.

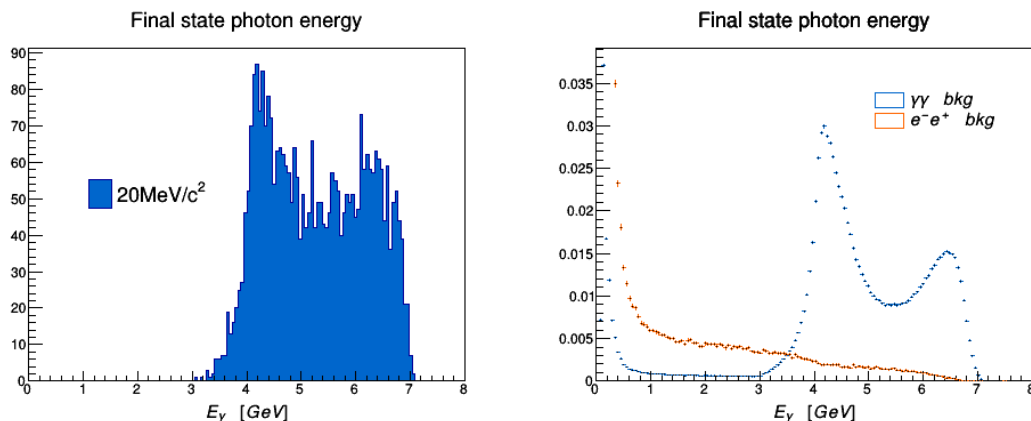


Figure 6.3: Distribution of the energy E_γ of the final state photon for background (right) and signal (left) events, the latter one at the mass value $m_a = 20\text{MeV}/c^2$. The distributions in case of signal and $\gamma\gamma$ background events are concentrated at the energies $E_\gamma \in 3 \div 7\text{GeV}$, while the e^+e^- background distribution peaks at lower energies $E_\gamma < 1\text{GeV}$. Only events with $E_\gamma > 3\text{GeV}$ are selected.

The final electrons invariant mass distribution for the background events is plotted in figure 6.4. It shows that the main background in the region of interest is the $\gamma\gamma$ background. The rest of the work will concentrate on a variable which discriminates at best this component from the signal events.

The efficiency ε for the signal events is in table 6.1. It is calculated as the number of events counted after preselections vs the number of generated events (20000).

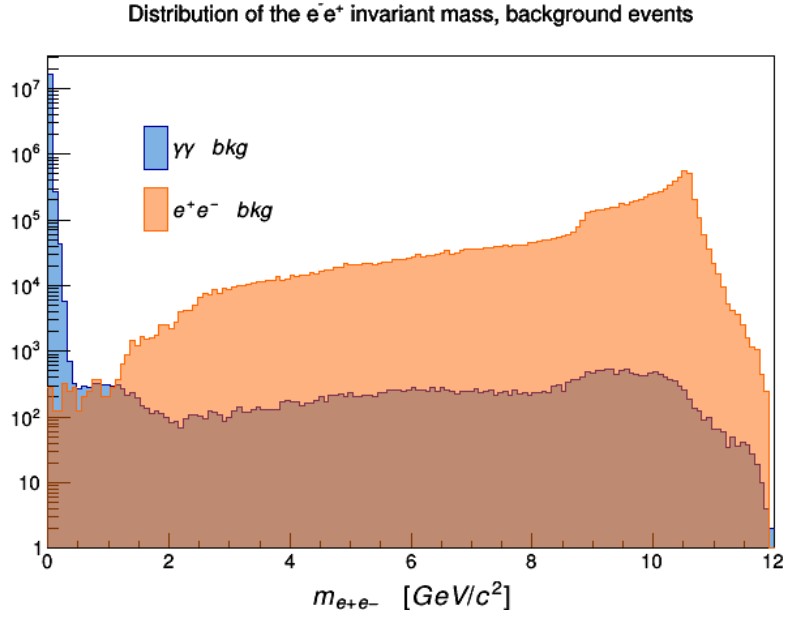


Figure 6.4: distribution of the final e^+e^- invariant mass for $\gamma\gamma$ and e^+e^- background. The $\gamma\gamma$ background is predominant in the region of interest which is $15 - 30 \text{ MeV}/c^2$

| m_a [MeV/ c^2] | ε % | m_a [MeV/ c^2] | ε % |
|---------------------|-----------------|---------------------|-----------------|
| 15 | 10.3 | 24 | 12.9 |
| 17 | 11.4 | 25 | 13.4 |
| 20 | 12.6 | 26 | 13.5 |
| 21 | 12.7 | 27 | 13.6 |
| 22 | 12.9 | 28 | 13.7 |
| 23 | 13.2 | 29 | 14.2 |
| | | 30 | 14.1 |

Table 6.1: Table with the signal efficiency ε for each mass value. The efficiency is relative to the number of generated and reconstructed events after the preselections are applied.

6.4 Region for sensitivity optimization

The sensitivity is calculated with a coarse formula which is essentially the ratio between the number of background events and the signal events. It is necessary to define a region in which to compare the two type of distributions (signal and background). The region is defined in the mass of the axion, which is given by the invariant mass of the final state e^+ and e^- . The region is a window in the mass distribution with a width depending on the resolution of the mass peak σ_{peak} .

6.4.1 Mass peak

The mass of the axion is reconstructed as the invariant mass of the final state electron and positron. While the generated axion mass is indicated with m_a , the mass coming from the final e^+e^- invariant mass is indicated with $m_{e^+e^-}$

$$m_{e^+e^-} = \sqrt{E_{e^+}E_{e^-} - 2p_{e^+}p_{e^-}\cos\theta} \quad \cos\theta = \frac{p_{e^+} \cdot p_{e^-}}{|p_{e^+}| \cdot |p_{e^-}|} \quad (6.4)$$

In figure 6.5 there is one example of the invariant mass distribution, reconstructed as in equation 6.4. The invariant mass of the dielectron system is obtained through the measurement of the particle momentum given by the detector components (specifically the CDC)

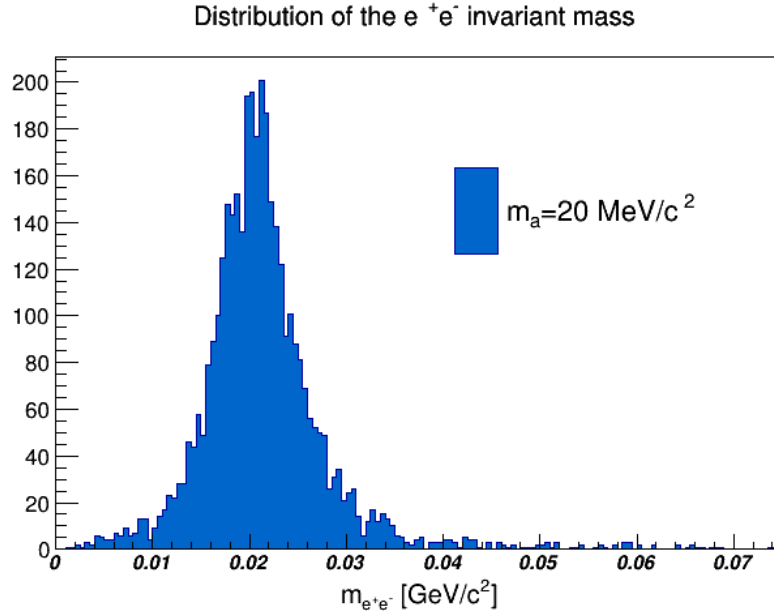


Figure 6.5: An example of the invariant mass $m_{e^+e^-}$ of the final state e^+e^- , from which the axion mass is reconstructed. The image shows the distribution of the reconstructed $m_{e^+e^-}$ for events in which the axion is generated with mass $m_a = 20 \text{ MeV}/c^2$. For lower generated masses, $m_a = 15 \text{ MeV}/c^2$ to $m_a = 23 \text{ GeV}/c^2$, the distributions show an asymmetric shape, with a higher tail on the right side of the peak. The peak shape tends to be more symmetrical from $m_a = 24 \text{ MeV}/c^2$ to $m_a = 30 \text{ MeV}/c^2$.

A preliminary fit to the invariant mass peak was made so to have an estimation of the peak resolution. The resolution σ_{peak} will be used to select a window in the mass distribution where to confront background and signal.

The function used to fit the distributions is a sum of a gaussian function and a crystalball function. The gaussian function (not normalized) is defined as:

$$G(x, \mu, \sigma) = e^{-\frac{(x-\mu)^2}{2\sigma^2}} \quad (6.5)$$

The crystalball function (not normalized) with a tail on the right side is defined as:

$$Cb(x, \alpha, n, \sigma, \mu) = \begin{cases} e^{-\frac{(x-\mu)^2}{2\sigma^2}} & \frac{x-\mu}{\sigma} < -\alpha \\ \left(\frac{n}{|\alpha|}\right)^n \cdot e^{-\frac{|\alpha|^2}{2}} \cdot \left(\frac{n}{|\alpha|} - |\alpha| - \frac{x-\mu}{\sigma}\right)^{-n} & \frac{x-\mu}{\sigma} \geq -\alpha \end{cases} \quad (6.6)$$

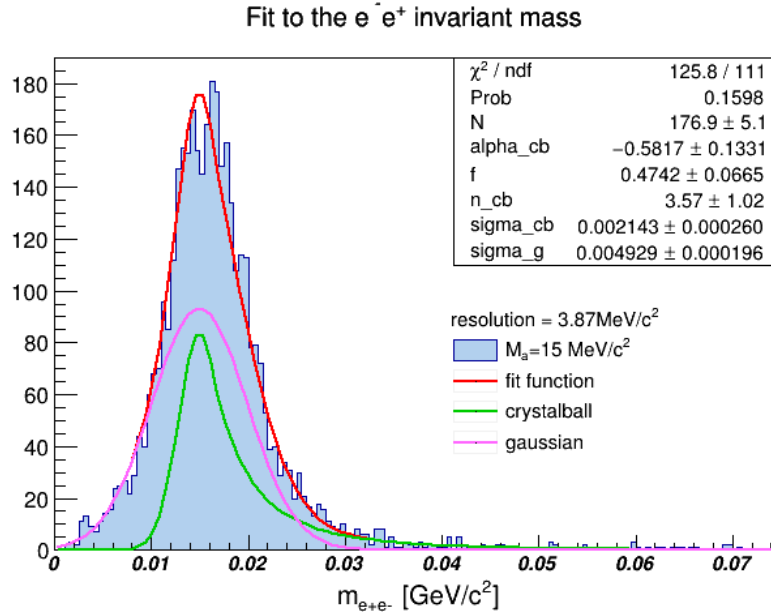
It represents a gaussian function with a tail on one side. The parameters α and n regulate the starting point of the tail and its shape. For a crystalball with a tail on the right side, the α values are negative.

The fit function is the sum :

$$y = N \cdot [f \cdot Cb + (1 - f) \cdot G] \quad (6.7)$$

N is a global normalizing factor, f is a parameter weighting the two functions. For both G and Cb , the mean μ_g and μ_{cb} , are fixed at the corresponding generated mass value m_a for each distribution, so the total number of free parameters to fit is 6.

An example of fit is given for two distributions in figure 6.6



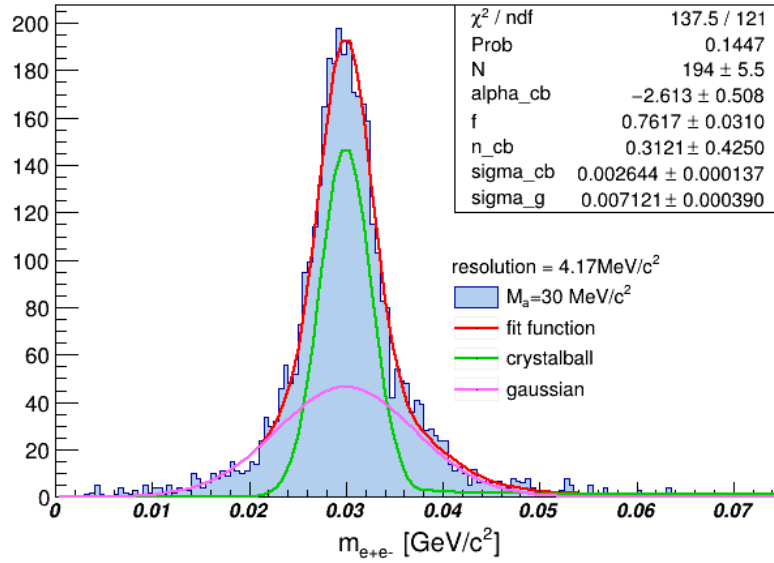


Figure 6.6: Example of fit of the invariant dielectron mass distribution for two generated mass values: $m_a = 15 \text{ MeV}/c^2$ (top) and $m_a = 30 \text{ MeV}/c^2$ (bottom). The red line is the fit function y , the green line corresponds to the crystalball function and the pink one to the gaussian function. In the box, the resulting χ^2 (full list in table 6.4) and the fitted parameter values (full list in tables 6.2 and 6.3). For each figure, the resolution is written. The figure relative to the $m_a = 15 \text{ MeV}/c^2$ generated mass shows a more asymmetric distribution, hence the crystalball tail is more accentuated, while for the $m_a = 30 \text{ MeV}/c^2$ distribution the tail is almost nonexistent.

The values of the fitted parameters are listed in table 6.2 and 6.3.

| m_a [MeV/c ²] | α_{cb} | n_{cb} | σ_{cb} [MeV/c ²] |
|-----------------------------|---------------|-----------|-------------------------------------|
| 15 | -0.6 ± 0.1 | 3.6 ± 0.1 | 2.1 ± 0.2 |
| 17 | -0.4 ± 0.1 | 2.8 ± 0.5 | 1.4 ± 0.3 |
| 20 | -1.0 ± 0.1 | 2.1 ± 0.4 | 2.6 ± 0.2 |
| 21 | -1.0 ± 0.2 | 2.0 ± 0.5 | 2.3 ± 0.2 |
| 22 | -1.3 ± 0.2 | 1.8 ± 0.4 | 2.9 ± 0.2 |
| 23 | -1.3 ± 0.2 | 1.8 ± 0.4 | 2.7 ± 0.2 |
| 24 | -1.5 ± 0.2 | 1.3 ± 0.3 | 2.6 ± 0.2 |
| 25 | -1.8 ± 0.2 | 1.0 ± 0.3 | 2.7 ± 0.2 |
| 26 | -1.6 ± 0.2 | 1.0 ± 0.3 | 2.4 ± 0.2 |
| 27 | -1.8 ± 0.2 | 1.1 ± 0.3 | 2.6 ± 0.1 |
| 28 | -2.0 ± 0.2 | 0.8 ± 0.3 | 2.7 ± 0.1 |
| 29 | -2.6 ± 0.1 | 0.3 ± 0.3 | 2.7 ± 0.1 |
| 30 | -2.6 ± 0.5 | 0.3 ± 0.4 | 2.6 ± 0.1 |

Table 6.2: Fit values for the 3 free parameters of the Cb component of the fit function y . From left to right: α_{cb} , n_{cb} the crystalball parameters regulating the tail shape, σ_{cb} the crystalball standard deviation.

| m_a [MeV/c ²] | σ_g [MeV/c ²] | f | N |
|-----------------------------|----------------------------------|-------------|---------|
| 15 | 4.9 ± 0.2 | 0.47 ± 0.06 | 176 ± 5 |
| 17 | 4.7 ± 0.2 | 0.43 ± 0.05 | 184 ± 6 |
| 20 | 5.6 ± 0.4 | 0.69 ± 0.06 | 185 ± 5 |
| 21 | 5.4 ± 0.2 | 0.56 ± 0.05 | 189 ± 5 |
| 22 | 6.4 ± 0.5 | 0.76 ± 0.06 | 181 ± 5 |
| 23 | 6.0 ± 0.3 | 0.68 ± 0.05 | 186 ± 5 |
| 24 | 6.2 ± 0.2 | 0.63 ± 0.04 | 179 ± 5 |
| 25 | 6.4 ± 0.3 | 0.68 ± 0.04 | 183 ± 5 |
| 26 | 5.9 ± 0.2 | 0.62 ± 0.04 | 188 ± 6 |
| 27 | 7.3 ± 0.4 | 0.79 ± 0.03 | 197 ± 6 |
| 28 | 6.7 ± 0.3 | 0.70 ± 0.03 | 181 ± 5 |
| 29 | 7.5 ± 0.3 | 0.80 ± 0.02 | 201 ± 5 |
| 30 | 7.1 ± 0.4 | 0.76 ± 0.03 | 194 ± 5 |

Table 6.3: Fit values for the other 3 free parameters of the fit function y . From left to right: σ_g the gaussian standard deviation, f the fraction factor and N the overall normalization factor.

For increasing m_a values, the parameters values given by the fit show the following trend: the parameter n_{cb} decreases; σ_{cb} is more or less stable; the absolute value of α_{cb} , the σ_g and the fraction f increase. The trend is compatible with the shape of the distributions. In fact, lower absolute values of α_{cb} correspond to a more accen-

tuated tail starting closer to the center of the peak, which is adequate for the lower mass values. On the contrary, for higher mass values the $m_{e^+e^-}$ peak becomes more narrow and symmetrical, so the tail is further away from the peak center and more suppressed. The decreasing value of n_{cb} is responsible for a greater tail suppression. When the crystalball tail becomes less significant, the symmetrical tails of the $m_{e^+e^-}$ peaks are gradually fitted with the gaussian component G and that is why the σ_g increase. The σ_{cb} remains stable and, because the peaks become more narrow, the f fraction regulating the Cb and G components increases so the peak is fitted mainly with the narrow crystalball.

The χ^2 obtained by the fit for each mass are listed in table 6.4

| $m_a[\text{MeV}/c^2]$ | χ^2/ndof | $m_a[\text{MeV}/c^2]$ | χ^2/ndof |
|-----------------------|----------------------|-----------------------|----------------------|
| 15 | 1.13 | 24 | 0.81 |
| 17 | 1.41 | 25 | 0.83 |
| 20 | 1.26 | 26 | 0.99 |
| 21 | 1.22 | 27 | 0.93 |
| 22 | 1.14 | 28 | 1.00 |
| 23 | 0.93 | 29 | 1.04 |
| | | 30 | 1.13 |

Table 6.4: For all mass values, the resulting χ^2 of the fit to the invariant mass distribution using the function y defined in equation 6.7

6.4.2 Resolution

The resolution on the mass peak is defined as:

$$\sigma_{peak} = \sqrt{f \cdot \sigma_{cb}^2 + (1 - f) \cdot \sigma_g^2} \quad (6.8)$$

where σ_{cb} and σ_g are relative to the Cb and G standard deviations respectively.

For each mass value, the resolution σ_{peak} was calculated as in equation 6.8 and the results are in table 6.5.

The values in table 6.5 are passed through the Savitzky–Golay filter [63]. This filter is used to increase the possible precision on the data without disturbing the signal tendency. It works by grouping data points into subsets of adjacent points which are then fitted with a polynomial by the linear least square method. From the fit procedure, a coefficient for each point in the subset is derived and used to smooth out the points. The filter returns a value at the center of the smoothed out points of the subset. The interpolated values for the resolution are used for the rest of the analysis and they are listed in table 6.6.

| m_a [MeV/c ²] | σ_{peak} [MeV/c ²] | m_a [MeV/c ²] | σ_{peak} [MeV/c ²] |
|-----------------------------|---------------------------------------|-----------------------------|---------------------------------------|
| 15 | 3.87 | 24 | 4.31 |
| 17 | 3.66 | 25 | 4.22 |
| 20 | 3.81 | 26 | 4.14 |
| 21 | 4.00 | 27 | 4.13 |
| 22 | 4.07 | 28 | 4.31 |
| 23 | 4.09 | 29 | 4.11 |
| | | 30 | 4.17 |

Table 6.5: For each mass m_a the resulting σ_{peak} resolution on the mass peak calculated as in equation 6.8

| m_a [MeV/c ²] | σ_{peak} [MeV/c ²] | m_a [MeV/c ²] | σ_{peak} [MeV/c ²] |
|-----------------------------|---------------------------------------|-----------------------------|---------------------------------------|
| 15 | 3.78 | 24 | 4.21 |
| 17 | 3.79 | 25 | 4.20 |
| 20 | 3.84 | 26 | 4.22 |
| 21 | 3.91 | 27 | 4.17 |
| 22 | 4.07 | 28 | 4.16 |
| 23 | 4.17 | 29 | 4.16 |
| | | 30 | 4.17 |

Table 6.6: Values for the resolution σ_{peak} after the use of the Savitzky–Golay filter.

The resolution on each mass peak is now defined. The region for sensitivity study is given by $m_{e^+e^-} \pm n \cdot \sigma_{peak}$, where n is an integer or fractional number. The value of n has been varied in order to compare the final sensitivity results in different regions of the invariant e^+e^- mass. The procedure to obtain the sensitivity, which is object of the following sections, has been used in the same way in the different $m_{e^+e^-} \pm n \cdot \sigma_{peak}$ regions, varying n from 0.5 to 2.5. The region in which the sensitivity has the lowest value is in the $m_{e^+e^-} \pm 1 \cdot \sigma_{peak}$ one. As discussed in section 6.5 and shown in figure 6.13. In table 6.7 the mass window $m_{e^+e^-} \pm 1 \cdot \sigma_{peak}$ for each generated mass in which sensitivity is optimized.

| m_a [MeV/c ²] | $m_a \pm 1 \cdot \sigma_{peak}$ [MeV/c ²] | m_a [MeV/c ²] | $m_a \pm 1 \cdot \sigma_{peak}$ [MeV/c ²] |
|-----------------------------|---|-----------------------------|---|
| 15 | [11.19; 18.81] | 24 | [19.80; 28.20] |
| 17 | [13.18; 20.82] | 25 | [20.83; 29.17] |
| 20 | [16.15; 23.85] | 26 | [21.82; 30.18] |
| 21 | [17.08; 24.92] | 27 | [22.86; 31.14] |
| 22 | [17.92; 26.08] | 28 | [23.86; 32.14] |
| 23 | [18.82; 27.18] | 29 | [24.84; 33.16] |
| | | 30 | [25.80; 34.20] |

Table 6.7: For each mass m_a the resulting $\pm 1 \cdot \sigma_{peak}$ mass window is given. Each value of σ_{peak} is taken from table 6.6.

6.5 Radial vertex distribution

As seen in figure 6.4, the most important background contribution is the one coming from $\gamma\gamma$ background process. In the region $m_a \pm 1 \cdot \sigma_{peak}$, the number of events of $\gamma\gamma$ background is of order 10^5 events.

The photons convert in the detector material, where the first material layer is at 1 cm from the interaction point. The axion has a decay time of $\tau \sim 10^{-15}$ s so the decay length is $l = \tau\beta\gamma \sim 100$ nm. Due to this difference, a variable useful for discrimination is the coordinate of the reconstructed vertex of the electron and positron pair which should coincide with the IP for the signal.

In the Belle II detector, the coordinate system is shown in figure 6.7

The variable R is defined as:

$$R = \sqrt{x^2 + y^2} \quad (6.9)$$

where x and y are the distance from the IP, respectively on the x and y axis, of the reconstructed vertex of the final state electron and positron.

The R distribution for the signal for three different m_a values are in figure 6.8. The distribution shows the expected form: it peaks near zero and it is almost all concentrated in the region $R < 1$ cm, which is inside the beam pipe.

The distribution tends to be narrower for higher values of m_a , and fewer points are distributed for R values greater than 1 cm. Also, the bump present at $R \sim 1.4$ cm, visible in all three images, becomes smaller when m_a increases. The coordinate $R = 1.4$ cm corresponds to the coordinate of the first PXD layer, in which the photons convert. The bump is due to a bad reconstruction in the signal events, where an axion is instead reconstructed as a photon. The effect is increasingly worst for smaller mass values, for which the mass is closer to $m_a \sim m_\gamma$.

The figure 6.9 shows the same distribution for the background events. The distribution is flat up to $R = 1.4$ cm. In the first PXD layer the majority of the photons

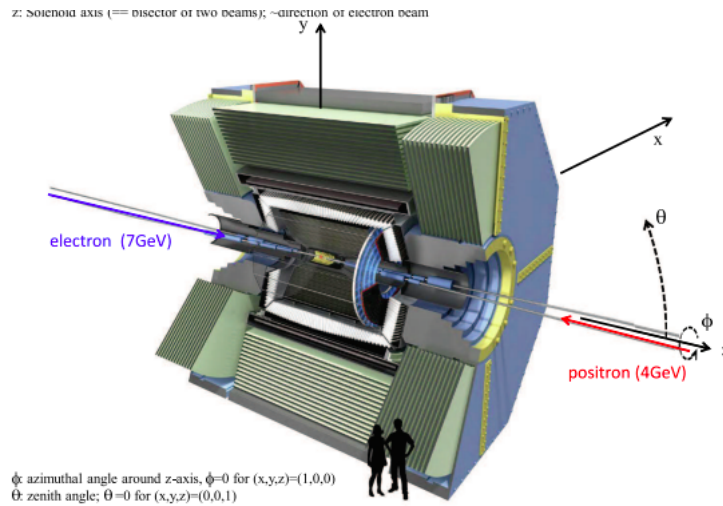


Figure 6.7: Coordinate system chosen for the Belle II detector. The z axis is along the beam, and points forward; direction which is chosen on the basis of the boost in the center of mass frame. The y axis point upward, the x axis point out. The IP is taken to be at $x = y = z = 0$. The two angular coordinates are: θ as the polar angle, defined as $\theta = 0$ when the coordinates are $(0,0,1)$, and ϕ the azimuthal angle, defined as $\phi = 0$ when the coordinates are $(1,0,0)$.

produce e^+e^- pairs. At 2.2cm the second PXD layer, and at 3.9cm the first SVD layer, in which the remaining photons convert.

A cut on the R value can be used as a selection criteria on the signal events, so to reject the background.

Comparing the distributions in figure 6.8 and 6.9 the cut should be at least $R < 1$ cm.

The value of the chosen cut will affect the efficiency and the purity of the signal. The efficiency is defined as the ratio between the number of events (total events) passing the selection criteria vs the generated number of signal events. The purity is defined as the ratio between the number of signal events passing the selection criteria vs the number of events passing the selection criteria.

A loose cut (the selection criteria) will give a high efficiency value because less events are eliminated. On the other hand, a stringent cut will eliminate most of the events, but the ones passing the selection will have a high purity, because most of the background is eliminated.

In an analysis the goal for the cut is to be able to keep a good purity and a good efficiency at the same time. In a purity vs efficiency plot this is seen as the most distant point from the origin. An example of purity vs efficiency plot is given in figure 6.10

To pick the optimal value of a selection criteria on a variable there are different statistical tools. In this case, in order to optimize the cut on the R , I have performed the maximization of the Punzi figure of merit, which is briefly discussed in the next

Radial vertex distribution, signal

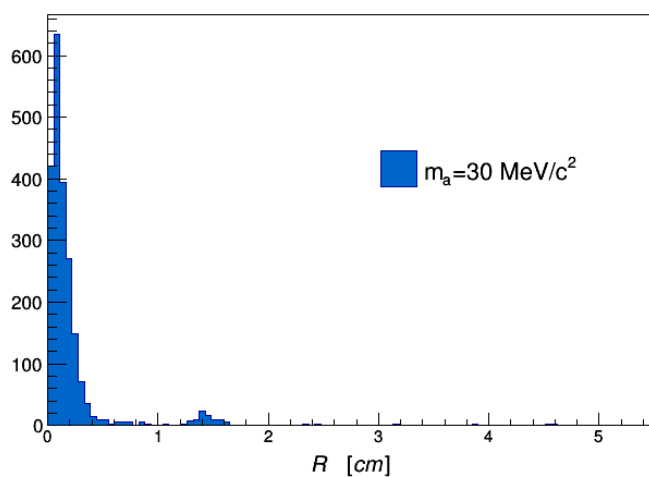
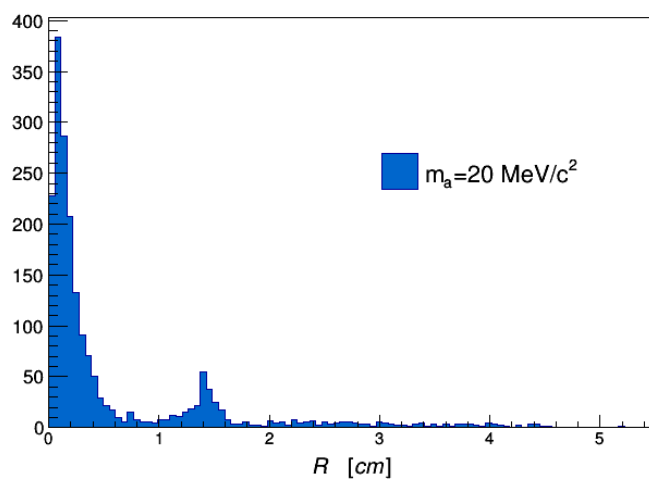
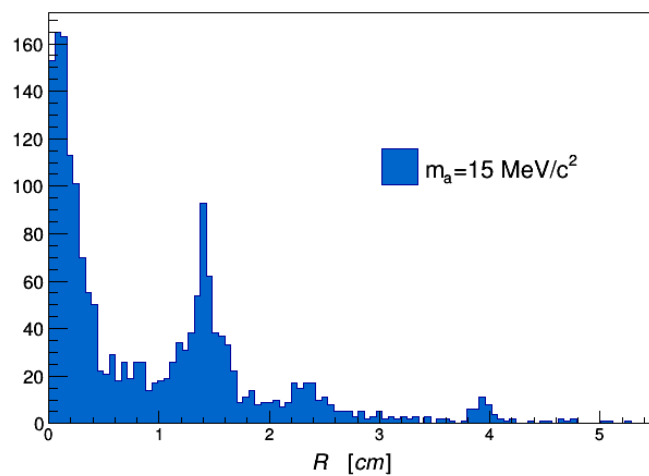


Figure 6.8: The distribution of $R = \sqrt{x^2 + y^2}$ for three different generated mass values: $m_a = 15 \text{ MeV}/c^2$ (top), $m_a = 20 \text{ MeV}/c^2$ (center) and $m_a = 30 \text{ MeV}/c^2$ (bottom).

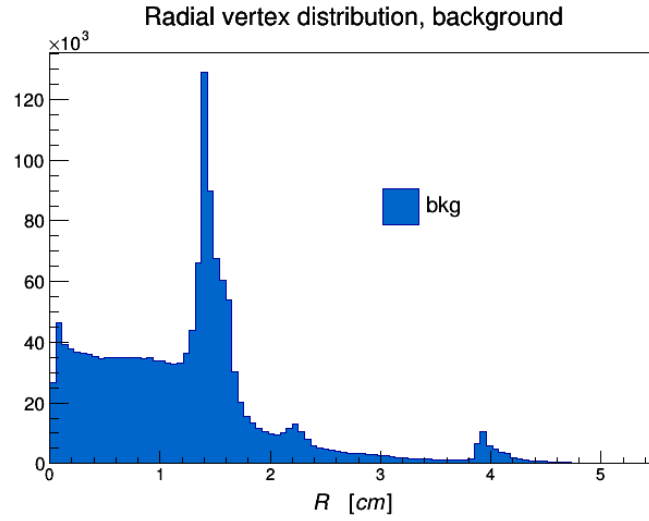


Figure 6.9: Distribution of $R = \sqrt{x^2 + y^2}$ for the background events. The background, for the considered mass regions, is mainly given by $\gamma\gamma$ events (see figure 6.4).

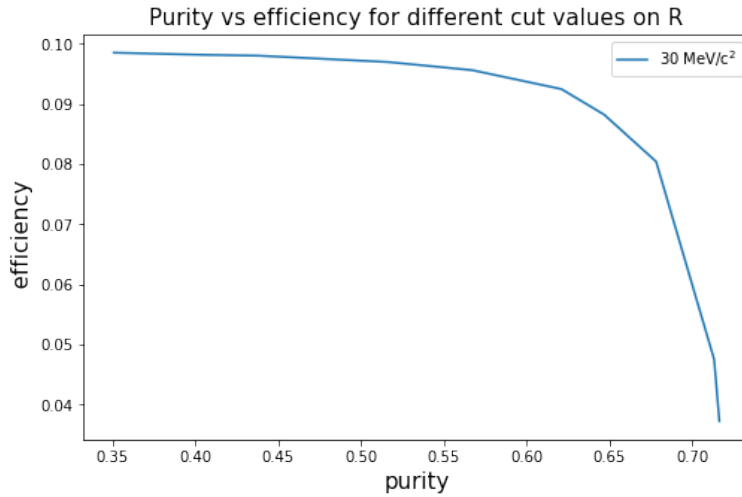


Figure 6.10: On example plot of purity vs efficiency, for the mass $m_a = 30\text{MeV}/c^2$. Each point of the line is given for a different choice of cut on the R variable. For very loose cuts the efficiency is at the highest value, while purity is much smaller. Requiring a more stringent cut means moving along the line to the right, so for a more stringent cut on R the purity is $\sim 75\%$ while the efficiency is lost. The ideal value of the cut on R should be on the round corner of the line, where both efficiency and purity have high values. In the case of $m_a = 30\text{MeV}/c^2$ the plot was made with a cut in the range $0.08 \div 1\text{ cm}$

section, for each value of m_a . The obtained values for the cut on R correspond to the values giving the points on the curve in the purity vs efficiency plot.

Figure of Merit

In general, the search for phenomena described by new physics is a test of hypothesis. The question is whether a default hypothesis H_0 or a new hypothesis H_m better describe a certain observable. The m subscript stands for a generic number of parameters in the new hypothesis. In the case considered, the observable can be the number of observed signal events: the H_0 is the Standard Model description, which would count zero signal events and only background events; while H_m is the model described in chapter 3, where the number of signal events differs from zero.

When comparing two hypothesis, one has to define a *significance level* usually indicated with α , which gives the probability of rejecting H_0 in the eventuality of it being the true hypothesis. Assuming instead H_m as true hypothesis, the probability of rejecting the right hypothesis is indicated as $\beta(m)$.

The way to express the probability of a new discovery is through the *power* of the test defined as $1 - \beta(m)$. It gives the probability of the observable being correctly described by H_m as a function of the parameters m .

Through the definition of *power* one can define a *sensitivity* region as:

$$1 - \beta_\alpha(m) > CL \quad (6.10)$$

where CL is the *confidence level* defined as $1 - \alpha$. This is the region in the parameter space m at which the experiment is sensitive, because it can give information on the hypothesis in any case: if m satisfies the condition, there is at least probability CL of having the discovery; if m instead does not satisfy the condition, the results will exclude all the region defined in equation 6.10.

The problem dealt with in this thesis is a counting experiment in presence of background. The sensitivity region as defined in equation 6.10 does not depend on the expected number of counts, and its optimization can be achieved through the maximization of a specific *figure of merit* after some assumptions [64] :

$$\frac{\varepsilon(t)}{\frac{a}{2} + \sqrt{B(t)}} \quad (6.11)$$

where B indicates the number of background events, a corresponds to the number of sigmas in a Gaussian test with significance α , ε is the signal efficiency and the letter t indicates a set of cuts imposed. For a one-tailed test and $\alpha = 0.1$ the number a is $a = 1.28$. The *Punzi figure of merit* in equation 6.11 is fitting for this type of analysis because it only depends on the efficiency of the signal events, not the number of signal events as in other *figure of merit*, which would require the knowledge of the cross section of the process.

The maximization is made in the following way. The values of the cut on R are chosen in a range from $[R_{min}, R_{max}]$ and subdivided by n steps. For each value, the constraint $\sqrt{x^2 + y^2} < R$ is imposed, and the number of $\varepsilon(t)$ and $\sqrt{B(t)}$ calculated.

The operation is repeated for n times, in which the R value is increased by $(R_{max} - R_{min})/n$. The R which maximises the ratio between efficiency and background events is the best cut for R value. An example of maximization of equation 6.11 is in figure 6.11.

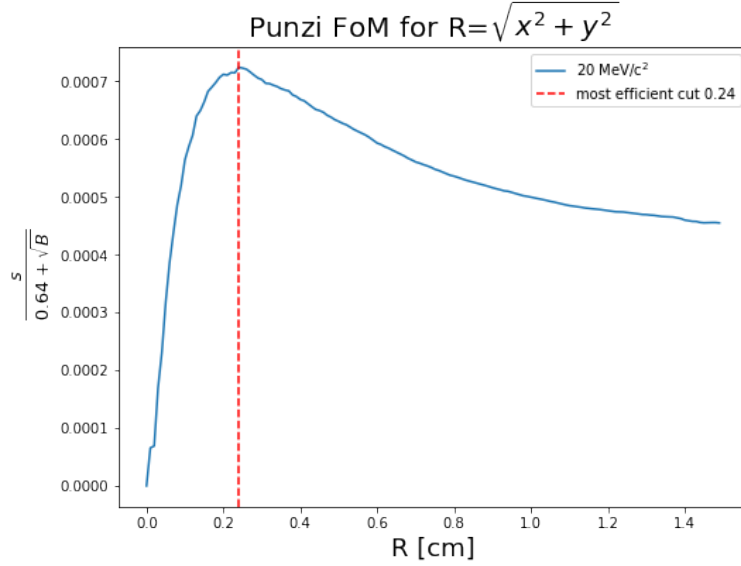


Figure 6.11: Example of maximization of the Punzi figure of merit for an example mass $m_a = 20 \text{ MeV}/c^2$. Each point on the blue line represents the ratio between the signal S and the square root of the background events B for the corresponding value of R . The red dotted line indicates for which cut on the variable R the ratio is maximized.

The values of the cut on R found by maximization of the *figure of merit* are listed table 6.8. The best cut value on R is then used as selection criteria on signal events. The signal efficiency and the number of background events after the selection is applied are displayed in figure 6.12.

| m_a [MeV/ c^2] | cut on R [cm] | m_a [MeV/ c^2] | cut on R [cm] |
|---------------------|-----------------|---------------------|-----------------|
| 15 | 0.28 | 24 | 0.22 |
| 17 | 0.22 | 25 | 0.23 |
| 20 | 0.24 | 26 | 0.22 |
| 21 | 0.22 | 27 | 0.20 |
| 22 | 0.22 | 18 | 0.22 |
| 23 | 0.25 | 29 | 0.21 |
| | | 30 | 0.21 |

Table 6.8: Values of the cut on the R variable for each generated mass m_a . The values result from the maximization of the *figure of merit* in equation 6.11. Such cut values allow to maximize the ratio of signal vs background in the R distribution.

The cut values tend to be more stringent for higher m_a values. This can be expected because, as shown in image 6.8, higher m_a values show an R distribution more narrow and peaked around small values of R. Furthermore, the number of background events is smaller for higher m_a values, as seen in figure 6.12, a trend expected from the $\gamma\gamma$ background.

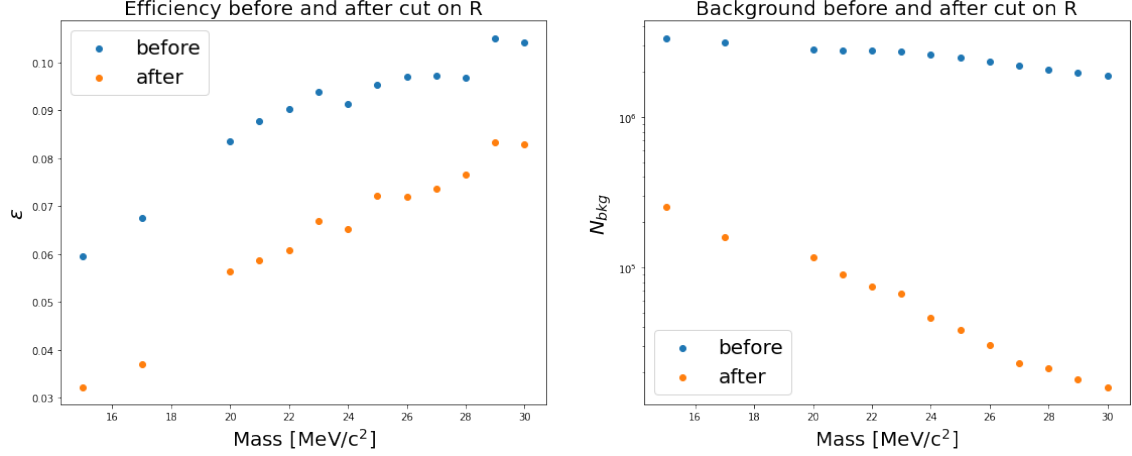


Figure 6.12: Plot of signal efficiency and number of background events before and after implementing the cut on R. The selection criteria rejects at least 90% of the background events. Both efficiency and background events (before and after the cut on R) are calculated in the $m_a \pm 1 \cdot \sigma_{peak}$ region.

The cut on the variable is able to reject at least $\sim 90\%$ of the background. The efficiency of the signal is also reduced, more for lower m_a values, but nevertheless the sensitivity on the cross section will improve, as shown later.

6.6 Sensitivity estimation

The sensitivity on the cross section in equation 6.3 is obtained as the sensitivity in a cut and count experiment in which one would expect only background events. For a large number of events, the distribution of the background can be considered Gaussian. For a Gaussian distribution, a test with a CL=90% corresponds to 1.28 as number of sigmas. Thus the number of background events are expected to be $1.28 \cdot \sqrt{B}$ and the sensitivity on the cross section at 90%CL, and not considering systematic errors, is given by:

$$\sigma_{90\%CL} = \frac{1.28 \cdot \sqrt{B}}{L \cdot \epsilon} \quad (6.12)$$

where L is the integrated luminosity and ϵ the efficiency on signal events.

The quantity in equation 6.12 is model dependent : the efficiency on the signal events change according to the allowed final states through which the model can be

probed, and this has an effect also on the resolution used to select the mass window. The used strategy is general, but the results rely on the specific model.

As said, the operations necessary to calculate the sensitivity have been made in different mass windows, in order to find the region which optimize the sensitivity. The plot in figure 6.13 shows the sensitivities calculated in different mass windows. The region $m_a \pm 1 \cdot \sigma_{peak}$ is the one maximizing the sensitivity, and the one in which the previous analysis have been made.

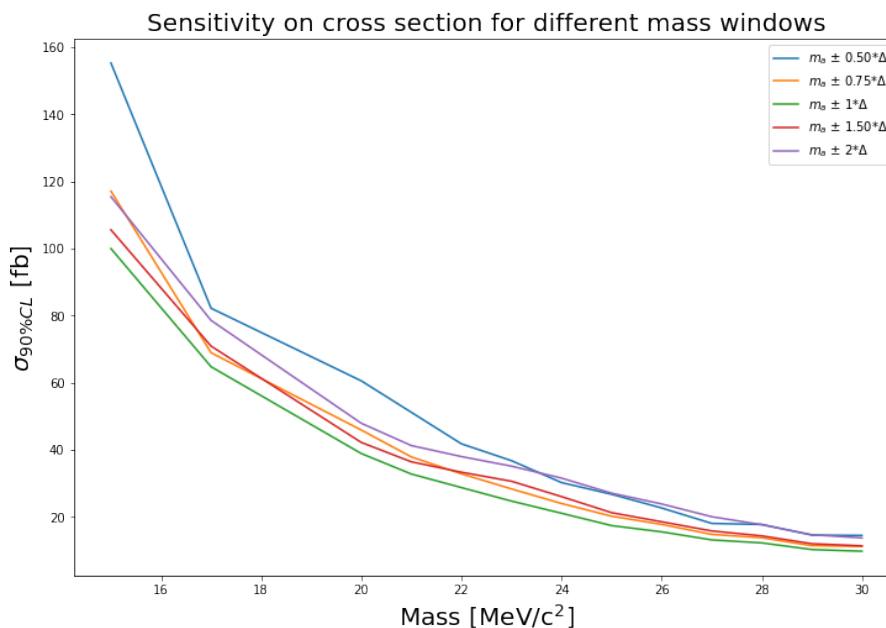


Figure 6.13: Different sensitivities on the production cross section at 90 % CL due to the choice of different mass windows. Different colors indicate different regions, as indicated in the legend. The region which gives the lowest sensitivity is the $m_a \pm 1 \cdot \sigma_{peak}$ region.

In figure 6.14 the sensitivity is shown before and after implementing the selection criteria on R. The sensitivity on the cross section has the expected trend. For lower m_a values, the background component is higher and the signal efficiency is worse, thus the $\sigma_{90\%CL}$ value is higher. The selection criteria effects the signal efficiency more or less in the same way for all m_a values (see figure 6.12); also the number of background events vary in the same way. This explains why the $\sigma_{90\%CL}$ after the selection keeps the same shape as before the selection is applied.

6.7 Recast on coupling parameters

The production cross section for the $e^+e^- \rightarrow \gamma a$ in equation 6.3 is here reported:

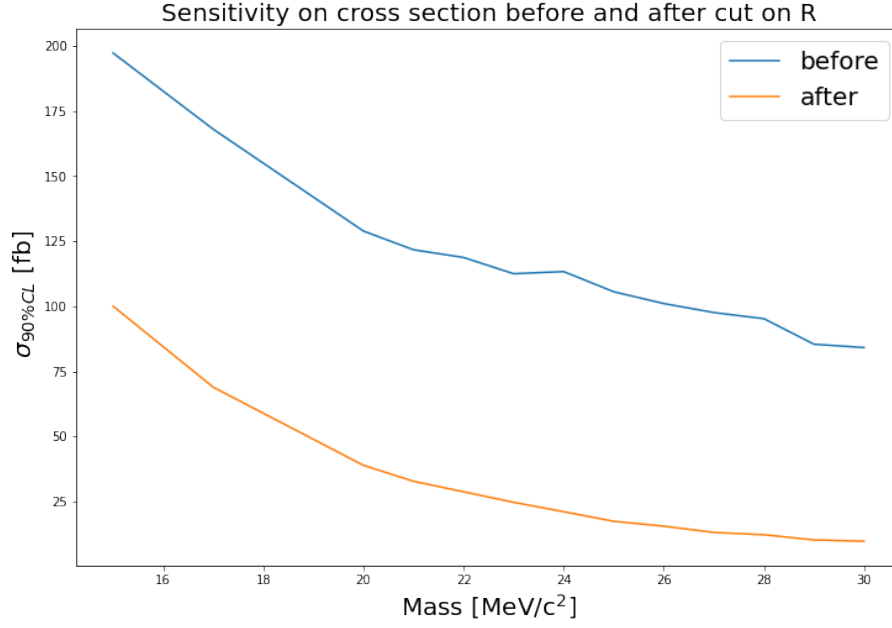


Figure 6.14: Sensitivity on the production cross section at 90 % CL before and after using the cut on R as selection criteria on the events.

$$\sigma_{e^+e^- \rightarrow \gamma a} = \frac{4\alpha}{\sqrt{s}} \left(\frac{Q_e}{f_a} m_e \right)^2 \frac{1}{1 - \cos^2 \theta_\gamma + \left(\frac{4m_e^2}{s} \right) \cos^2 \theta_\gamma} \Bigg|_{\theta_\gamma^1}^{\theta_\gamma^2} \quad (6.13)$$

The cross section is proportional to the square of the coupling parameter Q_e/f_a between axion and electrons.

The sensitivity estimation found in the previous section gives a value $\sigma_{90\%CL}$ which can be used as a measured quantity. As well as the theoretical cross section in the above equation, also $\sigma_{90\%CL}$ is proportional to the square of the coupling parameter. Exploiting the ratio between σ and $\sigma_{90\%CL}$ it is possible to obtain the upper limit at 90% CL for the coupling parameter $(Q_e/f_a)_{90\%CL}$:

$$\left(\frac{Q_e}{f_a} \right)_{90\%CL} = \frac{Q_e}{f_a} \cdot \sqrt{\frac{\sigma_{90\%CL}}{\sigma}} \quad (6.14)$$

The σ has been calculated for each m_a value and it is plotted in figure 6.15. For the axion model, the energy scale f_a and mass m_a are related as in equation 1.42, so the cross section grows increases with the mass m_a .

The expression in 6.14 expects an initial value for the coupling parameter of the model. As initial value I have taken $Q_e/f_a = 1 \text{ GeV}^{-1}$ which enables the axion to be fairly coupled with the electron and also is the value right below the exclusion upper limits imposed by Babar and KLOE collaboration. With this initial condition, the values of the sensitivity on the $(Q_e/f_a)_{90\%CL}$ are listed in table 6.7

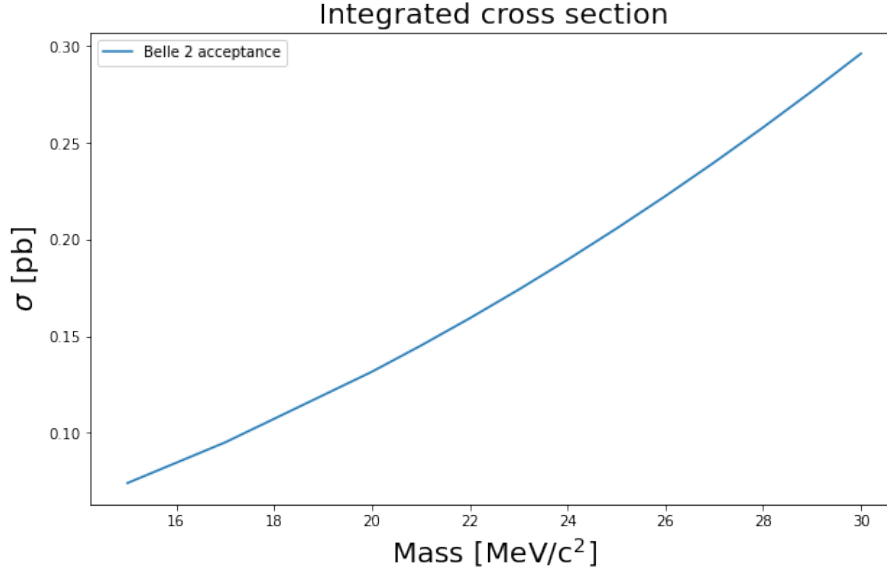


Figure 6.15: Value of the integrated cross section for every mass value. The angles of Belle II acceptance are $\theta \in [16^\circ \div 150^\circ]$. The cross section shows an increasing trend with the mass m_a , compatible with the proportionality between the two quantities: $\sigma \propto m_a^2$

| m_a [MeV/c ²] | Q_e/f_a [GeV ⁻¹] | m_a [MeV/c ²] | Q_e/f_a [GeV ⁻¹] |
|-----------------------------|--------------------------------|-----------------------------|--------------------------------|
| 15 | 3.05 | 24 | 1.40 |
| 17 | 2.46 | 25 | 1.27 |
| 20 | 1.90 | 26 | 1.20 |
| 21 | 1.75 | 27 | 1.10 |
| 22 | 1.64 | 28 | 1.07 |
| 23 | 1.52 | 29 | 0.98 |
| | | 30 | 0.95 |

Table 6.9: For each mass value, the recast of the sensitivity on the coupling parameters obtained by the equation in 6.14.

The analysis was made with an integrated luminosity $L = 200 \text{ fb}^{-1}$. A preliminary recast on a higher luminosity can be made knowing how it scales with luminosity. The sensitivity on the cross section scales as $\sigma|_{90\%CL} \sim \sqrt{L}$, so the coupling parameter scales as $\frac{Q_e}{f_a} \sim L$. Recasting to a different luminosity means multiplying the obtained values for the ratio of the different luminosity value. The other luminosity was chosen at $L = 400 \text{ fb}^{-1}$, which is approximately the current integrated luminosity.

The obtained results are compared to the ones obtained by KLOE and Babar from the recast of the search of dark photon.

6.7.1 Dark photon search and recast

The parameter space in figure 3.1 shows the shaded exclusion areas given by KLOE and Babar search for a dark photon. The experiments are both precision colliders experiments, so they share a lot of the advantages of precision colliders already cited. The respective detectors and analysis are summarize.

KLOE

The KLOE experiment was operative at the DAΦNE collider, in which electron and positron beams circulate and collide at a center of mass energy of $\sqrt{s} = 1.0195 \text{ GeV}$, the mass of the ϕ meson.

The KLOE detector is composed by a drift chamber (DC) surrounded by an electromagnetic calorimeter (ECL) covering almost 98% of the total solid angle. A superconducting coil around the ECL produces a magnetic field used to determine the charge of the particle. The energy deposition in the ECL and the number of hits in the DC are used as trigger signal.

The search for a dark photon was done in the channel $e^+e^- \rightarrow \gamma A'$ followed by the decay of the dark photon into electron and positron $A' \rightarrow e^+e^-$ [65]. The dark photon should appear as a peak in the invariant mass of the final e^+e^- . The irreducible background is the Bhabha scattering; the reducible backgrounds are $e^+e^- \rightarrow 2\gamma, 2\mu$ and decays of the ϕ . The study was made with a luminosity $L = 1.54 \text{ fb}^{-1}$. Events were selected by requiring: three separated energy deposit in the ECL; an emission angle for all final particles of $55^\circ < \theta < 125^\circ$ to suppress the contribution of Bhabha background; a cut on the photon energy $E_\gamma > 305 \text{ MeV}$. The studied invariant mass took values in the range $m_{ee} \ 5 < m_{ee} < 100 \text{ MeV}/c^2$, with a resolution peak $1.4 \text{ MeV}/c^2 < \sigma_{res} < 1.7 \text{ MeV}/c^2$. In this region the signal efficiency resulted $\varepsilon \sim 0.01 \div 0.02$.

An upper limit at 90% CL on the number of signal events N was calculated. This was used for an upper limit evaluation on the production cross section σ and the $A' - \gamma$ mixing parameter $\varepsilon_{A'\gamma}^2$. The results gave $\varepsilon_{A'\gamma}^2 \sim 10^{-6}$ for the m_{ee} mass range.

BaBar

Babar was an experiment at the SLAC PIP-II accelerator, in which electrons and positrons collide at a center of mass energy $\sqrt{s} = 10.58 \text{ GeV}$

The detector has the main characteristics of a *b-factory* listed in chapter 5. It is composed by 5 sub-detectors: the Silicon Vertex Tracker (SVT) used to determine the position of the charged tracks; the drift chamber (DCH); the detector of internally reflected cerenkov radiation (DIRC); the electromagnetic calorimeter (ECL) and the instrumented flux return which identifies muons and neutral hadrons. Also Babar has a magnetic field for the charge determination. The collaboration tested the dark photon

hypothesis through the study of the $e^+e^- \rightarrow \gamma A'$ at a luminosity $L = 514 \text{ fb}^{-1}$ [62]. The invariant mass considered was $0.02 \text{ GeV}/c^2 < m_{ee} < 10.2 \text{ GeV}/c^2$. The background are the same as in the KLOE analysis.

The selection was made by requiring: two opposite charged tracks and a single photon in the final state; a total center of mass energy $E^* > 0.02 \text{ GeV}$; the cosine of the emission angle $\cos\theta > -0.5$ to eliminate Bhabha background.

The mass resolution resulted $1.5 \text{ MeV}/c^2 < \sigma_{res} < 8 \text{ MeV}/c^2$, and the selection efficiency $\varepsilon \sim 15\%$.

The cross section is obtained again as the ratio between the signal yield and the product between the luminosity and the signal efficiency. The 90% CL upper limits were calculated through a Bayesian approach, with a flat prior for the cross section. The upper limit on the cross section is $\sigma(e^+e^- \rightarrow A'\gamma) \sim 25 \text{ fb}$, which results in an upper limit for the mixing parameter $\varepsilon_{A'\gamma} \sim 10^{-4} \div 10^{-3}$.

Recast

The dark photon is a new particle arising in BSM theories. This new boson has a mixing term with the electron field, through a mixing parameter ε . The final state is the same as the one of the axion channel, for this the recast is made by equating the integrated cross sections of the two process. The differential production cross section, as written in [66], is given by:

$$\frac{d\sigma_{e^+e^- \rightarrow \gamma A'}}{d\cos\theta_\gamma} = 2\pi\alpha^2\varepsilon^2 \frac{(s + m_{A'}^2)^2 + (s - m_{A'}^2)^2 \cos^2\theta}{s(s - m_{A'}^2)(s \cdot \sin^2\theta + 4m_e^2)} \quad (6.15)$$

where $\alpha = 1/137$ is the electromagnetic constant. The integration in the KLOE and Babar angles give a linear dependence between the square power of ε^2 and $(Q_e/f_a)^2$, thus the limits on the first can be recast on the second one.

The comparison is in figure 6.16

The recast made is a preliminary one, it does not keep in account the trigger efficiency nor systematic errors. Nonetheless it is to note that it lowers the previous bound coming from Babar in the region of $[25 - 30 \text{ MeV}/c^2]$.

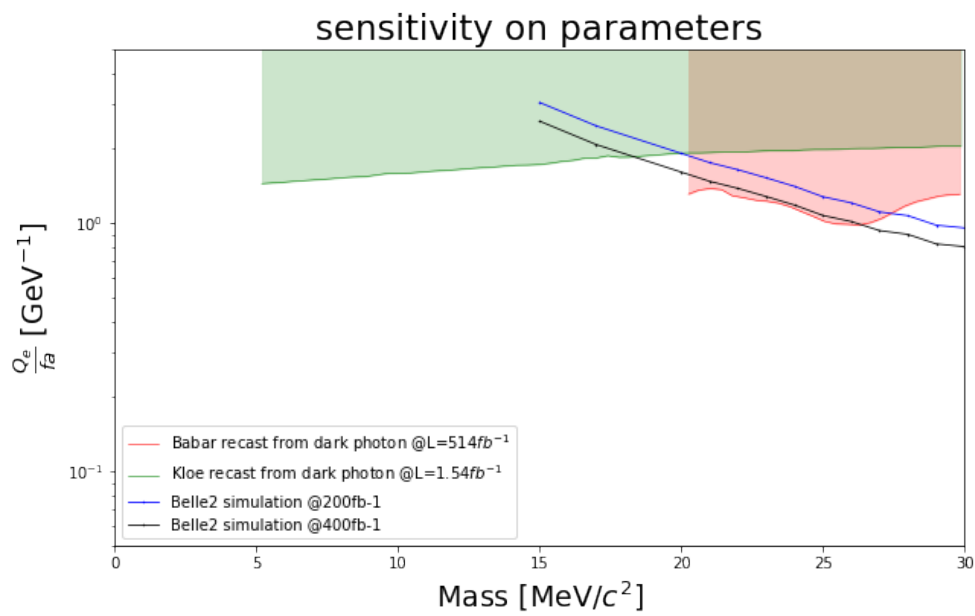


Figure 6.16: Comparison between the recast limits on the Q_e/f_a from KLOE and Babar and the recast obtained by the Belle 2 simulation for two interesting values of luminosity.

7. Study on $\tau \rightarrow l \alpha$

In this chapter I briefly go over the study conducted by the Belle II collaboration on the lepton flavor violating channel $\tau \rightarrow l \alpha$ where l is a lighter lepton and α is an invisible particle.

In colliders such as Belle II tau particles are produced in $\tau\bar{\tau}$ pairs, and both are used for the analysis. One is the *signal* tau, which decays in the channel of interest; the other is the *tag* tau, which has a signature decay in SM particles used to check if the signal comes from a τ pair event.

7.1 Belle II study

As stated earlier, Belle II can be seen also as a muon or a tau factory, because of the relatively high production cross section in table 5.1. The τ particles can be useful for studies of new physics process involving leptons, the most important being lepton flavor violating decays. The Belle II clean work environment is useful to investigate channels with invisible energy in the final state, due to the presence of one or more photons or neutrinos. This makes Belle II a good detector in which to test the $\tau \rightarrow l \alpha$. The study is conducted in a model independent way, it just aims to give a new upper limit on the branching fraction of the process and lower the existing one put by ARGUS [67].

The study conducted on the data is currently in review. The results here reported come from a preliminary study on MC simulations with a luminosity of $L = 63 \text{ fb}^{-1}$. The process is given in figure 7.1

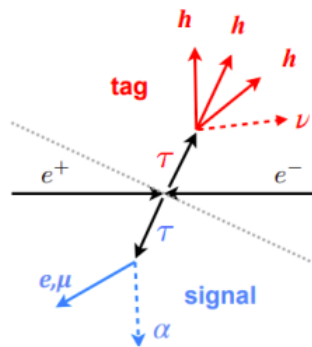


Figure 7.1: Diagram of studied process. Tag side is 3prong, signal side includes a lepton and an invisible particle.

Both τ and $\bar{\tau}$ are used in the reconstruction of the event. The *signal* side is a $\tau \rightarrow$

$e/\mu + \alpha$ with α invisible and long lived particle; the *tag* one is a decay in $\tau \rightarrow \pi\pi\pi\nu_\tau$ which has Branching ratio $Br = 9.31 \pm 0.05$ [1]. The choice of the final state particles entering the *tag* side is made to reduce the background. The *signal* side containing exactly one visible track is called *1prong*, while the *tag* side is called *3prong*. The *1prong* decays represent the $\sim 85\%$ of τ decay modes, while the *3prong* decays make up the $\sim 15\%$ of the decay modes.

The study uses seven different mass values for α in the range of $0.5 \div 1.6 \text{ GeV}/c^2$. The two hemispheres containing the taus are separated by the thrust vector, which is defined as the vector maximizing the momentum projection on a given direction :

$$\hat{T} = \max_n \left(\frac{\sum |\vec{p}_i^{CM} \cdot \hat{n}_{thrust}|}{\sum |\vec{p}_i^{CM}|} \right) \quad (7.1)$$

with \vec{p}_i^{CM} is the momentum in the center of mass frame of each final state particle in the event and \hat{n}_{thrust} is the *thrust* versor, which is the main axes of the event.

The reconstruction is made by requiring exactly four charged tracks in final state, and by the optimization of the thrust vector. The background for this study is given by $\tau \rightarrow e\nu\nu, B\bar{B}, q\bar{q}, \mu\mu(\gamma)$ and $ee(\gamma)$. Suppression of background is made with requests:

- visible energy in CM frame : $2.0 < E_{vis}^{CM} < 9.9 \text{ GeV}$
- thrust vector : $0.8 < \hat{T} < 0.99$ to reject spherical events ($\hat{T} < 0.5$).
- invariant mass of 3-prong in tag side : $0.48 < M_{3\pi} < 1.66 \text{ GeV}/c^2$

The signal event is given by two final particles, which in the CM frame would be easily recognized thanks to their monochromatic energy. But because of the τ boost, the electrons energy is a spectrum and not a single peak. To evaluate the electrons energy in the laboratory system it is necessary to make a boost in the τ frame. This would require the flight direction of such particle, which can not be reconstructed because of the presence of an invisible track in the final state.

One way to evade the problem is to approximate the τ momentum and use this value to boost into a pseudo-rest frame. There are two possibilities to approximate the direction of the tau momentum \vec{p}_τ in the center of mass frame. A first possibility is to consider the momentum of the tag side approximately equal to the momentum vector of the three final pions. In this way:

$$\hat{p}_{sig}^{CM} = -\hat{p}_{tag}^{CM} \sim \frac{\vec{p}_{3\pi}}{|\vec{p}_{3\pi}|} \quad (7.2)$$

This is the choice made by the ARGUS collaboration while studying the same process.

Otherwise, an other way is to use the thrust vector:

$$\hat{p}_{sig} = \hat{n}_{thrust} \quad (7.3)$$

In the Belle II studies both methods are used and compared. The choice of \hat{p}_τ sets the frame in which to apply cuts and give the upper limit on the branching fraction.

The formula used to describe the data F, including both signal and background, is:

$$F = \frac{\varepsilon_{l\alpha}}{\varepsilon_{lvv}} N_{lvv} \frac{Br(\tau \rightarrow \alpha l)}{Br(\tau \rightarrow lvv)} + N_{lvv} f_{lvv} + N_{bkg} f_{bkg} \quad (7.4)$$

In the formula, N_i represent the number of background events, where the irreducible background has been made explicit: N_{lvv} . The parameters f_i are probability density functions extracted from Monte Carlo simulations. Using N_i and $R = Br(\tau \rightarrow \alpha l)/Br(\tau \rightarrow lvv)$ as free parameters, a fit on the formula can give an upper limit on R with a 95%CL.

The resulting upper limit on $Br(\tau \rightarrow e\alpha)/Br(\tau \rightarrow evv)$ is of order 10^{-3} for $m_\alpha \in [0.5, 1.4] \text{ GeV}/c^2$ and of order 10^{-4} for $m_\alpha = 1.6 \text{ GeV}/c^2$. The new upper limits are of one order of magnitude lower than the ones put from ARGUS.

7.2 Recast of the limit

The question is whether the new limits on the branching ratio can be used in the model of an invisible and long lived ALP discussed in chapter 4, because the channel $\tau \rightarrow l\alpha$ represent exactly the type of decay which produced ALP as DM particle.

For the tau to electron case, the coupling matrix present mixing in the first and third generation: C_{ij}^V, C_{ij}^A are:

$$C_{ij}^V = C_{ij}^A = \begin{pmatrix} \sin(\varepsilon) & 0 & \cos(\varepsilon) \\ 0 & 0 & 0 \\ \cos\varepsilon & 0 & -\sin(\varepsilon) \end{pmatrix} \quad (7.5)$$

for the tau to muon instead: C_{ij}^V, C_{ij}^A are:

$$C_{ij}^V = C_{ij}^A = \begin{pmatrix} 0 & 0 & 0 \\ 0 & \sin(\varepsilon) & \cos(\varepsilon) \\ 0 & \cos(\varepsilon) & -\sin\varepsilon \end{pmatrix} \quad (7.6)$$

In the model the flavor violating decay of a tau in a generic lepton and ALP particle is:

$$\Gamma(\tau \rightarrow \alpha l) = \frac{\cos^2\varepsilon}{\Lambda_a^2} \frac{m_\tau^3}{32\pi} \left(1 - \frac{m_\alpha^2}{m_\tau^2}\right)^2 \quad (7.7)$$

up to corrections m_l^2/m_τ^2 , where Λ_a represents the energy scale at which the global symmetry $U(1)$ is broken.

The model works for DM candidates which are sufficiently long lived, hence light in order to suppress as much as possible the number of kinematic allowed channels.

But for extremely light particles there can be constraint coming from cosmological observations. The DM particles produced via decay of standard model leptons have an initial kinetic energy depending on the mass of the particle itself and the one of the decaying lepton. The higher the initial decaying mass and the lower the DM mass, the *warmer* the DM particle will be. Once it is produced, the dark matter particle streams in the universe, and if its kinetic energy is too high it might be in conflict with cosmological structure formation. For this, there reason is a lower bound on the mass value given by [49] which leads to $m_\alpha > 1 \text{ keV}$.

In the freeze-in mechanism, the request of a candidate fully covering the measured relic dark matter abundance gives:

$$\frac{\Lambda}{\cos\varepsilon} = 4.9 \cdot 10^9 \sqrt{\frac{m_\alpha}{100 \text{ keV}}} \sqrt{\frac{m_\tau}{\text{GeV}}} \quad (7.8)$$

meaning that the model of an ALP candidate as DM produced via the freeze in mechanism of lepton flavor violating decays foresees an energy scale of the order 10^9 GeV . As said in chapter 4, the value of ε for the interesting regions remains in the $10^{-1} \div 10^{-3}$ region, so the quantity $\cos(\varepsilon) \sim 1$.

The limit on the branching ratio given by Belle II is then a limit on $\Gamma(\tau \rightarrow e\alpha)$ as :

$$\Gamma(\tau \rightarrow e\alpha) < \frac{Br(\tau \rightarrow e\alpha)}{Br(\tau \rightarrow e\nu\nu)} \Gamma(\tau \rightarrow e\nu\nu) \quad (7.9)$$

where the total decay width $\Gamma(\tau)$ in the new model is taken equal to the one predicted by SM because the new decays $\tau \rightarrow \mu\alpha$ and $\tau \rightarrow e\alpha$ have small decay widths.

By making explicit the dependence of $\Gamma(\tau \rightarrow l\alpha)$ as in equation 7.7, from the coupling parameters $\Lambda/\cos(\varepsilon)$ the limit can be converted into a lower bound

$$\frac{\Lambda}{\cos(\varepsilon)} > \sqrt{\frac{m_\tau^3}{32\pi} \left(1 - \frac{m_\alpha^2}{m_\tau^2}\right)^2 \frac{1}{\Gamma(\tau \rightarrow l\nu\nu)}} \quad (7.10)$$

For an example ALP mass $m_\alpha = 200 \text{ keV}$ the limits are in table 7.1

| | $\tau \rightarrow e\alpha$ | $\tau \rightarrow \mu\alpha$ |
|-------------|------------------------------|------------------------------|
| UL (95% CL) | $5.34 \cdot 10^{-3}$ | $3.4 \cdot 10^{-3}$ |
| Λ | $0.3 \cdot 10^7 \text{ GeV}$ | $1.7 \cdot 10^7 \text{ GeV}$ |

Table 7.1: In the first row of the table, the upper limits UL at 95% on the branching fraction $Br(\tau \rightarrow l\alpha)/Br(\tau \rightarrow l\nu\nu)$ for $l = e, \mu$ given by the Belle II study. In the second row the recast on the coupling parameter $\Lambda/\cos(\varepsilon)$.

The study is conducted with a luminosity $L = 62.8 \text{ fb}^{-1}$. The goal on the Belle II luminosity is to reach $L = 50 \text{ ab}^{-1}$ which is a thousand times higher. It is possible to

make a naive recast of the UL in the case of $L = 50 \text{ ab}^{-1}$, knowing that the branching ratio scales as $\sim \sqrt{L}$. However the magnitude of Λ does not change and in the recast would not keep in account the different background in the machine at such luminosity.

Belle II detector can be useful to test high energy scales, yet it can't help in setting lower bounds on the Λ scale interesting for the model at least in the τ channel.

The model could be tested with other types of experiments, such as MEG II and MU3e, which are expected to reach lower limits on the Λ_a scale of order $\Lambda_a \sim 10^{10} \text{ GeV}$.

Conclusions

In this thesis, the theoretical and phenomenological implications of two classes of axion-like particle models have been considered: one is a “visible” QCD axion at the MeV/c^2 scale with flavor non-universal coupling to SM fermions such that the resulting axion is pion-phobic and able to evade a variety of very stringent phenomenological bounds (quarkonia decay, kaon decays, electron beam dump experiments); another is model describing an axion-like particle as DM candidate with tree-level flavor-violating couplings. It is exploited a new scenario where lepton flavor violation decays of SM leptons are directly responsible for the production of axion DM in the early Universe via the freeze-in mechanism.

Both models give rise to a very interesting phenomenology that can be tested at future lepton violating experiments such as Belle II, MEG2, Mu3e etc.

In particular, in this thesis, the sensitivities of some specific signatures of both models are investigated with the Belle II experiment.

To test the sensitivity of Belle II on the axion-electron coupling, a simulation of the channel ($e^+e^- \rightarrow \gamma a \rightarrow \gamma e^+e^-$) was made in the Belle II environment. The aim was to put an upper limit on the sensitivity.

The simulation was made through generation, simulation and reconstruction of signal events, for an axion with mass in the $15 - 30 \text{MeV}/c^2$ range. Monte Carlo simulations were also used to produce background events: the main SM background for the interesting process come from $e^+e^- \rightarrow e^+e^-(\gamma)$ and $e^+e^- \rightarrow \gamma\gamma \rightarrow \gamma \rightarrow e^+e^-$ with pair conversion from one of the two photons.

Preselections concerning energy of the final state photon, on the number of charged tracks in final state and total invariant mass were made in order to eliminate some background events.

The study conducted on the simulation focused on a variable capable of discriminating background from signal events. The variable is the radial coordinates of the reconstructed decay vertex into electron-positron pairs, indicated with the letter R. For the axion, the vertex should be near the IP, so a signal event should have a small R value; the photon background (the main one in this mass range) has instead a uniform distribution for the R values because of pair conversion happening in all the detector material. The strategy is to use a cut on the value of R as a selection criteria for the signal events, exploiting the difference between signal and background distributions.

In order to find the best value, the cut on R was optimized by the Punzi figure of merit, in a formulation used for only background experiments as the one considered. The resulting value for the cut on R makes the selection criteria for the signal events.

Once the events are selected, a coarse formula was used to calculate the sensitivity on the production cross section of the event $\sigma(e^+e^- \rightarrow a\gamma)$. The sensitivity is given for a cut and count experiment, without considering systematics. The sensitivity on the

cross section is then recast as sensitivity on the coupling parameter between electron and axion, entering the cross section formula.

The recast shows that the Belle II sensitivity for the parameter is of order (1 GeV) for the axion mass range considered. The values were then confronted with limits coming from the recast of dark photon search conducted by KLOE and BaBar experiments. The results obtained by Belle II lower the existing limits in the $25 \div 30 \text{ MeV}/c^2$ range.

The study is at a preliminary stage, and next steps can be made :

- implement other variables able to discriminate signal from the remaining background events (mainly given from $\gamma\gamma$) which are still considerable ($\sim 10^4$ events)
- implement a study for trigger efficiency
- insert also study of systematics
- explore different methods to set upper limits for the sensitivity on cross section

Belle II can be considered also as a τ factory, because of the high $\tau\bar{\tau}$ pair production rate. The heavy lepton can have decays included in beyond standard model theories, such as $\tau \rightarrow l\alpha$ where the final state lepton can be a muon or electron and α an invisible and long lived particle. To study lepton flavor violating process, as the one indicated, is overall important to search for new physics, this is why the Belle II collaboration conducted a study on the aforementioned simulation with a model independent approach.

The Belle II study gave an upper limit on the ratio between the branching ratio of the channel and the main background channel $\tau \rightarrow l\nu\nu$.

The results can be used to test the second model discussed in this thesis, which predict large LFV decays strictly related to the main channel responsible for the freeze-in DM production. The upper limits on the branching ratio were converted as lower limits on the coupling parameter between τ and the lepton, entering at first order thanks to the ALP. In the coupling parameter, the energy scale f_a enters. The study gives a resulting sensitivity of Belle II of order $f_a > 10^7 \text{ GeV}$. The freeze-in of LFV decays mechanism used to describe the dark matter abundance imply an energy scale of at least $f_a > 10^9 \text{ GeV}$. The conclusion is that the Belle II experiment, with the available study on the $\tau \rightarrow l\alpha$ channel, can not constraint the DM candidate model proposed. The model though can still be probed in different collider experiment, especially from the experiment Mu3e and MEG II which should be able to probe energy scales of order $f_a \sim 10^{10} \text{ GeV}$.

Bibliography

- [1] R. L. Workman *et al.*, “Review of Particle Physics,” *PTEP*, vol. 2022, p. 083C01, 2022. DOI: 10.1093/ptep/ptac097.
- [2] D. G. W.N. Cottingham, *An introduction to the Standard Model of Particle Physics*, 2nd ed. Cambridge university press, 2007.
- [3] L.-F. L. Ta-Pei Cheng, *Gauge theory of elementary particle physics*, 1st ed. Clarendon Press Oxford, 1988.
- [4] A. A. Belavin, A. M. Polyakov, A. S. Schwartz, and Y. S. Tyupkin, “Pseudoparticle Solutions of the Yang-Mills Equations,” *Phys. Lett. B*, vol. 59, J. C. Taylor, Ed., pp. 85–87, 1975. DOI: 10.1016/0370-2693(75)90163-X.
- [5] R. D. Peccei and H. R. Quinn, “CP Conservation in the presence of pseudoparticles,” *Phys. Rev. Lett.*, vol. 38, pp. 1440–1443, 25 Jun. 1977. DOI: 10.1103/PhysRevLett.38.1440. [Online]. Available: <https://link.aps.org/doi/10.1103/PhysRevLett.38.1440>.
- [6] M. Pospelov and A. Ritz, “Theta vacua, QCD sum rules, and the neutron electric dipole moment,” *Nucl. Phys. B*, vol. 573, pp. 177–200, 2000. DOI: 10.1016/S0550-3213(99)00817-2. arXiv: hep-ph/9908508.
- [7] R. D. Peccei and H. R. Quinn, “Constraints Imposed by CP Conservation in the Presence of Instantons,” *Phys. Rev. D*, vol. 16, pp. 1791–1797, 1977. DOI: 10.1103/PhysRevD.16.1791.
- [8] S. Weinberg, “A New Light Boson?” *Phys. Rev. Lett.*, vol. 40, pp. 223–226, 1978. DOI: 10.1103/PhysRevLett.40.223.
- [9] F. Wilczek, “Problem of Strong P and T Invariance in the Presence of Instantons,” *Phys. Rev. Lett.*, vol. 40, pp. 279–282, 1978. DOI: 10.1103/PhysRevLett.40.279.
- [10] L. Di Luzio, M. Giannotti, E. Nardi, and L. Visinelli, “The landscape of QCD axion models,” *Phys. Rept.*, vol. 870, pp. 1–117, 2020. DOI: 10.1016/j.physrep.2020.06.002. arXiv: 2003.01100 [hep-ph].
- [11] C. Vafa and E. Witten, “Parity Conservation in QCD,” *Phys. Rev. Lett.*, vol. 53, p. 535, 1984. DOI: 10.1103/PhysRevLett.53.535.
- [12] S. Scherer, “Introduction to chiral perturbation theory,” *Adv. Nucl. Phys.*, vol. 27, J. W. Negele and E. W. Vogt, Eds., p. 277, 2003. arXiv: hep-ph/0210398.
- [13] M. Bauer, M. Neubert, S. Renner, M. Schnubel, and A. Thamm, “The Low-Energy Effective Theory of Axions and ALPs,” *JHEP*, vol. 04, p. 063, 2021. DOI: 10.1007/JHEP04(2021)063. arXiv: 2012.12272 [hep-ph].

- [14] G. Bertone, D. Hooper, and J. Silk, “Particle dark matter: Evidence, candidates and constraints,” *Phys. Rept.*, vol. 405, pp. 279–390, 2005. DOI: 10.1016/j.physrep.2004.08.031. arXiv: hep-ph/0404175.
- [15] J. R. Primack, “Dark matter and structure formation,” in *Midrasha Mathematicae in Jerusalem: Winter School in Dynamical Systems*, Jul. 1997. arXiv: astro-ph/9707285.
- [16] S. Weinberg, *Cosmology*. 2008, ISBN: 978-0-19-852682-7.
- [17] T. Hambye, “On the stability of particle dark matter,” *PoS*, vol. IDM2010, p. 098, 2011. DOI: 10.22323/1.110.0098. arXiv: 1012.4587 [hep-ph].
- [18] T. R. Slatyer and C.-L. Wu, “General Constraints on Dark Matter Decay from the Cosmic Microwave Background,” *Phys. Rev. D*, vol. 95, no. 2, p. 023010, 2017. DOI: 10.1103/PhysRevD.95.023010. arXiv: 1610.06933 [astro-ph.CO].
- [19] P. A. R. Ade *et al.*, “Planck 2013 results. XVI. Cosmological parameters,” *Astron. Astrophys.*, vol. 571, A16, 2014. DOI: 10.1051/0004-6361/201321591. arXiv: 1303.5076 [astro-ph.CO].
- [20] L. J. Hall, K. Jedamzik, J. March-Russell, and S. M. West, “Freeze-In Production of FIMP Dark Matter,” *JHEP*, vol. 03, p. 080, 2010. DOI: 10.1007/JHEP03(2010)080. arXiv: 0911.1120 [hep-ph].
- [21] P. Arias, D. Cadamuro, M. Goodsell, J. Jaeckel, J. Redondo, and A. Ringwald, “WISPy Cold Dark Matter,” *JCAP*, vol. 06, p. 013, 2012. DOI: 10.1088/1475-7516/2012/06/013. arXiv: 1201.5902 [hep-ph].
- [22] G. Bertone and D. Hooper, “History of dark matter,” *Rev. Mod. Phys.*, vol. 90, no. 4, p. 045002, 2018. DOI: 10.1103/RevModPhys.90.045002. arXiv: 1605.04909 [astro-ph.CO].
- [23] J. Preskill, M. B. Wise, and F. Wilczek, “Cosmology of the Invisible Axion,” *Phys. Lett. B*, vol. 120, M. A. Srednicki, Ed., pp. 127–132, 1983. DOI: 10.1016/0370-2693(83)90637-8.
- [24] M. Trodden and S. M. Carroll, “TASI lectures: Introduction to cosmology,” in *Theoretical Advanced Study Institute in Elementary Particle Physics (TASI 2002): Particle Physics and Cosmology: The Quest for Physics Beyond the Standard Model(s)*, Jan. 2004, pp. 703–793. arXiv: astro-ph/0401547.
- [25] H. Georgi, D. B. Kaplan, and L. Randall, “Manifesting the Invisible Axion at Low-energies,” *Phys. Lett. B*, vol. 169, pp. 73–78, 1986. DOI: 10.1016/0370-2693(86)90688-X.
- [26] J. D. Bjorken, S. Ecklund, W. R. Nelson, *et al.*, “Search for Neutral Metastable Penetrating Particles Produced in the SLAC Beam Dump,” *Phys. Rev. D*, vol. 38, p. 3375, 1988. DOI: 10.1103/PhysRevD.38.3375.

- [27] E. M. Riordan *et al.*, “A Search for Short Lived Axions in an Electron Beam Dump Experiment,” *Phys. Rev. Lett.*, vol. 59, p. 755, 1987. DOI: 10.1103/PhysRevLett.59.755.
- [28] J. Redondo and A. Ringwald, “Light shining through walls,” *Contemp. Phys.*, vol. 52, pp. 211–236, 2011. DOI: 10.1080/00107514.2011.563516. arXiv: 1011.3741 [hep-ph].
- [29] K. Mimasu and V. Sanz, “ALPs at Colliders,” *JHEP*, vol. 06, p. 173, 2015. DOI: 10.1007/JHEP06(2015)173. arXiv: 1409.4792 [hep-ph].
- [30] A. Jodidio *et al.*, “Search for Right-Handed Currents in Muon Decay,” *Phys. Rev. D*, vol. 34, p. 1967, 1986, [Erratum: *Phys.Rev.D* 37, 237 (1988)]. DOI: 10.1103/PhysRevD.34.1967.
- [31] G. Hesketh, S. Hughes, A.-K. Perrevoort, and N. Rompotis, “The Mu3e Experiment,” in *2022 Snowmass Summer Study*, Apr. 2022. arXiv: 2204.00001 [hep-ex].
- [32] W. H. Bertl *et al.*, “Search for the Decay $\mu^+ \rightarrow e^+ e^+ e^-$,” *Nucl. Phys. B*, vol. 260, pp. 1–31, 1985. DOI: 10.1016/0550-3213(85)90308-6.
- [33] A. M. Baldini *et al.*, “The design of the MEG II experiment,” *Eur. Phys. J. C*, vol. 78, no. 5, p. 380, 2018. DOI: 10.1140/epjc/s10052-018-5845-6. arXiv: 1801.04688 [physics.ins-det].
- [34] A. Payez, C. Evoli, T. Fischer, M. Giannotti, A. Mirizzi, and A. Ringwald, “Revisiting the SN1987A gamma-ray limit on ultralight axion-like particles,” *JCAP*, vol. 02, p. 006, 2015. DOI: 10.1088/1475-7516/2015/02/006. arXiv: 1410.3747 [astro-ph.HE].
- [35] G. G. Raffelt, “Astrophysical axion bounds,” *Lect. Notes Phys.*, vol. 741, M. Kuster, G. Raffelt, and B. Beltran, Eds., pp. 51–71, 2008. DOI: 10.1007/978-3-540-73518-2_3. arXiv: hep-ph/0611350.
- [36] E. Armengaud *et al.*, “Axion searches with the EDELWEISS-II experiment,” *JCAP*, vol. 11, p. 067, 2013. DOI: 10.1088/1475-7516/2013/11/067. arXiv: 1307.1488 [astro-ph.CO].
- [37] R. Bernabei *et al.*, “Search for solar axions by Primakoff effect in NaI crystals,” *Phys. Lett. B*, vol. 515, pp. 6–12, 2001. DOI: 10.1016/S0370-2693(01)00840-1.
- [38] E. Arik *et al.*, “Probing eV-scale axions with CAST,” *JCAP*, vol. 02, p. 008, 2009. DOI: 10.1088/1475-7516/2009/02/008. arXiv: 0810.4482 [hep-ex].
- [39] M. A. Bershadsky, M. T. Ressell, and M. S. Turner, “Telescope search for multi-eV axions,” *Phys. Rev. Lett.*, vol. 66, pp. 1398–1401, 1991. DOI: 10.1103/PhysRevLett.66.1398.

- [40] M. Bauer, M. Neubert, and A. Thamm, “Collider Probes of Axion-Like Particles,” *JHEP*, vol. 12, p. 044, 2017. DOI: 10.1007/JHEP12(2017)044. arXiv: 1708.00443 [hep-ph].
- [41] D. Lombardi, “The DFSZ axion: analysis and generalization,” Laurea thesis, U. Bologna, DIFA, 2018.
- [42] D. S. M. Alves and N. Weiner, “A viable QCD axion in the MeV mass range,” *JHEP*, vol. 07, p. 092, 2018. DOI: 10.1007/JHEP07(2018)092. arXiv: 1710.03764 [hep-ph].
- [43] G. Mageras, P. Franzini, P. M. Tuts, *et al.*, “Search for Shortlived Axions in Radiative Υ Decays,” *Phys. Rev. Lett.*, vol. 56, S. C. Loken, Ed., pp. 2672–2675, 1986. DOI: 10.1103/PhysRevLett.56.2672.
- [44] R. Eichler *et al.*, “Limits for Shortlived Neutral Particles Emitted μ^+ or π^+ Decay,” *Phys. Lett. B*, vol. 175, p. 101, 1986. DOI: 10.1016/0370-2693(86)90339-4.
- [45] T. Aoyama, M. Hayakawa, T. Kinoshita, and M. Nio, “Tenth-Order Electron Anomalous Magnetic Moment — Contribution of Diagrams without Closed Lepton Loops,” *Phys. Rev. D*, vol. 91, no. 3, p. 033006, 2015, [Erratum: *Phys.Rev.D* 96, 019901 (2017)]. DOI: 10.1103/PhysRevD.91.033006. arXiv: 1412.8284 [hep-ph].
- [46] D. Hanneke, S. Fogwell, and G. Gabrielse, “New Measurement of the Electron Magnetic Moment and the Fine Structure Constant,” *Phys. Rev. Lett.*, vol. 100, p. 120801, 2008. DOI: 10.1103/PhysRevLett.100.120801. arXiv: 0801.1134 [physics.atom-ph].
- [47] D. Buttazzo, P. Panci, D. Teresi, and R. Ziegler, “Xenon1T excess from electron recoils of non-relativistic Dark Matter,” *Phys. Lett. B*, vol. 817, p. 136310, 2021. DOI: 10.1016/j.physletb.2021.136310. arXiv: 2011.08919 [hep-ph].
- [48] P. Panci, D. Redigolo, T. Schwetz, and R. Ziegler, “Axion Dark Matter from Lepton flavor-violating Decays,” Sep. 2022. arXiv: 2209.03371 [hep-ph].
- [49] F. D’Eramo and A. Lenoci, “Lower mass bounds on FIMP dark matter produced via freeze-in,” *JCAP*, vol. 10, p. 045, 2021. DOI: 10.1088/1475-7516/2021/10/045. arXiv: 2012.01446 [hep-ph].
- [50] D. Baumann, *Cosmology*. Cambridge University Press, Jul. 2022, ISBN: 978-1-108-93709-2, 978-1-108-83807-8. DOI: 10.1017/9781108937092.
- [51] E. Figueroa-Feliciano *et al.*, “Searching for keV Sterile Neutrino Dark Matter with X-ray Microcalorimeter Sounding Rockets,” *Astrophys. J.*, vol. 814, no. 1, p. 82, 2015. DOI: 10.1088/0004-637X/814/1/82. arXiv: 1506.05519 [astro-ph.CO].

- [52] F. D’Eramo and S. Yun, “Flavor violating axions in the early Universe,” *Phys. Rev. D*, vol. 105, no. 7, p. 075 002, 2022. DOI: 10 . 1103 / PhysRevD . 105 . 075002. arXiv: 2111.12108 [hep-ph].
- [53] A. Bettini, *Introduction to elementary particle physics*. 2008, ISBN: 978-0-521-88021-3.
- [54] W. Altmannshofer *et al.*, “The Belle II Physics Book,” *PTEP*, vol. 2019, no. 12, E. Kou and P. Urquijo, Eds., p. 123C01, 2019, [Erratum: PTEP 2020, 029201 (2020)]. DOI: 10.1093/ptep/ptz106. arXiv: 1808.10567 [hep-ex].
- [55] A. J. Bevan *et al.*, “The Physics of the B Factories,” *Eur. Phys. J. C*, vol. 74, p. 3026, 2014. DOI: 10.1140/epjc/s10052-014-3026-9. arXiv: 1406.6311 [hep-ex].
- [56] V. Bertacchi *et al.*, “Track finding at Belle II,” *Comput. Phys. Commun.*, vol. 259, p. 107 610, 2021. DOI: 10.1016/j.cpc.2020.107610. arXiv: 2003.12466 [physics.ins-det].
- [57] T. Abe *et al.*, “Belle II Technical Design Report,” Nov. 2010. arXiv: 1011.0352 [physics.ins-det].
- [58] I. Adachi, T. E. Browder, P. Križan, S. Tanaka, and Y. Ushiroda, “Detectors for extreme luminosity: Belle II,” *Nucl. Instrum. Meth. A*, vol. 907, pp. 46–59, 2018. DOI: 10.1016/j.nima.2018.03.068.
- [59] J. Alwall, M. Herquet, F. Maltoni, O. Mattelaer, and T. Stelzer, “MadGraph 5 : Going Beyond,” *JHEP*, vol. 06, p. 128, 2011. DOI: 10.1007/JHEP06(2011)128. arXiv: 1106.0522 [hep-ph].
- [60] A. J. Krasznahorkay, M. Csatlós, L. Csige, *et al.*, “On the X(17) Light-particle Candidate Observed in Nuclear Transitions,” *Acta Phys. Polon. B*, vol. 50, no. 3, p. 675, 2019. DOI: 10.5506/APhysPolB.50.675.
- [61] S. Agostinelli *et al.*, “GEANT4—a simulation toolkit,” *Nucl. Instrum. Meth. A*, vol. 506, pp. 250–303, 2003. DOI: 10.1016/S0168-9002(03)01368-8.
- [62] J. P. Lees *et al.*, “Search for a Dark Photon in e^+e^- Collisions at BaBar,” *Phys. Rev. Lett.*, vol. 113, no. 20, p. 201 801, 2014. DOI: 10.1103/PhysRevLett.113.201801. arXiv: 1406.2980 [hep-ex].
- [63] A. Savitzky and M. J. E. Golay, “Smoothing and differentiation of data by simplified least squares procedures.,” *Analytical Chemistry*, vol. 36, no. 8, pp. 1627–1639, 1964. DOI: 10.1021/ac60214a047. eprint: <https://doi.org/10.1021/ac60214a047>. [Online]. Available: <https://doi.org/10.1021/ac60214a047>.
- [64] G. Punzi, “Sensitivity of searches for new signals and its optimization,” *eConf*, vol. C030908, L. Lyons, R. P. Mount, and R. Reitmeyer, Eds., MODT002, 2003. arXiv: physics/0308063.

- [65] A. Anastasi *et al.*, “Limit on the production of a low-mass vector boson in $e^+e^- \rightarrow U\gamma$, $U \rightarrow e^+e^-$ with the KLOE experiment,” *Phys. Lett. B*, vol. 750, pp. 633–637, 2015. DOI: 10.1016/j.physletb.2015.10.003. arXiv: 1509.00740 [hep-ex].
- [66] X. Chen, Z. Hu, Y. Wu, and K. Yi, “Search for dark photon and dark matter signatures around electron-positron colliders,” *Phys. Lett. B*, vol. 814, p. 136076, 2021. DOI: 10.1016/j.physletb.2021.136076. arXiv: 2001.04382 [hep-ph].
- [67] H. Albrecht *et al.*, “A Search for lepton flavor violating decays $\tau \rightarrow e\alpha$, $\tau \rightarrow \mu\alpha$,” *Z. Phys. C*, vol. 68, pp. 25–28, 1995. DOI: 10.1007/BF01579801.